Escola de Camins
Escola Tècnica Superior d'Enginyeria de Camins, Canals i Ports
UPC BARCELONATECH

PROJECTE O TESINA D'ESPECIALITAT

Títol

Improving wave forecasting in the Catalan coast (WAM)

Autor/a

Adrià Moya Ortiz

Tutor/a

Agustín Sánchez-Arcilla Conejo
Jesús Gómez Aguar
Gerbrant Ph. van Vledder

Departament

Enginyeria Hidràulica, Marítima i Ambiental

Intensificació

Enginyeria Marítima

Data

Octubre 2014

Improving wave forecasting in the Catalan coast (WAM)

Adrià Moya

Department of Civil Engineering

Polytechnic University of Catalonia

This dissertation is submitted for the degree of

Civil Engineering

2014

I would like to dedicate this thesis to my loving parents.

Acknowledgements

I would like to heartily thank Prof. Agustín Sánchez-Arcilla, who offered assistance from the very first moment and encouraged me to take on this research. Because of him I could contact Jesús Gómez, who I would like to express my sincere gratitude for his role in conditioning the workspace, obtaining experimental data and proposing technical solutions.

I owe special gratitude to Dr. Gebrant Ph. van Vledder, who has provided me precious suggestions and advice. Without his guidance and encouragement through the past year at Delft University of Technology (the Netherlands), this study would not have been possible to accomplish.

My sincere thanks also go to Elena Pallarès, who has provided me with constructive suggestions and computing resources. Her work has brought much to this research.

Last but not least, sincere gratitude should be given to my dear friends and classmates in TU Delft, for their company during my study abroad experience. It was their hard work and perseverance that encouraged me to accomplish this research.

Abstract

The purpose of this study is to mainly investigate the effect of spectral energy dissipation on the temporal evolution of the wave spectrum, bring about more insight in this least understood part of the physics relevant to wave modeling and consequently propose a modification on the physics that rule such a dissipation model, supported on comprehensive spectral and integral analyses.

Such modifications attempt to correct, or at least improve, the frequent disagreement between predicted and observed wave data at the Catalan coast, especially during storm conditions. Particular attention is drawn to the Ebro delta area, not only because of the growing need to properly track its evolution but due to the common presence of characteristic bimodal spectra caused by the coexistence of wind-seas and swell trains.

The WAM Cycle 4.5.3 is implemented here in two nested grids covering all the Northwestern Mediterranean Sea with a grid resolution from 9 to 3 km, forced with corresponding low and high-resolution wind fields (WRF) for two typical storm events during January 2010.

The current dissipation model dependence on an overall wave steepness unavoidably yields systematic errors when more than one sea state are propagating. The results obtained, however, show a clear enhancement of the mean and peak wave periods for the study area, decreasing considerably the negative bias observed, whereas it is not possible to distinguish a representative improvement of wave heights by only tuning the whitecapping dissipation function.

Abstract

El propòsit principal d'aquesta recerca es basa en l'estudi de l'efecte de la dissipació d'energia espectral, en relació a l'evolució de l'espectre total d'energia, i assolir així, un major coneixement del comportament físic d'aquest terme. La dissipació d'energia és considerada, fins a l'actualitat i de forma generalitzada, un fenomen relativament desconegut. Adicionalment, es proposa una modificació adient a la física que regeix tal model, recolzant-se en l'anàlisis de paràmetres espectrals i integrats.

Les modificacions aplicades intenten corregir, o substancialment millorar, el freqüent desajustament entre prediccions i dades observades al litoral català, especialment durant condicions de tempesta. Especial atenció s'ha donat a la zona del Delta de l'Ebre, no només per la necessitat de dur a terme un correcte seguiment de l'evolució del mateix, sinó per la presència d'espectres bimodals característics, deguts a la coexistència de mar de vent i mar de fons.

El model oceànic WAM Cycle 4.5.3 s'ha implementat en aquest estudi, fent ús de dues malles niades cobrint així el Mediterrani Occidental, tot augmentant la seva resolució des de 9 fins a 3 km. Els camps de vent han estat simulats a partir del model atmosfèric WRF, per similars escales durant dues tempestes típiques del litoral.

El model de dissipació actual està governat pel peralt mig de l'espectre, fet del qual se'n deriven errors sistemàtics quan hi ha presència de més d'un estat de mar. No obstant, els resultats obtinguts mostren una encoratjadora millora dels períodes d'ona mitjana i pic a l'àrea d'estudi, on s'ha reduït considerablement el biaix negatiu observat. Tot i així, no ha estat possible distingir una millora clara de l'altura d'ona significant, basant-se només en l'ajustament de la funció de dissipació d'energia.

Contents

List of Figures

List of Tables

Symbols

Roman Symbols

A	normalization factor
a	wave amplitude
c	phase velocity
C_b	bottom friction coefficient
c_g	propagation speed of wave energy, group velocity
C_{ds}	dissipation coefficient (whitecapping tunable coefficient)
C'_{ds}	dissipation coefficient scaled with overall steepness for Pierson-Moskowitz spectrum
C_{nl4}	constant (DIA)
CDIS	dissipation coefficient scaled with overall steepness for Pierson-Moskowitz spectrum
d	water depth
$D(\theta)$	(one-dimensional) spreading function
$D(f,\theta)$	directional spreading function
D_{tot}	mean rate of energy dissipation per unit horizontal area due to wave breaking
$E(f)$	(one-dimensional) frequency energy spectrum
$E(f,\theta)$	(two-dimensional) directional energy spectrum

E_{tot}	total wave energy
$\mathscr{F}$	high-frequency dissipation in (one-dimensional) frequency spectrum
$\tilde{F}$	dimensionless fetch
F	fetch
f	frequency
f_0	starting frequency
$f_{\max}$	maximum frequency
$f_{\min}$	minimum frequency
f_{hf}	parametric tail cut-off frequency
f^*_{PM}	peak frequency of the fully developed sea state (Pierson-Moskowitz)
g	gravitational acceleration ($\approx$9.801 $\mathrm{m^2\,s^{-1}}$)
H	wave height, filter
h	wave height, mixing scale
H_s	significant wave height
H_w	height of the whitecap
$H_{1/3}$	significant wave height
h_{m0}	significant wave height
H_{max}	maximum wave height
H_{rms}	root-mean-square wave height
i	discrete dummy index
j	discrete dummy index
KL	number of directional bands
K	effective turbulent viscosity coefficient

k	wave number
k_p	peak wave number of the JONSWAP spectrum
L	wave length
L_w	length of the whitecap
ML	number of frequency bands
M_n	functional derivative matrix $\partial S_n/\partial E$
m_n	n-th order spectral moment
MAE	mean absolute error
N	number of data
n	discrete dummy index
N_n	nondiagonal residual matrix of M_n
$\bar{O}$	mean value of the observed data
O_i	observed value
p	exponential coefficient (whitecapping tunable coefficient)
R	correlation coefficient, radius of the Earth (6,378.1 km)
RMSE	root mean square error
$\bar{S}$	mean value of the simulated data
$\hat{s}$	overall wave steepness
$\hat{s}_{PM}$	overall wave steepness for the Pierson-Moskowitz spectrum
$S(f,\theta)$	(two-dimensional) directional source terms spectrum
S_i	simulated value
$S_{ds,br}$	depth-induced wave breaking dissipation
$S_{ds,b}$	bottom dissipation

$S_{ds,l}$	low-frequency dissipation term (Tolman and Chalikov, 1996)
$S_{ds,w}$	(whitecapping) wave breaking dissipation
S_{ds}	dissipation source term
S_{in}	wind input source term
S_{nl3}	triad wave-wave interactions
S_{nl4}	quadruplet wave-wave interactions
S_{nl}	nonlinear source term
SI	scatter index
$\bar{T}_0$	mean wave period or zero-crossing wave period
Δt	time step
t	time
$T_{1/3}$	significant wave period
T_{m02}	zero-crossing period
T_p	peak wave period
u_*	friction velocity in the atmospheric boundary layer
U_{10}	wind velocity at 10 m
z_0	roughness length
z_e	effective surface roughness

Greek Symbols

α	Phillips' coefficient, representative energy level
α_n	Phillips' dimensionless high-frequency energy level
α_{BJ}	fraction of breaking waves (Battjes and Janssen, 1978)
$\hat{\alpha}$	Charnock constant

β	dimensionless growth rate
δ	delta value (whitecapping tunable coefficient)
η	elevation of water surface
γ	breaker parameter
κ	Von Karman constant
λ	latitude, dimensionless critical height, constant (DIA)
Λ_n	diagonal matrix of M_n
ω	angular frequency (=$2\pi f$)
ϕ	empirical function accounting for development stage of waves
ρ	water density ($\approx 10^3$ kg m^{-3})
ρ_a	air density ($\approx$ 1.225 kg m^{-3})
σ	direction spreading
θ	wave direction
θ_m	mean wave direction
θ_w	wind direction
$\vec{\tau}$	total surface stress
$\vec{\tau}_w$	wave-induced stress
φ	latitude

Acronyms / Abbreviations

BS	Balearic Sea
CFSR	Climate Forecast System Reanalysis
DIA	Discrete Interaction Approximation
ECMWF	European Centre for Medium-Range Weather Forecasts

ERA-Interim	ECMWF meteorological re-analysis project (from 1979)
JONSWAP	Joint North Sea WAve Project
LIM-UPC	Laboratori d'Enginyeria Marítima
MM5	Mesoscale Meteorological model
NCAR	National Center for Atmospheric Research
NCEP	National Centers for Environmental Prediction
PdE	Puertos del Estado
SMC	Servei Meteorològic de Catalunya
SWAN	Simulating WAves Nearshore
WAM	WAve Model
WAMDIG	WAve Model Development and Implementation Group
WM	Western Mediterranean sea
WRF	Weather Research and Forecasting model
WWIII	WAVEWATCH III
XIOM	Xarxa d'Instruments Oceanogràfics i Meteorològics

Chapter 1

Introduction

1.1 Motivation

This thesis work was mainly originated with the goal of improving the current wave forecasting situation at the Catalan coast. It is known that the "Servei Meteorològic de Catalunya" (SMC), also known as "Meteocat", has driven its wave forecasts by using the wave model WAM over the Western Mediterranean Sea. Therefore, this study will be principally focused on getting deep insight into the wave model and, secondly, seeking the reasons by which non-negligible divergence exists between the outputs of such a model and the real measurements.

Many atmospheric, topographic and orographic features of the Catalan coast make it extremely difficult to develop accurate predictions, notably in situations where the coast is hit by exceptionally hazardous storms. The Spanish Mediterranean coast is subjected to a high usage and extremely variable climate (del Amo, 2000) influenced by the topography. Social and economical activities developed at the coastal area are significantly vulnerable to phenomena resulting from flooding and erosion, honoring the typical "torrential" Mediterranean climate. This has lately demanded a better understanding of the coastal climate and an enhanced toolset for quickly and efficiently reckon the possible hazards linked to the sea state that may threaten those coastal activities and, most importantly, the response of defense structures (see Day et al., 1997; Sánchez-Arcilla et al., 1998).

One of the difficulties experienced by the wave forecasting on the Mediterranean comes associated with the limited time and spatial scales, commonly attributed to storms generated by northwestern winds. In fact, scales of the order of 10 km and 12 hours (as the average duration of storms from directional wave records (Gómez et al., 2001) are the most common. Furthermore, high variability in both wind speed and direction is a key aspect to be

taken into account. This variability in the intensity comprises one of the hugest sources of errors and may thus entail a loss of information when it comes to solve the wave generation equations (Alomar, 2012). Just to give a mere example, wave models usually compute under the condition of the existence of a wind speed larger than the speed of the waves which results in an underestimation of wave conditions due to the fact of time- and space-averaged winds. This uncertainty is also found in the determination of an optimal wind which feeds a wave model, as much as the appropriate time step for integrating the system equations.

Nowadays, the wind field's quality over the oceans is generally good, but for enclosed basins, where the surface winds are affected by the presence of land, the accuracy of wind models diminishes substantially. In these areas the modeled surface wind speeds are almost always underestimated and the bias depends on the proximity of land. This negative effect appears in various locations of the Mediterranean Sea (Bertotti and Cavaleri, 2004).

This situation becomes particularly acute in the Northwestern Mediterranean due to the limited fetches (the longest fetch for the coast off Barcelona is of order of 600 km in the northeast direction) and the limited time of atmospheric storms. This situation brings a challenge for wind and consequently wave forecasting since conventional models are at the limit of their performance.

Other drawbacks concern the difficulty of characterizing the bathymetry of the Catalan coast. The irregularity of such geometric contours (submerged canyons, variable continental shelf width and presence of islands) has lead to a doubtful parameterization in not only wave but atmospheric prediction models which, naturally, influences the degree of applicability of such models.

It is therefore important to emphasize the need for better predictability at the Catalan coast, since wave integral parameters are used in many other fields' estimations (e.g., morphodynamics, port operation, civil work design criteria, navigation, etc.). For example, a quite common phenomenon is the beach erosion due to the predominant longshore current along the Catalan coast, which flows towards the southwest. The estimation of the mean transport of longshore drift, which is often less than the needed for the natural feeding of beaches, can be achieved through the CERC formula. This empirical relationship establishes that the longshore sediment transport is proportional the significant wave height to the power 2.5 ($S \propto H_s^{2.5}$). If the prediction of the wave height is underestimated by, for example, a 20%, it can be foreseen that the longitudinal transport will be even more, about a 43% underestimation. Therefore, it is evident that a mistaken computation of wave parameters may yield large errors in derived calculations that depend on such parameters.

Additionally, the incidence of high waves with elevated sea levels involve the over wash-

ing of the beach by the waves which, in low lying coasts, determines the presence of flooding of marine origin . The flood potential is characterized through the maximum elevation of water during, the storm surge, and wind forcing and wave currents are the main mechanisms in charge of piling up water at the coast and, hence, generate cross-shore sediment transport and shoreline migration. Therefore, a correct simulation of both the forcing at the surface and circulation underneath are demanded in order to quantitatively estimate the damage of a storm.

These, and many other applications, demonstrate the close bond between coastal engineering and modeling of the wave climate. Therefore, this study has added value in the sense that not only exposes the shortcomings of the wave predictability at the Catalan coast, but because of the many applications related to maritime and coastal engineering that rely on wave models. Overall, as stated above, this study aims to focus its research onto third-generation wave models (WAM model) and somehow contribute towards a more reliable description of the sea state at the Catalan coast.

1.2 Objectives

So far calibration of wave models has been performed by fine tuning the free parameters to fit the measurements at a location for a short time period. The "historical" way to actually calibrate a wave model was first to use a fetch-limited growth curve (e.g., WAMDIG, 1988) and then test it out on real cases, in particular at high winds.

The difficulty with this is to control the many degrees of freedom. The standard fetch-limited growth curves essentially control the difference between energy input and dissipation, but still exists the possibility of having both weaker input and weaker dissipation. As a result, Tolman and Chalikov (1996) parameterizations, with an input three times weaker than the Janssen (1991) input could yield reasonably good wave height estimates.

Things get more interesting when the wind is not perpendicular to the shore: in this case, the mean direction is a very good indicator of the strength of the source terms (Ardhuin et al., 2007). Several authors have based their parameterization's adjustments on that.

Then the problem is that the different wind fields (ECMWF operational analyses, ERA-Interim, NCEP operational analyses, CFSR, etc.) have different biases, and a model tuned with NCEP winds must be re-tuned with ECMWF winds. Also, looking back at times when little data were available, one cannot use data to assimilate in the model: this is true for global wave models before 1993. It is thus very important to be able to detect biases and find some corrections.

This brings up the following question: is it so insightful to perform a typical "tuning-calibration" based on a statistical validation of the results? In order to move forward, it seems more practical to understand where the source of a surplus or lack of energy in the wave spectrum is rooted in, which will have direct impact on integral parameters, and how, from a physical point of view, modifications should be implemented to overcome such shortcomings.

Therefore, the present study attempts to bring to the table the several features that lead to poor predictability in the Catalan coast, especially during storm conditions. Furthermore, the fact that limited data are available, suggests exploring the behavior of the wave model from a physical point of view to be the recommended option.

Along these lines, among others, the following objectives are expected to be achieved:

- Explore and analyze the typical storm events at the different buoy locations.
- Realize a validation of the model results with the buoys' data, from both integral and spectral points of view. To that end, reconstruction of wave spectra from pitch-and-roll buoy wave data shall be necessary. In addition, it is envisaged that partitioning of the wave spectrum should be carried out in order to get more insight during the process.
- Draw firm conclusions in accordance with similar investigations performed in the Catalan coast.
- Bring about recommendations and propose changes based on the results obtained.

1.3 Structure of the thesis

The document consists of six (6) chapters. First of all, in Chapter 2, an introduction of the study of ocean wave dynamics is given. This chapter provides a brief theoretical explanation of all parameters and methods used for the analysis of the wave records, from the basic statistics to the spectral analysis (mainly short-term analyses). Eventually, since the representation of the sea state is the main purpose of spectral wave models, the energy balance equation is presented, along with a comprehensive review of the main source terms that comprise such a balance. In order to introduce the present WAM Cycle 4.5, a comparison between the physics of each energy generation/dissipation mechanism and its numerical implementation into wave models is given.

Next, the Chapter 3 presents an update of the state of the art of wave modeling in relation with some practical aspects that shall be taken into account in this research. Firstly, a set of features that are relevant to the region of study are characterized. The quality of the wave predictions relies on how the physics capture those aspects, therefore it shall be further reviewed the up-to-date knowledge of the physics of characteristic key points, such as variable winds and directional response of waves to turning winds, and whether its numerical implementation has yield successful results. Special attention shall be drawn to spectral dissipation (in deep water) due to the fact that modifications in the physics of this mechanism shall be applied in the wave model. The idea that lies behind this strategy concerns the generalized lack of knowledge with reference to the energy dissipation, the possibility of gaining more insight from a physical point of view and understand how this mechanism behaves in a particular scenario such as the Catalan coast. Since the analysis both relates the spectral and physical properties of the source terms, handling and filtering wave data and reconstruction of 2D spectra from observational instrumentation shall be necessary to validate the model results. Therefore, for this purpose, main techniques are presented and discussed in this chapter as well. Ultimately, the partition of the wave spectrum (into different sea states) shall be also put into practice at later stages of this research. For this reason, the principal method implemented by the wave model is described.

In the Chapter 4, the region of study, wind estimates and wave instruments used to support this work are introduced. Data available are separated into two different sections: observed data and forecasted data.

Chapter 5, presents the basic set-up of the WAM wave model A review of the principal settings is therefore given, as well as brief introduction to the interval of study. This chapter therefore lays out of the modeling-pre-processing phase. On the other hand, Chapter 6 contains a presentation of the results and a summary of conclusions and recommendations. Similarly, this chapter describes the modeling-post-processing phase of validation of results.

Chapter 2

Physics approach and numerical implementation in wave models

2.1 Short-term statistics

Real ocean wind waves have an irregular character (not-periodic, not repeating itself in time and space) as opposed to the single sinusoidal signal. The waves are therefore called irregular or random waves. In spite of the seemingly unpredictable (random) way in which the signal fluctuates, if we describe the short-term variations in a statistical way by taking average parameters it appears that the statistics can be considered constant in time (stationary).

In order for the averages to be representative of the sea state, the record should be short enough to be statistically stationary (not changing in time). On the other hand the record should be long enough to get reliable averages. At sea 15-30 minutes is used, most commonly 20 min. Thus wind waves are a random stationary process for time scales up to half an hour. In practice one recording of for instance 20 min is done every three hours. This record is thought to be representative for the entire tune-period o f three hours. The duration of a storm is generally 6-8 h in which the conditions (mean wind speed) are more or less constant.

It appears that the short-term distribution of wave heights can be described by a Rayleigh distribution as long as we are dealing with not too steep waves at deep water. In those conditions the parameters as determined by the wave-by-wave analysis and by the spectral analysis can be related to each other by constant ratios. As a consequence, spectral wave models can estimate the spectrum and bring about the transformation of spectral parameters into statistical. Therefore, both descriptions are in biunivocal relation. Ultimately, the energy density spectrum can be obtained from the variance density spectrum by multiplying it

by the specific weight of the water (ρg).

Further insight into wave-by-wave analysis will not be provided since a statistical description will not be given in the present work. However, there is a roundabout way of arriving at a statistical representation of the sea state using the fact that the surface elevation at one location can be unraveled into various sine waves (harmonic wave components) with different frequencies of which the amplitudes and phases can be determined by so-called Fourier analysis (the random-phase/amplitude model).

Phases turn out to have any value without any preference, whereas only the amplitude spectrum remains to characterize the wave record. More commonly used is the variance spectrum due to the fact that it is a more relevant (statistical) quantity than the amplitude and because the energy of the waves is proportional to the variance.

$$E(f) = \rho g \lim_{\Delta f \to 0} \frac{1}{\Delta f} \left\langle \frac{1}{2} \underline{a}^2 \right\rangle \tag{2.1}$$

where E is the energy density spectrum, ρ is the water density, g is the gravitational acceleration, f is the frequency (with Δf a discrete frequency band) and $\langle \underline{a}^2/2 \rangle$ is the mean value of the amplitude variance (where the amplitude $\underline{a}$ is treated as a random variable). Since wave amplitudes are not available, the only amplitude in the absence of observations is to simulate the wave conditions.

Eq.(2.1) describes the energy distribution of waves (one-dimensional frequency spectrum). One can find in literature relationships that relate derived properties from this spectrum and integral parameters such as significant wave heights or mean and peak wave periods (Section 2.2). Although it is presented later, it can be assumed that spectral wave models are based on the resolution of the energy balance (where the energy at a particular location and time is represented by Eq.(2.1), or the two-dimensional, directional energy spectrum $E(f,\theta)$). This energy balance describes the evolution of wave energy and allows spectral wave models to compute the energy spectrum at each time step and consequently derive integral parameters from spectra.

This, however, shall be introduced later since a clear distinction can be made at this point: some integral parameters can be determined differently under certain conditions. It can be either assumed that sea is under idealized conditions (such that constant wind blows perpendicularly off a long and straight coastline over deep water; i.e., waves are unaffected by the seabed) or under more realistic, arbitrary conditions.

Wave modeling under idealized conditions Wave modeling for idealized cases (oceanic waters) can be achieved under the assumption that only parameters that are assumed to affect the waves, in addition to idealized wind (U_{10}), are the fetch (F), gravitational acceleration (g) and duration (t). These parameters are often reduced to three by expressing the duration in terms of an equivalent fetch. The remaining parameters can be combined into one dimensionless parameter, the dimensionless fetch $\tilde{F}$. Similarly, dimensionless significant wave height and dimensionless peak period can be obtained using the same parameters.

At short fetches, waves grow rapidly (young sea states), but gradually slow down until the growth eventually stops (fully developed sea). These three dimensionless parameters thus define the well-known growth curves, which can be used to determine the wave spectrum.

Various idealized spectra have been estimated over the years. Perhaps the simplest is that proposed by Pierson and Moskowitz (1964). They assumed that if the wind blew steadily for a long time over a large area, the waves would come into equilibrium with the wind and demonstrated that the spectrum maintains its shape along the fetch. This is in agreement with the concept of a fully developed sea (a sea produced by winds blowing steadily over hundreds of kilometers for several days).

After analyzing data collected during the Joint North Sea Wave Observation Project JONSWAP (under idealized deep-water conditions), the spectra observed appear to have a sharper peak tan the Pierson-Moskowitz spectrum. Scientists of JONSWAP decided to keep the shape of the Pierson-Moskowitz spectrum and to enhance its peak with a peak-enhancement function.

It has been considered important to determine its origin since the JONSWAP is commonly used as design spectrum in most of the wave models nowadays, even in highly variable wind fields. Furthermore, it has been proved that young sea state spectrum is almost always close to the JONSWAP spectrum since for sufficiently steep waves, the quadruplet wave-wave interactions tend to stabilize the shape of the spectrum. On the contrary, JONSWAP spectrum does not apply to swell because steepness is low and shape-stabilizing capacity of quadruplet interactions is weaker.

Therefore, under idealized conditions, the one-dimensional frequency spectrum has a universal shape: the JONSWAP spectrum for young sea states or the Pierson-Moskowitz spectrum for fully developed sea states. It must be noted, however, that JONSWAP spectrum agreed well in the North Sea and it has had successful implementation in open ocean conditions; nevertheless, spectra obtained in the Mediterranean Sea do not normally adjust to JONSWAP since most of the energy is not commonly restricted to a small frequency

range. Thereafter, due to its similarities with a semi-enclosed basin and complex orography, the different physical response of waves to variable winds calls for higher rates of wave growth in the Mediterranean Sea.

Wave modeling under more realistic, arbitrary conditions The idealized conditions above are generally inadequate since in the most energetic regions of the world, the wind varies rapidly both in time and space. To model waves under realistic oceanic water conditions, the concepts of fetch and duration cannot be used. Instead, the spectral energy balance of waves is computed. It represents the evolution of the wave spectrum, based on the propagation, generation, wave-wave interactions and dissipation of all individual wave components at the surface.

When waves propagate from deep into intermediate and shallow water depths, the waves transform; e.g., wave height, length and direction change until the waves finally break and lose their energy (waves are affected by processes such as refraction, shoaling, bottom friction and wave-breaking). When the water depth becomes less than about half the wavelength, the waves start to be affected by the bottom and slow down. A certain harmonic component retains its frequency but the propagation speed c decreases and the wave length L decreases correspondingly.

First third generation wave models, such as the present cycle of the WAM, incorporate the effects of shoaling, refraction, bottom friction and wind and are based on a spectrally integrated energy balance. (Numerically) solving the energy balance yields information on the wave transformation (i.e., the changes in H, L, c and wave direction θ) of a wave field while the waves approach the shore.

In the presence of a current, energy is not conserved anymore, since transfer of energy between waves and currents is possible. In that case another wave quantity, wave action E/ω, will be conserved and the wave action balance rather than the energy balance should be solve. In the absence of a current, the wave action balance reduces to the energy balance which is presented in Section 2.3.

Below the above mentioned relationships between integral and spectral parameters are described.

2.2 Relationship between integral and spectral parameters

There are basically two ways to characterize a wave record in terms of its short term statistics:

1. based on direct analysis of the time series and regarding it as a sequence of individual waves each with their one wave height and wave period (wave-by-wave analysis);

2. through a spectral analysis using the fact that the surface can be seen as a summation of an infinite number o f sine waves with different heights, periods and directions.

Various average parameters can now be derived of which the most obvious probably is the mean wave height. Nevertheless, the mean wave height is not used that often. Of more practical use is the significant wave height H_s or $H_{1/3}$. The significant wave height is defined as the average height of the highest one third of the waves:

$$H_{1/3} = \frac{1}{N/3} \sum_{j=1}^{N/3} H_j \tag{2.2}$$

where H_j is the j-th wave (with $j = 1$ the largest wave, $j = 2$ the second largest, etc.) and N is the total number of waves. It is called significant wave height because it approximately corresponds to visual estimates of experienced observers at sea of a representative wave height. Apparently observers tend to bias their estimates to the higher waves in the record.

The mean of all wave periods is called the mean wave period or zero-crossing wave period:

$$\bar{T}_0 = \frac{1}{N} \sum_{j=1}^{N} T_j \tag{2.3}$$

Similar to $H_{1/3}$, the significant wave period is defined as the average wave period of the highest one-third of the waves. The significant wave period is not correlated to visual estimates and therefore has less physical meaning:

$$T_{1/3} = \frac{1}{N/3} \sum_{j=1}^{N/3} T_j \tag{2.4}$$

The parameters (2.2), (2.3) and (2.4) are commonly used to characterize a wave record. Additionally, as previously introduced, parameters can be derived from the wave spectrum due to some well-known relationships. Therefore, after solving the energy balance equation by the WAM model (2.18), various important integral wave parameters can be derived from the calculated spectra.

First, the spectrum reveals the dominant frequencies in the wave record; most energy occurs at the spectral peak and the corresponding wave period is called the peak spectral period T_p. Therefore:

$$T_p = \frac{1}{f_p} \tag{2.5}$$

In addition, most of these derived parameters are expressed in terms of spectral moments:

$$m_n = \int_0^\infty f^n E(f)\,\mathrm{d}f \tag{2.6}$$

The significant wave height can be therefore defined as a function of the zero-order spectral moment as:

$$h_{m0} \approx 4\sqrt{m_0} \tag{2.7}$$

In a similar way, wave periods can be determined. For instance, the zero-crossing period:

$$T_{m02} = \sqrt{\frac{m_0}{m_2}} \tag{2.8}$$

Theoretically, (2.8) is equal to the zero-crossing period $\bar{T}_0$ as determined from the time series (2.3). For narrow spectra as for swell, T_{m02} and $T_{1/3}$ are approximately equal to the spectral peak period T_p. For a broader spectrum with a high frequency tail (a typical wind-sea spectrum) $T_{1/3}$ is approximately equal to 0.9 to 0.95 T_p and T_{m02} is roughly equal to 0.7 T_p. However, the value of T_{m02} should be considered with care; because of the sensitivity of the higher moments for higher frequencies, T_{m02} will be sensitive to details of the measurements and data-processing.

2.3 Energy balance equation

In this study we shall only consider the energy balance since it is solved by the present wave model, although it should be noted that more recent wave models are based on the

previously mentioned wave action balance (e.g., SWAN or WAVEWATCHIII).

The evolution of the energy density of each wave component (f,θ) can be obtained by integrating an energy evolution equation while propagating with the group velocity along a wave ray:

$$\frac{\mathrm{d}E(f,\theta;x,y,t)}{\mathrm{d}t} = S(f,\theta;x,y,t) \tag{2.9}$$

where the term on the left-hand side is the rate of change of the energy density, and $\mathrm{d}x/\mathrm{d}t = c_{g,x}$ and $\mathrm{d}y/\mathrm{d}t = c_{g,y}$ (where $c_{g,x}$ and $c_{g,y}$ are the x- and y-components of the group velocity of the wave component under consideration), and frequency and direction are constant (in deep water). The term on the right-hand side (called the source term) represents all effects of generation, wave–wave interactions and dissipation. Conceptually this (Lagrangian) approach is very straightforward because in deep water the wave rays are straight lines or great-circles and Eq.(2.9) needs only to be integrated along these lines.

The integration of the source term along each of these rays would not be difficult if that term were known along the rays. That, unfortunately, is not the case: at each point along the ray, the source term depends not only on the component that is being followed, but also on the entire, two-dimensional spectrum, at that point, i.e., on wave components that cross the wave ray (on their way across the ocean). The energy densities of these other components are not known (they travel along other wave rays), so the Lagrangian approach cannot be used for computations. It is conceptually attractive, but we need to use another approach for computations.

A workaround is available and it is provided by the Eulerian approach, in which the spectrum is computed not only at a single prediction point but rather at a large number of locations in the ocean simultaneously with a local energy balance at each of these locations. This approach is fundamentally correct and it is used in advanced wave modeling (second- and third-generation wave models).

The Eulerian formulation treats the energy balance of the waves on a regular geographic grid, either a Cartesian x, y-grid (for small areas) or a longitude-latitude λ, φ-grid (for larger areas). To derive the local energy balance for this approach, consider one cell of the geographic grid (size Δx in the x-direction and Δy in the y-direction); see Fig. 2.1. The energy balance for this cell (and all others in the grid) is essentially the bookkeeping of the energy of an arbitrary wave component (f,θ) traveling through this cell, i.e., balancing the change of energy in the cell over time interval Δt against the net import and the local generation of energy:

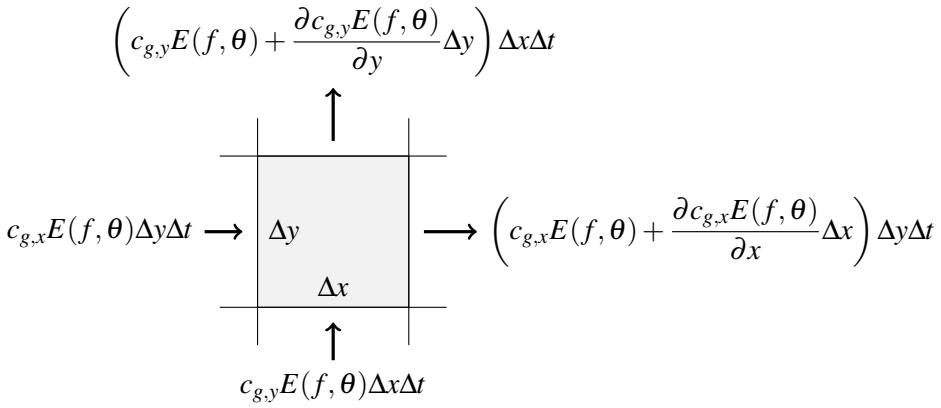

Fig. 2.1 The energy propagation through one cell of the regular grid projected onto the ocean in the Eulerian approach.

$$change\,of\,energy\,in\,cell = net\,import\,of\,energy + local\,generation\,of\,energy \tag{2.10}$$

The term on the left-hand side of this balance is equal to the energy in the cell at the end of the interval, minus the energy in the cell at the start of the interval. Ignoring the dependence on x, y and t in the notation, this can be written as:

$$\begin{aligned} change\,of\,energy\,in\,cell &= \left(E(f,\theta)\Delta x\Delta y+\frac{\partial E(f,\theta)}{\partial t}\Delta x\Delta y\Delta t\right)-E(f,\theta)\Delta x\Delta y \\ &= \frac{\partial E(f,\theta}{\partial t}\Delta x\Delta y\Delta t \end{aligned} \tag{2.11}$$

The first term on the right-hand side of the energy balance of Eq.(2.10) is the net import of energy into the cell during interval Δt. For the x-direction it is equal to the energy import through the left-hand side of the cell (with propagation speed $c_{g,x} = c_g \cos\theta$; the cell width is Δy) minus the energy export through the right-hand side of the cell (with an energy transport that has evolved over the distance Δx; see Fig. 2.1).

$$\begin{aligned} net\,import\,of\,energy\,in\,x\,direction &= c_{g,x}E(f,\theta)\Delta y\Delta t-\left(c_{g,x}E(f,\theta)+\frac{\partial c_{g,x}E(f,\theta)}{\partial x}\Delta x\right)\Delta y\Delta t \\ &= -\frac{\partial c_{g,x}E(f,\theta)}{\partial x}\Delta x\Delta y\Delta t \end{aligned} \tag{2.12}$$

Similarly, the net import of energy in the y-direction during the interval Δt is:

$$net\ import\ of\ energy\ in\ y\ direction = -\frac{\partial c_{g,y} E(f,\theta)}{\partial y}\Delta x \Delta y \Delta t \tag{2.13}$$

The second term on the right-hand side of the energy balance of Eq.(2.10) represents the locally generated energy in the cell, during the time interval Δt:

$$local\ generation\ of\ energy = S(f,\theta)\Delta x \Delta y \Delta t \tag{2.14}$$

where $S(f,\theta)$ is the source term, representing all effects of generation, wave–wave interactions and dissipation per unit time per unit surface area. So, in total, the energy balance for the cell $\Delta x \Delta y$ over the time interval Δt is (substituting Eqs.2.11–2.14 into Eq.2.10):

$$\begin{aligned}\frac{\partial}{\partial t}E(f,\theta)\Delta x \Delta y \Delta t = &-\frac{\partial c_{g,x} E(f,\theta)}{\partial x}\Delta x \Delta y \Delta t \\ &-\frac{\partial c_{g,y} E(f,\theta)}{\partial y}\Delta x \Delta y \Delta t + S(f,\theta)\Delta x \Delta y \Delta t\end{aligned} \tag{2.15}$$

where $c_{g,x} = c_g \cos\theta$ and $c_{g,y} = c_g \sin\theta$, and c_g is the propagation speed of wave energy. Dividing all terms by $\Delta x \Delta y \Delta t$ and moving the transport terms to the left-hand side gives the Eulerian spectral energy balance equation for each wave component, each cell, at each moment in time. Adding the dependence on time and horizontal space again in the notation gives:

$$\frac{\partial E(f,\theta;x,y,t)}{\partial t} + \frac{\partial c_{g,x} E(f,\theta;x,y,t)}{\partial x} + \frac{\partial c_{g,y} E(f,\theta;x,y,t)}{\partial y} = S(f,\theta;x,y,t) \tag{2.16}$$

The source term $S_{tot} = S(f,\theta;x,y,t)$ is often written as:

$$S_{tot} = S_{in} + S_{nl3} + S_{nl4} + S_{ds,w} + S_{ds,b} + S_{ds,br} \tag{2.17}$$

These terms denote, respectively, wave growth by the wind, nonlinear transfer of wave energy through three-wave and four-wave interactions and wave decay due to whitecapping,

bottom friction and depth-induced wave breaking. Only in deep water, S_{tot} can be reduced to S_{in}, S_{nl4} and $S_{ds,w}$.

These processes will be treated in the following but it must be noted that our understanding of these processes is far from complete. The quadruplet wave–wave interactions in deep water are well understood; the generation by wind is only reasonably well understood; and dissipation by white-capping is barely understood. The formulations that represent the last two processes in operational wave models are therefore to a large extent empirical (i.e., based on observations, intuition, speculation and calibrations).

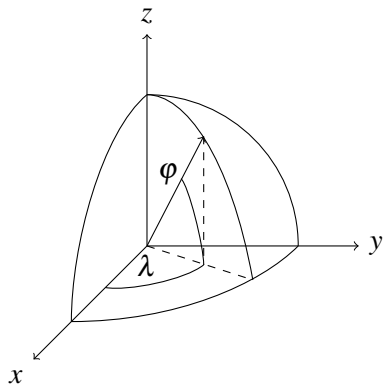

Fig. 2.2 Wave propagation on a globe.

For large areas and certainly for global scales, where longitude-latitude coordinates are required, the formulation of the energy balance of Eq.(2.16) needs to be modified to account for the effects of propagation on a sphere (i.e., a great-circle propagation). This approach is commonly implemented in wave models, since most of the time tend to first work at a large-scale level and then use these results as boundary conditions for a nested subdomain with higher grid resolution. The energy balance equation is then formulated, in spherical coordinates, as:

$$\frac{\partial E(f,\theta;\lambda,\varphi,t)}{\partial t}+\frac{\partial c_{g,\lambda}E(f,\theta;\lambda,\varphi,t)}{\partial \lambda}+(\cos\varphi)^{-1}\frac{\partial c_{g,\varphi}E(f,\theta;\lambda,\varphi,t)}{\partial \varphi} + \frac{\partial c_{g,\theta}E(f,\theta;\lambda,\varphi,t)}{\partial \theta}=S(f,\theta,;\lambda,\varphi,t) \quad (2.18)$$

where λ and φ are longitude and latitude, respectively, and $c_{g,\lambda}$ and $c_{g,\varphi}$ are the group velocity components in longitude and latitude directions respectively:

$$c_{g,\lambda} = \frac{c_g \sin\theta}{R\cos\varphi} \tag{2.19}$$

$$c_{g,\varphi} = \frac{c_g \cos\theta}{R} \tag{2.20}$$

and c_θ is the turning rate of the wave direction due to the change in (nautical) direction as the wave travels along a great circle:

$$c_\theta = \frac{c_g \sin\theta \tan\varphi}{R} \tag{2.21}$$

where R is the Earth's radius (the oblateness of the Earth is normally ignored in wave models).

The above Eulerian approach of modeling waves in the ocean is represented by only one equation: the energy balance equation Eq.(2.18), but the integration of this equation over space and time involves a very large number of points in geographic space and time and a large number of wave components. For each combination of these points and components this equation must be computed. This number of equations is very large: it is equal to the number of frequencies in the spectrum (≈30, say), times the number of directions in the spectrum (≈36, say), times the number of grid points in the geographic grid (≈10,000, say). The total is therefore easily 10,000,000 equations, which need to be computed at every time step of (typically) 15 min for the integration in time (i.e., about 500 times for a five-day forecast)! This illustrates the considerable computing power that is needed for an Eulerian oceanic wave model. The problem of the wave components being interdependent, which forced the move from a Lagrangian approach to this Eulerian approach, is now properly solved, but at a considerable price.

2.4 Source terms

2.4.1 Generation by wind

When the wind starts to blow over still water: the first waves to appear are small and very short, slowly getting longer and higher. Phillips' theory (1957) suggested that the wind, by its nature, induces a turbulent pressure on the water surface, propagating as a nearly frozen (random) field. This pressure field can be seen as a superposition of many harmonic

air-pressure waves, all oriented in many different direction but all propagating in the wind direction. For a constant wind, Phillips (1957) estimates this transfer (matching pressure waves transfer energy to their counterpart water waves by resonance) to be constant in time, resulting in a linear growth in time:

$$S_{in,1}(f,\theta) = \alpha \tag{2.22}$$

Miles' theory (1957) finds that air pressure at the water surface attains a maximum on the windward side of the wave crest and a minimum on the leeward side. This implies that the wind effectively pushes the water surface down where the wave surface is moving down (the windward side of the crest) and pulls the water surface up where it is actually moving up (the leeward side of the crest). This out-of-phase coupling between pressure and surface motion transfers energy to the waves. Therefore, the waves grow by this mechanism and the mechanism becomes more effective (positive feedback mechanism):

$$S_{in,2}(f,\theta) = \beta E(f,\theta) \tag{2.23}$$

where the coefficient β depends on the speed and direction of the wind and the waves. In summary, the source term for the generation of waves by wind can be written as a superposition between a linear growth (Phillips, 1957) and an exponential growth of $E(f,\theta)$ in time for a constant wind (Miles, 1957):

$$S_{in}(f,\theta) = \alpha + \beta E(f,\theta) \tag{2.24}$$

The shape of this source term (integrated over directions) for a JONSWAP spectrum is show in Fig. 2.3 Apparently, most of the energy transfer from wind to waves occurs at the spectral peak and on its high-frequency side.

WAM Cycle 4.5, and also previous versions, implements this model to estimate the source term contribution due to wind (S_{in}). Therefore, the transfer of wind energy to the waves is described with a resonance mechanism (Phillips, 1957) and a feed-back mechanism (Miles, 1957). The wave growth by wind is described by the same Eq.(2.25) (note the

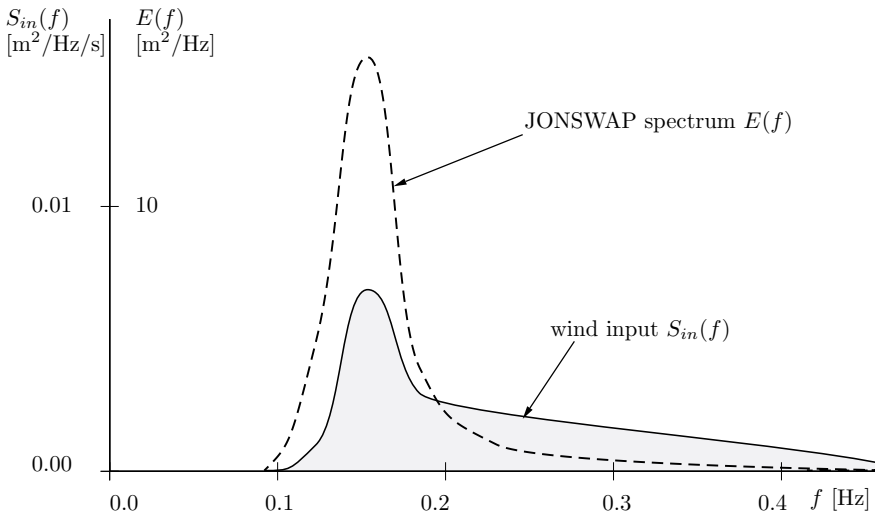

Fig. 2.3 The wind input source term, for a JONSWAP spectrum in deep water (for $h_{m0} = 3.5$ m, $T_{peak} = 7$ s and $U_{10} = 20\,\mathrm{m\,s^{-1}}$).

change of notation):

$$S_{in}(f,\theta) = A + BE(f,\theta) \tag{2.25}$$

in which A describes linear growth and $BE(f,\theta)$ exponential growth. For the WAM Cycle 4.5, the model is driven by the wind speed at 10 m elevation U_{10} whereas it uses the friction velocity u_*. The computation of u_* is an integral part of the source term and it represents an alternative measure for stress or momentum flux (more information in Komen et al., 1994).

Linear growth by wind

For the linear growth term α, the expression due to Cavaleri and Rizzoli (1981) is used with a filter to eliminate wave growth at frequencies lower than the Pierson-Moskowitz frequency (Tolman, 1992).

$$f_{PM}^{*} = \frac{0.13g}{28u_{*}} \tag{2.26}$$

$$H = \exp\left\{-\left(\frac{f}{f_{PM}^{*}}\right)^{-4}\right\} \tag{2.27}$$

$$A = \frac{1.5\times10^{-3}}{2\pi g^{2}}\left(u_{*}\max\left[0,\cos(\theta-\theta_{w})\right]\right)^{4}H \tag{2.28}$$

in which θ_w is the wind direction, H is the filter and f_{PM}^{*} is the peak frequency of the fully developed sea state according to Pierson and Moskowitz (1964) as reformulated in terms of friction velocity.

Exponential growth by wind

The expression for exponential growth by wind is due to Janssen (1991). It is based on a quasi-linear wind-wave-theory and is given by:

$$B = \beta\frac{\rho_{a}}{\rho_{w}}\left(\frac{u_{*}}{c}+\hat{\alpha}\right)^{2}\max\left[0,\cos(\theta-\theta_{w})\right]^{2}2\pi f \tag{2.29}$$

where β is the Miles constant. In the theory of Janssen (1991), this constant is estimated from the non-dimensional critical height λ:

$$\beta = \frac{\beta_{m}}{\kappa^{2}}\lambda\ln^{4}\lambda \tag{2.30}$$

$$\lambda = \frac{gz_{e}}{c^{2}}e^{r} \tag{2.31}$$

$$r = \kappa c/|u_{*}\cos(\theta-\theta_{w})| \tag{2.32}$$

where κ=0.40 is the Von Karman constant and z_e is the effective surface roughness. If the non-dimensional critical height λ>1, the Miles constant is set equal 0. Janssen (1991) assumes that the wind profile is given by:

$$U(z) = \frac{u_{*}}{\kappa}\ln\left[\frac{z+z_{e}-z_{0}}{z_{e}}\right] \tag{2.33}$$

in which $U(z)$ is the wind speed at height z (10 m) above the mean water level, z_0 is the roughness length. The effective roughness length z_e depends on the roughness length z_0 and the sea state through the wave-induced stress $\vec{\tau}_w$ and the total surface stress $\vec{\tau} = \rho_a |\vec{u}_*| \vec{u}_*$.

$$z_e = \frac{z_0}{\sqrt{1 - |\vec{\tau}_w|/\vec{\tau}}} \tag{2.34}$$

$$z_0 = \hat{\alpha} \frac{u_*^2}{g} \tag{2.35}$$

The second of these two equations is a Charnock-like relation in which $\hat{\alpha}$ is a constant equal to 0.011. The wave stress $\vec{\tau}_w$ is given by:

$$\vec{\tau}_w = \rho_w \int_0^{2\pi} \int_0^{\infty} \omega B E(\omega, \theta) \cos(\theta - \theta_w) \frac{\vec{k}}{k} \mathrm{d}\omega \mathrm{d}\theta \tag{2.36}$$

The value of u_* can be determined for a given wind speed U_{10} and a given wave spectrum $E(\omega, \theta)$ from the above set of equations. Note that the directional spectrum in (2.36) is expressed in terms of the angular frequency ω. A simple change of variable may be applied to use frequencies. In the following, wave spectrum and source term functions are arbitrarily described by either f or ω.

2.4.2 Nonlinear wave-wave interactions

The second mechanism that affects wave growth in deep water is the transfer of energy among the waves, i.e., from one wave component to another, by resonance. To visualize this mechanism consider two wave trains (with different frequencies and directions) approaching each other obliquely. The resulting waves create a diamond pattern of crests and troughs, which has its own wave length, speed and direction.

Such a diamond pattern would interact with a third, freely propagating wave component (i.e., one obeying the dispersion relationship of the linear wave theory if this third wave had the same wave length, speed and direction as the diamond pattern. The original pair of wave components would thus interact with this third wave component if the proper conditions were met (triad wave–wave interaction). Each of the components would thus have lost or gained energy, but the total energy (the sum of the energy of the three components at each

point in the ocean) would remain constant. Such interaction between freely propagating waves is called resonance.

Triad wave–wave interactions therefore do not occur in deep water. However, it is possible in deep water to have one pair of wave components interacting with another pair, if the wave numbers (and frequencies) of the two corresponding diamond patterns match. The reason is that, in deep water, two such pairs, i.e., four wave components, can fulfill the resonance conditions and can thus resonate. This matching of frequencies and wave numbers is expressed with the resonance conditions:

$$f_1 + f_2 = f_3 + f_4 \tag{2.37}$$

$$\vec{k}_1 + \vec{k}_2 = \vec{k}_3 + \vec{k}_4 \tag{2.38}$$

These resonance conditions state that, if the frequency, wave number and direction of one diamond pattern coincide with those of another diamond pattern, then energy is transferred among the four free components involved. Such a set of four wave components is called a quadruplet and the interactions are called quadruplet wave–wave interactions. The full expressions for these interactions have been given by Hasselmann (1962).

$$\begin{aligned} S_{nl4}(\vec{k}_4) = \iiint T_1(\vec{k}_1,\vec{k}_2,\vec{k}_1+\vec{k}_2-\vec{k}_4)E(\vec{k}_1)E(\vec{k}_2)E(\vec{k}_1+\vec{k}_2-\vec{k}_4)\mathrm{d}\vec{k}_1\mathrm{d}\vec{k}_2 \\ - E(\vec{k}_4)\iiint T_2(\vec{k}_1,\vec{k}_2,\vec{k}_4)E(\vec{k}_1)E(\vec{k}_2)\mathrm{d}\vec{k}_1\mathrm{d}\vec{k}_2 \end{aligned} \tag{2.39}$$

The exact computation of the nonlinear interactions S_{nl} involves the evaluation of a six dimensional Botzmann integral, which includes an interaction function with strong moving singularities. The dimension of the integral is effectively reduced due to the fact that contributions exist only for so-called quadruplets of four spectral components. As previously mentioned, it reduces the integral to a three-dimensional integral. However, even with present day computer technology, and with various improvements in the efficiency of the computation of these integrals the exact integral is prohibitively expensive for use in practical models.

The numerical implementation of the quadruplet wave-wave interactions is achieved with the development of the Discrete Interaction Approximation (DIA) as proposed by Hasselmann et al. (1985), which proved sufficiently economical for application in operational wave models. In the DIA, two quadruplets of wave numbers are considered, both with

(angular) frequencies:

$$\omega_1 = \omega_2 = \omega\,,\ \omega_3 = \omega(1+\lambda) = \omega^+\,,\ \omega_4 = \omega(1-\lambda) = \omega^- \tag{2.40}$$

where λ is a constant coefficient set equal to 0.25. To satisfy the resonance conditions for the first quadruplet, the wave number vectors with frequency ω_3 and ω_4 lie at an angle of $\theta_1 = -11.5°$ and $\theta_2 = 33.6°$ to the two identical wave number vectors with frequencies ω_1 andω_2. The second quadruplet is the mirror of this first quadruplet (the wave number vectors with frequency ω_3 and ω_4 lie at mirror angles of $\theta_3 = 11.5°$ and $\theta_4 = -33.6°$.

Within this discrete interaction approximation, the source term $S_{nl4}(\omega,\theta)$ is given by:

$$S_{nl4}(\omega,\theta) = S^*_{nl4}(\omega,\theta) + S^{**}_{nl4}(\omega,\theta) \tag{2.41}$$

where S^*_{nl4} refers to the first quadruplet and S^{**}_{nl4} to the second quadruplet (the expressions for S^{**}_{nl4} are identical to those for S^*_{nl4} for the mirror directions) and:

$$S^*_{nl4}(\omega,\theta) = 2\delta S_{nl4}(\alpha_1\omega,\theta) - \delta S_{nl4}(\alpha_2\omega,\theta) - \delta S_{nl4}(\alpha_3\omega,\theta) \tag{2.42}$$

in which α_1=1, α_2=$(1+\lambda)$and α_3=$(1-\lambda)$. Each of the contributions (i=1,2,3) is:

$$\delta S_{nl4}(\alpha_i\omega,\theta) = C_{nl4}(2\pi)^2 g^{-4}\left(\frac{\omega}{2\pi}\right)^{11}\left[E^2(\alpha_i\omega,\theta)\left\{\frac{E(\alpha_i\omega^+,\theta)}{(1+\lambda)^4} + \frac{E(\alpha_i\omega^-,\theta)}{(1-\lambda)^4}\right\} - 2\frac{E(\alpha_i\omega,\theta)E(\alpha_i\omega^+,\theta)E(\alpha_i\omega^-,\theta)}{(1-\lambda^2)^4}\right] \tag{2.43}$$

with constant $C_{nl4} = 3\times10^7$. Following Hasselmann and Hasselmann (1981), the quadruplet interaction in finite water depth is taken identical to the quadruplet transfer in deep water multiplied with a scaling factor:

$$S^{finite\,depth}_{nl4} = R(k_p d)S^{deep\,water}_{nl4} \tag{2.44}$$

where R is given by:

$$R(k_p d) = 1 + \frac{C_{sh1}}{k_p d}(1 - C_{sh2} k_p d)\exp(C_{sh3} k_p d) \tag{2.45}$$

in which k_p is the peak wave number of the JONSWAP spectrum for which the original computations were carried out. The values of the coefficients are: $C_{sh1} = 5.5$, $C_{sh2} = 6/7$ and $C_{sh3} = -1.25$. In the shallow water limit, i.e., $k_p \to 0$ the nonlinear transfer tends to infinity. Therefore, a lower limit of $k_p = 0.5$ is applied (cf. Komen et al., 1994), resulting in a maximum value of $R(k_p d) = 4.43$. To increase the model robustness in case of arbitrarily shaped spectra, the peak wave number k_p is replaced by $k_p = 0.75\,\langle k \rangle$ (cf. Komen et al., 1994).

The quadruplet wave–wave interactions only redistribute energy over the spectrum. No energy is added or withdrawn from the spectrum as a whole. The + / – / + character of this source term, at least for a JONSWAP-type spectrum (with zero at the peak frequency; see Fig. 2.4), implies that the quadruplet interactions transfer a significant fraction of the wind input from the mid-range frequencies to lower frequencies and a small fraction to higher frequencies. At the high frequencies, white-capping dissipates this energy. At the low frequencies, the energy is absorbed without appreciable dissipation. The energy at the low frequencies therefore grows, shifting the peak of the spectrum to lower frequencies, and thus dominating the evolution of the spectrum.

A remarkable property of the quadruplet interactions is their capacity to stabilize the shape of the spectrum of steep waves, i.e., waves that are being generated by wind. If, for instance, the tail of the spectrum deviates locally from a smooth shape (e.g., there is a small hump in the tail), the quadruplet interaction will smooth the tail back to approximately the universal f^{-4}-shape (for instance). Alternatively, if the shape deviates considerably from the JONSWAP shape, the quadruplet interactions will force it (back) into a JONSWAP shape (e.g., with a f^{-4}-tail). This is the main reason why the JONSWAP spectrum is often observed in storms, which do not even approximate the idealized situation in which the JONSWAP spectrum was first observed. Of course, it is the balance among the wind input, the quadruplet wave–wave interactions and the white-capping that determines the actual shape of the spectrum. If the wind is strong and highly variable (in speed or direction), the wind input may have a stronger effect on the shape of the spectrum than the quadruplet wave–wave interactions and a non-JONSWAP spectrum may evolve. However, if the wind varies sufficiently slowly, the quadruplet wave–wave interactions will dominate and a

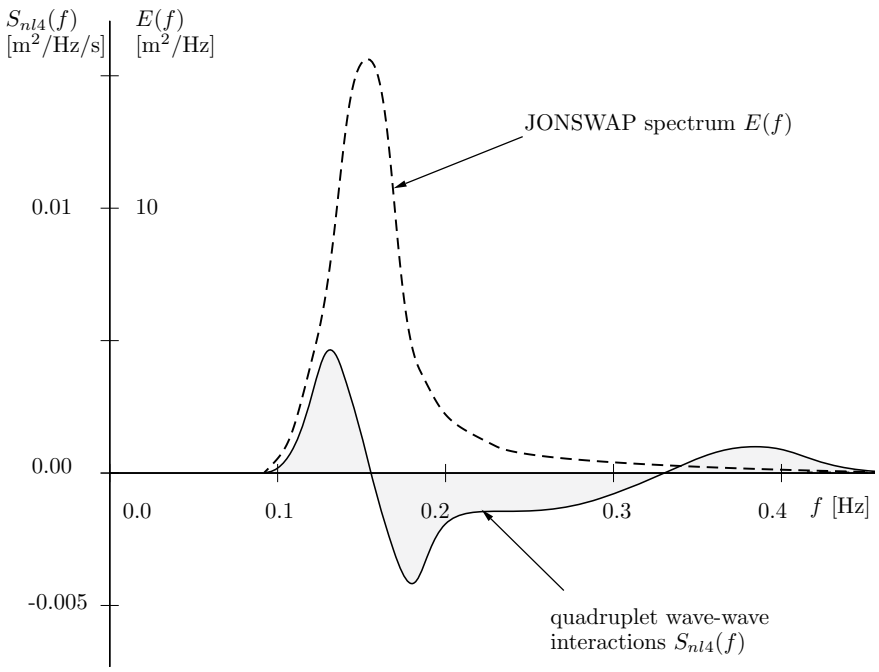

Fig. 2.4 The source term for quadruplet wave-wave interactions, for a JONSWAP spectrum in deep water (for $h_{m0} = 3.5$ m, $T_{peak} = 7$ s and $U_{10} = 20\,\mathrm{m\,s^{-1}}$).

JONSWAP spectrum evolve. This is usually the case in a storm and even in large parts of a hurricane.

This shape-stabilizing effect of the quadruplet wave–wave interactions is the reason why the JONSWAP spectrum is widely accepted as the design spectrum for engineering purposes. However, if the wind drops, or the waves leave their generation area, the steepness of the waves reduces sharply (due to frequency-dispersion and direction-dispersion) and the quadruplet wave–wave interactions decrease accordingly. Under swell conditions, therefore, a JONSWAP spectrum is not be expected. In fact, the spectral shape then depends entirely on the history of the individual wave components, which may be very different for different portions of the spectrum. At wind-sea, this usually results in a spectrum with multiple swell peaks and a locally generated JONSWAP spectrum at higher frequencies.

2.4.3 Dissipation of wave energy

The mechanism of wave energy dissipation largely depends on the water depth or, more precisely, whether the water column is located at deep water or shallow water. In deep water ($h > L/2$), waves do not feel the bottom and the only mechanism that dissipates energy is the wave breaking (whitecapping). On the other hand, at shallow water ($h < L/2$),

waves are significantly influenced by the presence of the sea bottom and the dissipation term is represented by the summation of three different contributions: whitecapping, bottom friction and depth-induced breaking. Even though a quick overview of the bottom friction and depth-induced breaking is given (mainly its implementation in the WAM model), due to the fact that most of the time we will be dealing with deep water conditions, all the attention shall be directed to the whitecapping mechanism.

Wave breaking in deep water (whitecapping)

Wave breaking in deep water (whitecapping) is a very complicated phenomenon, which so far has defied theoretical understanding. It involves highly nonlinear hydrodynamics on a wide range of scales, from gravity surface waves to capillary waves, down to turbulence. A complicating factor is that there is no generally accepted precise definition of breaking and quantitative observations are very difficult to carry out. Not surprisingly, therefore, breaking is the least understood of all processes affecting waves. Due to this reason, it is common practice to calibrate numerical wave models by tuning the parameters included in the corresponding formulation (at a preliminary stage). Such is the importance and large lack of knowledge about this mechanism that a more detailed overview of the spectral dissipation will be presented in the Section 3.2.

Some speculations as to what controls wave breaking have been made and it seems reasonable to assume that it is the wave steepness. However, observations at sea (deep water) have shown that whether an individual wave is breaking or not is almost independent of the steepness of that wave (but the maximum steepness $H_{max}/L = 0.14$, deduced from the maximum wave height H_{max} presented by Miche (1944), seems to be an upper limit).

The breakers in the open ocean are called whitecaps. and its occurrence is essentially a characteristic of the sea state itself, but whitecapping is obviously closely related to the wind.

The (dissipative) effect of whitecapping on the evolution of the waves is locally highly nonlinear, but on average, i.e., averaged over a large number of waves, it is rather weak. In wave models it is therefore represented as a source term in the energy balance of the waves. In spite of the uncertainty about the relevance of wave steepness, several approaches to deriving such a source term are based on this assumption.

The best-known is the theory of Hasselmann (1974) in which each whitecap acts as a pressure pulse on the sea surface, just downwind of the crest. At that location in the wave, the weight of the whitecap acts against the rising sea surface, thus draining energy from the wave. This is almost the mirror-image of the feedback mechanism for wind-induced

growth proposed by Miles (1957) the whitecap drains energy from the wave (transporting it to surface currents and turbulence) at roughly the same location as where the wind transfers energy to the wave. In other words, the weight of the whitecap counteracts, to some extent, the pulling effect of the deficit in air pressure on the lee side of the wave crest.

The corresponding shape of the source term is shown in Fig. 2.5 for JONSWAP spectrum.

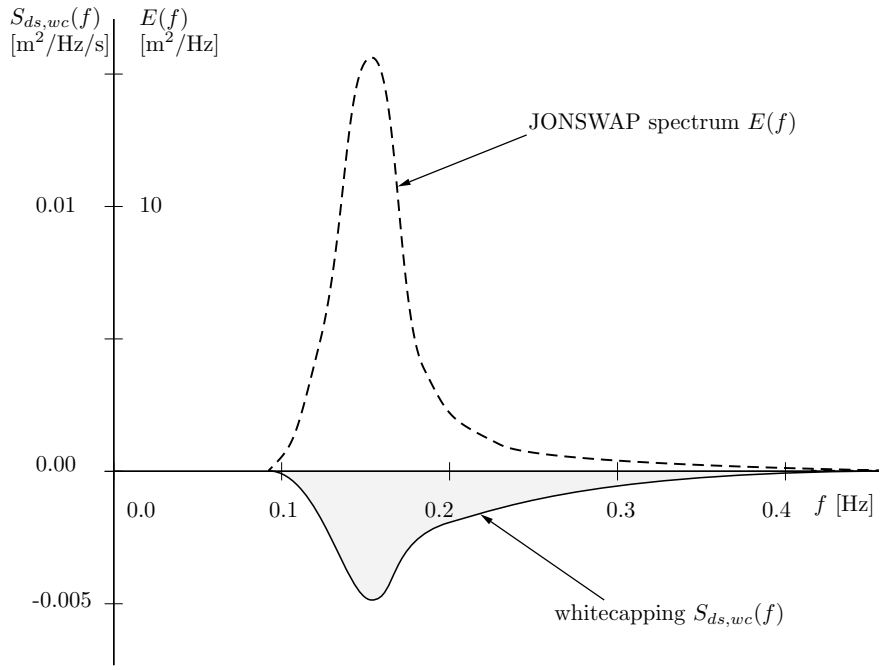

Fig. 2.5 The whitecapping source term, for a JONSWAP spectrum in deep water (for $h_{m0} = 3.5$ m, $T_{peak} = 7$ s and $U_{10} = 20\,\mathrm{m\,s^{-1}}$).

In the present cycle of the WAM model, the process of whitecapping is represented by the latter model of Hasselmann (1974). Reformulated in terms of wave number (rather than frequency) so as to be applicable in finite water depth (cf. WAMDIG, 1988), this expression is:

$$S_{ds,w}(\omega,\theta) = -\Gamma \langle \omega \rangle \frac{k}{\langle k \rangle} E(\omega,\theta) \tag{2.46}$$

where $\langle \omega \rangle$ and $\langle k \rangle$ are the mean (angular) frequency and the mean wave number. The coefficient Γ depends on the overall wave steepness. This steepness dependent coefficient has been adapted by Günther et al. (1992).

$$\Gamma = C_{ds}\left[(1-\delta)+\delta\frac{k}{\langle k\rangle}\right]\left(\frac{\hat{s}}{\hat{s}_{PM}}\right)^{p} \tag{2.47}$$

For $\delta = 0$ the expression of Γ reduces to the expression as used by WAMDIG (1988).The coefficients C_{ds}, δ and p are tunable coefficients, $\hat{s}$ is the overall wave steepness, $\hat{s}_{PM}$ is the value of $\hat{s}$ for the Pierson-Moskowitz spectrum (Pierson and Moskowitz, 1964): $\hat{s}_{PM} = \sqrt{3.02\times10^{-3}}$. The overall wave steepness $\hat{s}$ is defined as:

$$\hat{s} = \langle k\rangle\sqrt{E_{tot}} \tag{2.48}$$

The mean frequency $\langle\omega\rangle$, the mean wave number $\langle k\rangle$ and the total wave energy E_{tot} are defined as (cf. WAMDIG, 1988):

$$E_{tot} = \int_0^{2\pi}\int_0^{\infty} E(\omega,\theta)\,\mathrm{d}\omega\mathrm{d}\theta \tag{2.49}$$

$$\langle\omega\rangle = \left[E_{tot}^{-1}\int_0^{2\pi}\int_0^{\infty}\frac{1}{\omega}E(\omega,\theta)\,\mathrm{d}\omega\mathrm{d}\theta\right]^{-1} \tag{2.50}$$

$$\langle k\rangle = \left[E_{tot}^{-1}\int_0^{2\pi}\int_0^{\infty}\frac{1}{\sqrt{k}}E(\omega,\theta)\,\mathrm{d}\omega\mathrm{d}\theta\right]^{-2} \tag{2.51}$$

The values of the tunable coefficients C_{ds} and δ and exponent p in this model were obtained by Komen et al. (1984) by closing the energy balance of the waves in idealized wave growth conditions (both for growing and fully developed wind seas) for deep water. This implies that coefficients in the steepness dependent coefficient Γ depend on the wind input formulation that is used. For the wind input of Janssen (1991) and Günther et al. (1992) it was obtained (assuming $p = 4$) $C_{ds} = 4.10\times10^{-5}$ and $\delta = 0.5$ (as used in the WAM Cycle 4; Günther et al., 1992).

Replacing these values into the Eq.(2.46) one can find the shallow water version of the whitecapping formulation proposed.

$$S_{ds,w}(\omega,\theta) = -\frac{C_{ds}}{\hat{s}_{PM}^4}\langle\omega\rangle E_{tot}^2\langle k\rangle^4\left[(1-\delta)\frac{k}{\langle k\rangle}+\delta\left(\frac{k}{\langle k\rangle}\right)^2\right]E(\omega,\theta) \tag{2.52}$$

Similarly, whitecapping source term, expressed in terms of frequency (deep water case), can be obtained by using the dispersion relationship (2.53):

$$\omega^2 = gk \tanh kd \tag{2.53}$$

It is known that at deep water the (angular) frequency is independent of the depth, $\tanh kd \to 1$ and, therefore Eq.(2.53) can be reduced to:

$$\omega^2 = gk \tag{2.54}$$

Hence, replacing the wave number in equation Eq.(2.52) will lead to the whitecapping formula applied in deep water:

$$\begin{aligned} S_{ds,w}(\omega,\theta) &= -\frac{C_{ds}}{\hat{s}_{PM}^4} \langle\omega\rangle E_{tot}^2 \langle k\rangle^4 \left[(1-\delta)\frac{k}{\langle k\rangle} + \delta\left(\frac{k}{\langle k\rangle}\right)^2\right] E(\omega,\theta) \\ &= -\frac{C_{ds}}{\hat{s}_{PM}^4} \langle\omega\rangle \left(\frac{\langle\omega\rangle^2}{g}\sqrt{E_{tot}}\right)^4 \left[(1-\delta)\frac{\omega^2}{\langle\omega\rangle^2} + \delta\frac{\omega^4}{\langle\omega\rangle^4}\right] E(\omega,\theta) \\ &= -\frac{C_{ds}}{\hat{s}_{PM}^4} \langle\omega\rangle \frac{\langle\omega\rangle^8}{g^4} E_{tot}^2 \left[(1-\delta)\frac{\omega^2}{\langle\omega\rangle^2} + \delta\frac{\omega^4}{\langle\omega\rangle^4}\right] E(\omega,\theta) \\ &= -\frac{C_{ds}}{\hat{s}_{PM}^4} \frac{\langle\omega\rangle^9}{g^4} E_{tot}^2 \left[(1-\delta)\frac{\omega^2}{\langle\omega\rangle^2} + \delta\frac{\omega^4}{\langle\omega\rangle^4}\right] E(\omega,\theta) \end{aligned} \tag{2.55}$$

or in terms of the frequency:

$$S_{ds,w}(f,\theta) = -\frac{C_{ds}}{\hat{s}_{PM}^4} \frac{(2\pi\langle f\rangle)^9}{g^4} E_{tot}^2 \left[(1-\delta)\frac{f^2}{\langle f\rangle^2} + \delta\frac{f^4}{\langle f\rangle^4}\right] E(f,\theta) \tag{2.56}$$

The present WAM Cycle 4.5, similarly to previous version, implements Hasselmann (1974) dissipation model. In shallow water, the dissipation function is expressed in terms of wave number and in deep water in terms of frequency, by using the dispersion relationship (2.53). Besides, the C_{ds} dissipation coefficient does not appear explicitly in the model's subroutine, but scaled with the overall steepness for the Pierson-Moskowitz spectrum. Therefore, such a parameter, which shall be serve as tuning parameter for the whitecapping dis-

sipation at later stages of this research, is represented by C'_{ds} (hereinafter, in WAM model outputs, called CDIS). Hence:

$$C'_{ds} = \frac{C_{ds}}{\hat{s}^4_{PM}} \tag{2.57}$$

Janssen (1991) and Günther et al. (1992) obtained $C_{ds} = 4.10 \times 10^{-5}$ and $\delta = 0.5$. Using these values, the scaled dissipation coefficient (2.57) is equal to $\approx$ 4.5. In Chapter 6 it is addressed the influence of C'_{ds} over the overall spectral energy. It can be advanced that 4.5 yields too much energy dissipation during storm conditions at the Catalan coast.

Bottom friction

The empirical model of JONSWAP (Hasselmann et al., 1973) is the bottom friction formulation implemented, which can be expressed in the following form:

$$S_{ds,b}(f,\theta) = -C_b \frac{\omega^2}{g^2 \sinh^2 kd} E(f,\theta) \tag{2.58}$$

in which C_b is the bottom friction coefficient and, in agreement with the JONSWAP result for swell dissipation, Hasselmann et al. (1973) found $C_b = 0.038\ \mathrm{m\,s^{-3}}$. Bouws and Komen (1983) selected a bottom friction coefficient of $C_b = 0.067\ \mathrm{m\,s^{-3}}$ for fully developed wave conditions in shallow waters. In principle, the former value is employed by default in the present model.

Depth-induced wave breaking

To model the energy dissipation in random waves due to depth-induced breaking, the bore-based model of Battjes and Janssen (1978b) is used. The mean rate of energy dissipation per unit horizontal area due to wave breaking D_{tot} is expressed as:

$$D_{tot} = -\alpha_{BJ} Q_b \langle \omega \rangle \frac{H^2_{max}}{8\pi} \tag{2.59}$$

in which $\alpha_{BJ} = 1$ in WAM Cycle 4.5, Q_b is the fraction of breaking waves determined by (solved by using Newton-Raphson method):

$$\frac{1 - Q_b}{\ln Q_b} = -\left(\frac{H_{rms}}{H_{max}}\right)^2 \tag{2.60}$$

with:

$$H_{max} = \gamma d \tag{2.61}$$

$$H_{rms} = 2\sqrt{2}\sqrt{m_0} = 2\sqrt{2}\sqrt{E_t ot} \tag{2.62}$$

where $\gamma = 0.8$. Extending the expression of Eldeberky and Battjes (1996) to include the spectral directions, the dissipation for a spectral component per unit time is calculated as:

$$S_{ds,br}(f,\theta) = \frac{D_{tot}}{E_{tot}} E(f,\theta) = -\frac{\alpha_{BJ} Q_b \langle \omega \rangle H_{max}^2}{8\pi E_{tot}} E(f,\theta) \tag{2.63}$$

Chapter 3

Innovation for the Catalan coast

Since this research attempts to bring to light and address the main weak points that lead to a poor representation of the spectral dissipation, an extensive explanation of the findings found so far in literature is presented. Furthermore, there are additional aspects that directly influence the predictability in this particular region and, likewise, affect the dissipation (Section 3.2). Therefore, in this chapter an overview of the up-to-date knowledge of these fields is given. Last but not least, some techniques involved in developing an insightful validation of wave estimates are provided (Section 3.3).

3.1 Wave modeling in the Catalan coast

3.1.1 The Northwestern Mediterranean Sea

First, particular focus is placed upon the several aspects that compromise the quality of predictions at the Catalan coast. The source of such factors is not only related to modeling but the physical characteristics of the Mediterranean Sea and evolution of storms, for instance.

The Mediterranean Sea is a semi-enclosed sea for it has limited exchange of water with the outer ocean. For practical reasons, it can be considered as a big lake in the sense that it is highly influenced by the coastline and the surrounding orography. Wave forecasting in this region is subject of extensive research and important progress has been achieved so far.

The reasons for the limited predictability in the study region are determined by a wave climate controlled by (1) short fetches, (2) shadow effect of waves from the south and east due to the Balearic islands, (3) complex bathymetry with deep canyons close to the coast, (4) high wind field variability in the time and space, (5) wave calms during the summer and energetic storms from October to May (marked seasonality), (6) presence of wind jets

canalized by river valleys, (7) sea and swell waves combination that generate bi-modal spectra and (8) relatively short periods associated with swell waves, which compromise the proper distinction between wind-sea and swell.

The abovementioned factors yield a characteristic behavior of integral parameters during storm conditions. More specifically, underestimation of wave height maximum values and overestimation of wave heights during calm periods (Bolaños, 2004) is often observed. Additionally, wave periods still suffer a notable underprediction. Pallares et al. (2014), however, obtained a clear improvement of the mean wave period and the peak period at the Catalan coast, decreasing considerably the negative bias observed. Nevertheless, almost no change was observed in wave height due to the proposed modification.

Several authors have reported similar conclusions in areas with characteristic features in accordance with the Western Mediterranean Sea. Akpınar et al. (2012) found an underprediction of the significant wave height and period for the Black Sea. Similar results were obtained also in semi-enclosed basins and bays, as Lin et al. (2002) who conducted a study in Chesapeak Bay (USA) where waves were dominated by locally generated and fetch-limited young seas. Although wave heights displayed slight overprediction, peak wave periods showed low correlation and negative bias.

Rogers et al. (2003) observed a similar undeprediction pattern and concluded that the cause lied in an underprediction of low- and medium-frequency energy in the modeled spectrum, together with an overly strong dissipation of the swell. Their solution is further detailed in the Section 3.2.

3.1.2 Effects on wave growth

However, inconsistent dissipation cannot be blamed for the present poor predictability since other factors have also large influence on the distribution of wave energy. Before introducing the concept of short fetch and its shortcomings in wave modeling, it is convenient to introduce the wind wave growth and the development of different sea states.

The process of generation of waves can be seen as a rather linear wave growth achieved through energy transfer from the wind to those waves traveling at slower velocities. Wave speed is directionally proportional to wave period and, thus, waves speed up as they grow (young sea states). Eventually, waves slow down as they approach fully-developed conditions, when it is assumed that wind has blown long enough (in time) and over a long enough distance (fetch) so waves run as fast as the wind and they do not grow anymore (Holthuijsen, 2007). Within the wave growing phase, two different conditions may happen and detour sea states from their full development: fetch-limited and duration-limited condi-

tions. Fetch-limited waves are not fully developed because the fetch (distance) is not long enough. Instead, duration-limited waves are not fully developed due to the fact that wind has not blown long enough (time).

With reference to the sea states: wind-sea refers to wind waves being actively generated by in-situ winds. Swell, on the other hand, refers to wind waves that were generated by remote wind conditions but which are no longer growing. Therefore, wind-sea is still highly influenced by wind, whereas swell is only more residually influenced by wind.

In relation to the above explanation of wave growth, both sea states can be related to the different stages: wind-sea can be associated to young sea states (although as they run over the fetch they become older wind-seas), whereas swell wave trains are fully-developed due to the processes of frequency- and direction-dispersion.

Offshore-blowing winds (with very small fetches along the land to sea direction) are frequent, particularly prevailing between October and May, when regional northwestern winds (Mistral) become more intense and persistent (Fig. 4.3). Wind-sea grows and propagates southwards along a rather short fetch due to the presence of the Balearic Islands (more precisely the island of Ibiza) leading to a fetch-limited wave growth (Fig. 4.4).

Additionally, one needs to be aware that the wind variability, commonly blamed for the inaccurate wave predictions in the NW Mediterranean Sea, is mainly due to the complex orography of the coastal areas. During storm conditions this variability has been reported to increase.

With particular reference to the Ebro delta, due to the concurrence of several factors, it has been reported that: (1) the air-flow channeling along the river valley provides high-intensity, offshore-blowing winds that generate wind-seas in fetch-limited conditions, (2) due to the short duration of the storms in the NW Mediterranean Sea, fully-developed waves cannot be attained not only because of fetch-limited but duration-limited conditions,(3) variable wind conditions, during which wind may not blow uniformly from the coast towards offshore, lead to a deviation from the more homogeneous conditions of wave growth and (4) lead to more than one dominant direction during a storm event. It should be pointed out that the third effect is slightly reduced at the Ebro delta due to the previously mentioned canalization of wind, which results in a fairly steady air-flow with a marked direction during storm driven by northwestern winds.

However, due to the complexity of the pre-coastal Catalan Mountain Range, wind commonly displays rapid variations not only in speed but also in direction across the Catalan coast. Therefore, the accuracy of wave forecasting in fetch-limited conditions and variable wind conditions such as the region of interest is known to be limited (Bolaños, 2004).

Alomar (2012) researched in depth this topic and suggested two different approaches to tackle these shortcomings: (1) increase the spatial and temporal resolution of both the forcing wind and the wave model and (2) adjust the non-dimensional wave growth curves, i.e., using observed data to derive empirical relationships between wind and waves.

So far, most of the work carried on towards including the effect of wind variability in wave predictions is focused on the smaller temporal scales and gustiness. Abdalla et al. (2002) provides a new growth rate, which accounts for gustiness and is higher than the traditional one, whose impact on the model performance was, although positive, rather limited. Alternatively, Babanin and Makin (2008) pointed to an increased drag coefficient in gusty wind conditions, which enhances the transfer of energy from wind to waves. Ultimately, Komen et al. (1994) stated that wave growth is indeed affected significantly by both the temporal and spatial variability of the wind fields (not necessary gustiness), thus justifying the interest to focus on wind and wave gradients.

3.1.3 Implications for wave modeling

Spatial and temporal resolution of wind and wave fields The above mentioned limitations have direct implications on regional wave modeling. Spatial gradients in the wind fields are generated by the irregular orography that results in jet-like patterns over the sea. Although the effect on waves is expected to be less sharp, because of the slower response of waves to winds, significant differences in wave heights have been found between available buoys. However, due to the excessive spacing between buoy stations, the spatial scale of coastal wind jets cannot be estimated. Nevertheless, authors such as Alomar (2012) have reported wave height differences between points separated by 30 km, both along the coast and in the offshore direction, off the Ebro delta. A minimum spatial resolution of the regional model should be below half the coastal wind jet's spatial scale. On reflection, due to the width of the various river valleys influencing the work of Alomar (2012), it was eventually concluded that in order to resolve wind jets due to local orography of roughly 10 km wide, grid resolution should be between 3.3 and 5 km.

On the other hand, characteristic wind speed of such coastal jets may dramatically increase and decrease within 6 h, thus resulting in temporal scales shorter than 6 h. It is common use to implement input wind fields with a frequency of 6 h in regional wave modeling, as it is actually practiced in this research. However, if aiming to capture temporal scales of coastal wind jets, it shall be necessary to enlarge the frequency of input wind fields up to at least 3 h, as suggested by Alomar (2012).

Interference from land presence As a final note, in reference with wind, it has been reported the wind blowing from land to sea may lead to significant errors when it comes to modeling. This is due to the fact that wind speed at land grid points is assumed to be zero, thus causing sharp gradients in wind speed in grid cells that contain land grid points. Therefore, an assessment of the impact of the non-negligible interference from land presence shall be performed in applications where winds blow from land.

Numerical schemes Additional effects may have significant implications in regional wave modeling such as the proper estimation of propagation mechanisms (swell attenuation and slanting fetch; Alomar, 2012). Ardhuin et al. (2007) reported that a moderate swell opposing the wind does not significantly impact wind wave growth. Moreover, these authors concluded that models reproduced fairly well the directional change due to slanting fetch effects and suggested that an increase of the model's directional resolution would not bring about a major improvement of the directional energy spread.

The response of waves to varying wind speed in terms of wave energy and frequency is fairly well understood. To achieve a similar degree of understanding for the directional response, a corresponding parameterization is often used of the mean wave direction relaxing towards the local wind direction. This was done, for example, by SWAMP Group (1985). The response of waves in turning-wind situations has mostly been studied with heave, pitch and roll buoys. These can be used to estimate integral directional parameters (Kuik et al., 1988) or the buoy data can be used to reconstruct a low-resolution image of the directional energy distribution (see Section 3.3.1).

For moderate angles (20°-30°) between the wind and shore-normal direction, observed wind-sea evolution agreed well with height and period growth curves (Ardhuin et al., 2007). This situation is commonly reproduced at the buoy of Tortosa, where northwestern off-shore blowing wind tends to be directed approximately perpendicular to the coast. In addition, they concluded that results that included both swell and wind waves clearly showed that the parameterizations proposed by the WAMDIG (1988) were not very well adapted to this very common type of sea state. This is addressed in Section 3.2.

Large- and small-scale domains There are further aspects related to wave modeling that should be reviewed. The use of a small- or large-scale domain can be crucial. In this research, a coarse domain is used to cover the whole Western Mediterranean, while a small-scale, nested grid is implemented, placing the focus on the Catalan coast. Bertotti and Cavaleri (2009) concluded that, although the quality of the performance drops substantially in enclosed seas, the quality of results improves with increasing resolution, and indeed the

performance of small-scale models (higher resolution) considered outperformed the large-scale models (lower resolution). Note that it is necessary to start the simulation for the large-scale model in order to capture the effect of storms generated away from the study region, and thus transfer such information to the corresponding boundaries of the small-scale model. If only small-scale simulations were considered, a crucial loss of information would likely produce large errors in the study area. Therefore, it is unavoidably necessary to be aware of the dimensions of the scale required to cover all those phenomena that may impact the location of interest. Bear in mind that a nested model behaves according to the information it starts from (large-scale domain) and the subsequent boundary conditions along the forecast range. If time or space errors are present in the large-scale domain, they will unavoidable be reflected, possibly amplified, in the small-scale domain (Bertotti and Cavaleri, 2009).

High-frequency tail The application of a high-frequency tail is introduced into the numerical model to reduce computation time. The high-frequency part of the wave spectrum is important for calculating the momentum flux between the wind and the sea. It can be shown that the air-sea momentum exchange for developing wind waves takes place primarily at the high-frequency part of the spectrum, which therefore has to be modeled accurately (e.g., Makin and Kudryavtsev, 1999).

The WAM Cy 4.5, similarly to the previous cycle, solves the energy balance equation (2.18) up to a certain dynamically cut-off frequency f_{hf}, which is dependent on place, time, u_*, mean frequency of the spectrum, and largest frequency in the discrete frequency grid. The low frequency part of the calculated wave spectrum E, i.e. for $f \leqslant f_{hf}$, is called the prognostic part of the wave spectrum. Cut-off frequency f_{hf} corresponds to a wave length $\lambda \approx 10\,\mathrm{m}$.

For frequencies larger than f_{hf} (i.e., for waves shorter than 10 m), the spectrum is assumed to behave according to a diagnostic tail, which is proportional to f^{-5} as described by Phillips (1958). In other words, the high-frequency part of the spectrum is assumed to be

$$E \propto f^{-5}, \quad f \geqslant f_{hf} \tag{3.1}$$

where the proportionally constant equals $E(f_{hf})f_{hf}^5$ patching the prognostic part of the diagnostic tail of the spectrum. Therefore, the complete high-frequency tail is merely determined by cut-off frequency f_{hf}, the pre-assumed f^{-5}-profile of the diagnostic tail and spectral level $E(f_{hf})$.

The prognostic part of the wave spectrum is dependent on the so-called inverse wave age, defined as the ratio U_{10}/c, describing the stage of wave development for wind sea. This relation lifts the prognostic part of the spectrum upward for young sea, whereas it is pushed downward for old sea. However, the high-frequency part of the spectrum is also shifted up- and downwards according to patching spectral level $E(f_{hf})$ of the highest prognostic frequency bin by Eq.(3.1). This numerical feature implies a direct relation between the wave age and the high-frequency part of the wave spectrum, which does not correspond to the behavior of the diagnostic tail observed in nature, which is a drawback of the application of the pre-described high-frequency tail.

Further information with relation to the diagnostic tail is provided in Appendix **??**.

3.2 Spectral dissipation in deep water

As it was introduced in Chapter 2, spectral wave energy dissipation represents the least understood part of the physics relevant to wave modeling. There is hardly any agreement neither on the basic physics of the process nor on the best way, although empirical, to model it. The physical knowledge of the process and its implementation on wave modeling differ completely and evolve along separate tracks. Although many efforts are being focused on developing wave models towards a best and most physical solution, since whitecapping is a rather unknown process, it is often used as a tuning knob to best-fit the results and measurements. In this study, analyses of the physics of the dissipation and the numerical simulations of the spectral dissipation are separated into different subsections.

3.2.1 Theoretical research of physics of the spectral dissipation

Theoretical and even experimental results in this area are few and often contradictory. So far, several energy sink mechanisms have been recognized as possible candidates for energy dissipation, although three dissipation sources are considered the most important ones: those due to wave breaking, wave-turbulence and wave-wave modulation. Here, however, only spectral dissipation due to wave breaking is reviewed since it is the only mechanism implemented in wave models so far.

It is generally assumed that S_{ds} is a function of the wave spectrum E but there is no agreement on whether the spectral dissipation S_{ds} is linear in terms of E. Donelan and Yuan (1994) classified theoretical models of the spectral dissipation into three types:

1. probability models,

2. quasi-saturated models and

3. whitecap models.

None of these models, however, deals with the physics of wave breaking which governs the energy loss. Present analytic models try to employ either a wave state immediately prior to the breaking or the residual wave and turbulence features after the breaking to derive conclusions on the dissipation due to breaking.

Probability models The first analytic model is based on considering wave prior to breaking is called the probability model (Longuet-Higgins, 1969; Yuan et al., 1986). This approach is founded on the Stokes' limiting criterion that waves will break when the downward acceleration at the crest exceeds $g/2$. Such waves were assumed to break until the wave height is reduced back to a limiting value, and the difference was attributed to the dissipation. More recently, however, it has been shown that waves do not necessarily have to reach the $g/2$ acceleration limit to break (Holthuijsen and Herbers, 1986). Additionally, once they are breaking they do not stop at the Stokes limiting steepness but may keep losing energy until their steepness is well below the Stokes limit.

Quasi-saturated models The second type of prior-to-breaking class of models is the quasi-saturated model (Phillips, 1985; Donelan and Pierson, 1987). These models rely on the equilibrium range of the wave spectrum, where some sort of saturation exists for the wave spectral density. In this region, the wind input, the wave-wave interactions and the dissipation are assumed to be in balance. They suggested that whitecapping is essentially local in wave number space, i.e., at each wave scale (wave number); any excessive energy contributed by combined wind input and nonlinear interaction fluxes do not bring about spectral growth but wave breaking and can be interpreted as the spectral dissipation. They picture the wave breaking process as highly nonlinear in the wave steepness, having no effect until some limiting steepness is achieved when the wave form becomes unstable and spills plunges forward, producing a whitecap at large and intermediate scales or a micro-breaker at very small scales. This model type has a main shortcoming: none of the source terms which shape the spectral balance are known explicitly and accurately enough to provide a reliable determination of the dissipation as a residual sink term. Finally, there is growing evidence that dominant waves and the breaking of dominant waves affect dissipation at smaller scales (Banner et al., 2000;Young and Babanin, 2006). If that is true, dissipation in the saturation interval will not be a function in wave number scale.

Whitecap models The most mathematically well-advanced and most frequently utilized dissipation model is that due to Hasselmann (1974) and it shall be therefore comprehensively explained here. The assumptions are that the whitecaps can be treated as a random distribution of perturbation forces, which are formally equivalent to pressure pulses, and that the scales of the whitecaps in space and time are small compared to the wavelength and period of the associated wave (see Fig. 3.1).

First, it is shown generally that all processes which are weak-in-the-mean, even if they are strongly nonlinear locally, yield source functions which are quasi-linear to lowest interaction order: the source function consists of the spectrum at the wave number considered multiplied by a factor which is a functional of the entire wave spectrum (and which depends also on additional external factors, such as the wind speed). Secondly, an attempt is made to determine that factor for the special case of whitecapping. This involves a number of rather complex approximations based on the assumed space- and time-scale inequalities of the whitecaps and the energy containing waves of the spectrum.

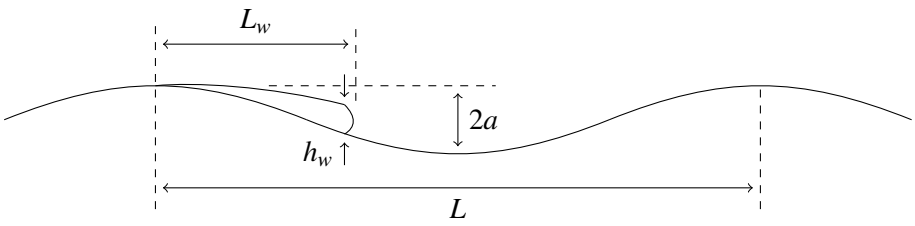

Fig. 3.1 Geometric similarity of whitecap and wave.

The existence of an attenuation factors in this model implies that the whitecaps are preferably situated on the forward faces of the waves, thereby exerting a downward pressure on the upward moving water and hence doing negative work on the wave. Furthermore, the extent of the whitecap, along the direction of travel of the wave, varies in proportion to the length of the wave.

Duncan (1981) performed various experiments in a laboratory and concluded that these steady whitecaps and the underlying waves were in geometric similarity:

$$L_w/L = const, \tag{3.2}$$

$$H_w/a = const. \tag{3.3}$$

The pressure exerted by the whitecap on the surface of the wave is $p_w \propto \rho g h_w \propto \rho_w h a$.

Thus the drag or negative momentum transfer to the wave is:

$$-\frac{\rho_w g}{2c}\frac{\mathrm{d}E}{\mathrm{d}t} = \left\langle p\frac{\partial \eta}{\partial x}\right\rangle \propto \rho_w g a \times ka = 2\rho_w g k E \tag{3.4}$$

Hence:

$$\frac{\mathrm{d}E}{\mathrm{d}t} \propto -\omega E \tag{3.5}$$

This yields a direct dissipation source function that is linear in both the spectral density (wave energy) and the frequency. There is an additional attenuation mechanism attributed to the passage of a whitecapping wave through a field of smaller waves. It is well known (Banner et al., 1989) that the breaking of large scale waves causes rapid attenuation of short waves in its wake. In a continuous spectrum this may be represented by requiring the dissipation source function to depend on the frequency relative to the peak. Both attenuation mechanisms are sensitive to the extent of breaking, which itself depends on the overall steepness of the wave field. Combining these three processes, the dissipation function of the form used in the WAM model (Komen et al., 1984) is obtained:

$$S_{ds} = -C_{ds}\left(\frac{\hat{s}}{\hat{s}_{PM}}\right)^m \left(\frac{\omega}{\langle\omega\rangle}\right)^n \omega E(k) \tag{3.6}$$

where:

$$\hat{s} = m_0 \langle\omega\rangle / g^2 \tag{3.7}$$

and C_{ds}, m and n are fitting parameters, $\langle\omega\rangle$ is the mean radian frequency and $\hat{s}/\hat{s}_{PM}$ is a measure of the overall steepness of the wave field (cf. Eq.(2.52)).

3.2.2 Modeling the spectral dissipation function

Understanding the physics of wave dissipation from a spectral perspective has been so incomplete that the spectral dissipation rate, unlike the wind input and nonlinear transfer, has been inferred indirectly by modeling the evolution of the wave spectrum rather than by pa-

rameterizing known physical features of the dissipation directly (wave breaking, etc.). It is generally recognized that a major part of the wave dissipation is produced by wave breaking; however, many recent experimentally-discovered features of breaking-induced dissipation have not yet been incorporated to wave models (e.g., wave turbulence interaction and wave-wave modulation). Another growing discussion is centered on what physical features have to be excluded from being damped in the spectral models as a result of artificially tuned dissipations. For example, Donelan and Meza in two separate papers presented dissipation functions responsible for the spectral peak downshift. Such a feature does not appear in dissipation functions presently in use, but is consistent with laboratory experiments.

Groundwork was set by Komen et al. (1984) who first demonstrated the possibility of obtaining and tuning a form of the spectral dissipation function based on a rather free interpretation of Hasselmann (1974) analytic model of whitecap dissipation (see Section 3.2.1). Unfortunately, all the tests by Komen et al. (1984) were performed for wind sea growth in the absence of swell, which was later found to have very large spurious effect on the parameterizations (Tolman and Chalikov, 1996). This problem is inherent to the definition of a mean steepness from the entire spectrum, and leads to overestimation of wind sea growth in the presence of swell by as much as a factor of 2 (Ardhuin et al., 2007). Even with the latest modifications to Komen et al.'s formulation by Bidlot et al. (2005). A list of more recent dissipation functions is presented in (WISE Group et al., 2007).

Another significant step was achieved by Young and Banner (1992) who introduced a requirement for the modeled evolution, based on the use of a chosen dissipation function, to reproduce an experimentally known form of the wave number spectrum tail. Spectral models are required to be able to simulate development of the directional spectrum as well as its integral properties, which it was concluded that the Komen et al. (1984) dissipation term could hardly satisfy all the evolution dependence at the same time. Among other conclusions was a demonstration of sensitivity of the evolution results to variations of other than the dissipation source terms. Fixing the high-frequency spectrum tail to an f^{-5} dependence, as in Komen et al. (1984), brought essential changes to the nonlinear term which had to be compensated by additional alterations of S_{ds}. This revealed an ambiguity in verification of the dissipation term on the basis of evolution runs that rely on simultaneous balance of all the sources/sinks.

There is work still in progress on refining the approach of Alves and Banner (2003), based on the local spectral saturation breaking threshold (see Section 3.2.1). Since the major contributor into the spectral dissipation is the wave breaking, the dissipation function should be verified against both its ability to reproduce observed spectral distributions of

wave breaking and against the evolution dependence for spectral and integral properties.

Osuna et al. (2007) implemented this new formulation, which takes into account the nonlinear effect of wave groups on the onset of wave breaking (Alves and Banner, 2003) and obtained that the integrated spectral parameters computed by this new implementation of wave breaking tend to be larger (between 10% and 15% for significant wave height and mean period) than computed with standard formulation of WAM (Günther et al., 1992). Furthermore, Osuna et al. (2007) reduced the negative bias and RMS error computed for the second moment mean period T_{m02}. T_{m02} values computed with Alves and Banner (2003) dissipation term were larger than obtained with Komen et al. (1994) by about 8% and up to 20% during some events. The fact that T_{m02} values were significantly larger seemed to indicate the presence of more energy at swell frequencies for the Alves and Banner (2003), which shall be demonstrated as one of the driving forces behind the recursive underestimation of mean wave periods in the Catalan coast (Section 6.3).

Following is presented an innovative dissipation function that, in the view of the results of this research, it would be very intriguing and strongly recommended to test.

3.2.3 Proposed update of present dissipation function

Tolman and Chalikov (1996) dissipation function The present theory was successfully implemented in the third-generation ocean wave model WAVEWATCH III. Tolman and Chalikov (1996) suggested that the dissipation source term should consist of two constituents due to the fact that different dissipation timescales (low frequencies and high frequencies) are obviously incompatible:

1. a (dominant) low-frequency dissipation constituent: based on an analogy with energy dissipation due turbulence,
2. an empirical high-frequency dissipation constituent.

Tolman and Chalikov (1996) argued that the parametric high-frequency tail, which in WAM is applied for numerical reasons ("disparities in response timescales"; WAMDIG, 1988), might seem a simple way to account for high-frequency dissipation separately. However, a parametric tail fixes the shape of the spectrum, but not the high-frequency energy level α. This level can only be influenced by the frequency dependency of the explicit dissipation source term. High-frequency dissipation thus still influences the shape of the low-frequency dissipation. To avoid this "cross-contamination", the high-frequency dissipation should be described explicitly (cf. WAM high-frequency tail in Section 3.1.3).

In their study, it is assumed that the low-frequency dissipation has a form similar to the energy dissipation due to turbulent viscosity in the boundary layer. On the other hand, the parameterization for high-frequency dissipation is purely diagnostic and is designed to be consistent with the occurrence of a power-law behavior of the equilibrium range.

Low-frequency constituent

The main idea behind this approach is to parameterize the turbulent dissipation of wave energy and associate this sink term to the low-frequency part of the spectrum. In literature, a way to parameterize turbulent dissipation is based on representing velocity and pressure fields in the Navier-Stokes equations as a sum of three components: mean, wave (potential) and turbulent components. Therefore, for example, velocity can be expressed as a superposition of a mean velocity (associated with currents), a wave velocity (associated with the orbital motion of the overlaying waves) and a turbulent velocity. The same applies for the pressure field. If wave motion and turbulence are not correlated, their interaction can be accounted for by introducing an effective turbulent viscosity coefficient K, which depends on the vertical coordinate. This eddy viscosity reduces the kinetic energy of the waves, and it is assumed that a mechanism of mutual adjustment exists between the potential and kinetic wave energy. From this point, the following relationships can be deduced (see Tolman and Chalikov (1996) for detailed description).

$$S_{ds,l}(f,\theta) = -2u_* hk^2 \phi E(f,\theta) \tag{3.8}$$

$$h = 4\left(\int_0^{2\pi}\int_{f_h}^{\infty} E(f,\theta)\mathrm{d}f\,\mathrm{d}\theta\right)^{1/2} \tag{3.9}$$

$$\phi = b_0 + b_1\tilde{f}_{p,i} + b_2\tilde{f}_{p,i}^{-b_3} \tag{3.10}$$

where h is a mixing scale determined from the high-frequency energy content of the wave field and where ϕ is an empirical function accounting for the development stage of the wave field. The linear part of the last equation describes the dissipation for growing waves. The nonlinear term has been added to allow for some control over fully grown conditions by defining a minimum value for $\phi(\phi_{min})$ for a minimum value of $f_{p,i}(f_{p,i,min})$. If ϕ_{min} is below the linear curve, b_2 and b_3 are given as:

$$b_2 = -2\tilde{f}_{p,i,min}^{b_3}\left(\phi_{min} - b_0 - b_1\tilde{f}_{p,i,min}\right) , \tag{3.11}$$

$$b_3 = 8\,. \tag{3.12}$$

If ϕ_{min} is above the linear curve, b_2 and b_3 are given as:

$$\tilde{f}_a = \frac{\phi_{min} - b_0}{b_1} , \tag{3.13}$$

$$\tilde{f}_b = \max\left\{\tilde{f}_a - 0.0025\,,\, \tilde{f}_{p,i,min}\right\} , \tag{3.14}$$

$$b_2 = \tilde{f}_b^{b_3}\left[\phi_{min} - b_0 - b_1\tilde{f}_b\right] , \tag{3.15}$$

$$b_3 = \frac{b_1\tilde{f}_b}{\phi_{min} - b_0 - b_1\tilde{f}_b}\,. \tag{3.16}$$

The above estimate of b_3 results in $\partial\phi/\partial\tilde{f}_{p,i} = 0$ for $\tilde{f}_{p,i} = \tilde{f}_b$. For $\tilde{f}_{p,i} < \tilde{f}_b$, ϕ is kept constant ($\phi = \phi_{min}$). Note that this dissipation disappears in the absence of wind ($u_* = 0$) and/or high-frequency waves ($h = 0$) and hence it is indirectly but strongly linked to the input source term.

High-frequency constituent

Wave energy dissipation for high frequencies is poorly (if at all) understood. Moreover, the entire source term balance for this part of the spectrum is less well known than that for low frequencies, because neither the wind-wave interaction parameter β (Section 2.4.1), nor the nonlinear interactions according to the DIA (Section 2.4.2) are well established in this spectral regime. To be consistent with the parametric tail needed to calculate S_{nl} (Section 2.4.2), the high-frequency dissipation should result in the corresponding one-dimensional frequency spectrum which corresponds to a Phillips or JONSWAP type spectrum:

$$\mathscr{F}(f) = \alpha g^2 (2\pi)^{-4} f^{-5} \tag{3.17}$$

Similarly to the low-frequency constituent, this expression is further developed (see Tolman and Chalikov (1996) for detailed description) and it is eventually found that:

$$S_{ds,h}(f,\theta) = -a_0 \left(\frac{u_*}{g}\right)^2 f^3 \alpha_n^B E(f,\theta)\,, \tag{3.18}$$

$$B = a_1 \left(\frac{f u_*}{g}\right)^{-a_2}\,, \tag{3.19}$$

$$\alpha_n = \frac{\omega^6}{c_g g^2 \alpha_r} \int_0^{2\pi} E(f,\theta)\mathrm{d}\theta \tag{3.20}$$

where α_n is Phillips' non-dimensional high-frequency energy level normalized with α_r, and where α_0 through α_2 and α_r are empirical constants. This parameterization implies that $m = 5$ in the parametric tail. Note that the last equation is solved assuming a deep water dispersion relation (in the model) in which case α_n is evaluated as:

$$\alpha_n = \frac{2k^3}{\alpha_r} E(f) \tag{3.21}$$

The two constituents of the dissipation source term are combined using a simple linear combination, defined by the frequencies f_1 and f_2.

$$S_{ds}(f,\theta) = \mathscr{A} S_{ds,l} + (1-\mathscr{A}) S_{ds,h} \tag{3.22}$$

where

$$\mathscr{A} = \begin{cases} 1 & \text{for} \quad f < f_1 \quad , \\ \dfrac{f-f_2}{f_1-f_2} & \text{for} \quad f_1 \leqslant f < f_2 \quad , \\ 0 & \text{for} \quad f_2 \leqslant f \quad , \end{cases} \tag{3.23}$$

To enhance the smoothness of the model behavior for frequencies near the parametric cut-off f_{hf}, a transition zone is used between the prognostic spectrum and the parametric high-frequency tail. The frequencies defining the transitions and the length scale h are predefined in the model.

Summary

The physics of wave energy dissipation are still largely unknown, and the dissipation source term was similarly used in Tolman and Chalikov (1996) as a tunable closure term in the

wave energy balance equation. The main contribution to understanding the wave energy dissipation is the distinction of two separate dissipation regimes dominated by incompatible dissipation timescales.

The high-frequency dissipation covers only a fraction of the total spectral energy and has to be purely diagnostic. It does not yield physical insight since high-frequency dissipation is directly derived from the other source terms. Note that depending on the parameterization of S_{in} and S_{nl}, and for different shapes of the parametric tail, the parameterization of high-frequency dissipation needs to be reassessed. It was somewhat arbitrary to describe the low-frequency dissipation with a turbulence analogy. The dependence of this source term on the function ϕ makes the final definition to some extend a tuning exercise. There is a potential shortcoming in the low-frequency dissipation and it is directly related to the input through the friction velocity u_* and its vanishing when $U_{10} \to 0$. In such conditions, steep swells will not be dissipated, which are, however, mostly due to strong effects of shoaling or due to wave-current interactions, where both of which are expected to be relevant in relatively small-scale implementations only.

3.3 Routines implemented in wave data handling

In this section a review of some of the techniques involved in favor of the goal of developing an insightful validation of wave estimates is provided. It is not attempted to fully cover the mechanics of these schemes but to understand the need and benefits of their implementation.

3.3.1 Routine Analysis of Pitch-and-Roll buoy Wave Data

First, in order to examine the spectral evolution of the selected storms it shall be necessary to process raw data from pitch-and-roll buoys and reconstruct corresponding two-dimensional directional spectra.

The technique based on the pitch-and-roll buoy has undoubtedly been used most frequently (Kuik et al., 1988). For such pitch-and-roll buoy, a large variety of analysis methods can be used and they are all based on a cross-spectral analysis of the three basic heave and slope signals of the buoy. For the present study, WAFO Matlab Toolbox is used for analysis of waves (WAFO-group, 2000).

Pith-and-roll buoys measure the elevation and slope (two directions) of the sea surface as a function of time. From these three time series, one can determine the one-dimensional energy-density spectrum $E(f)$ and some information about the directional distribution of

the energy. The two-dimensional energy spectrum can be decomposed into the directional spreading as a function of the frequency and the one-dimensional frequency spectrum (3.24):

$$E(f,\theta) = E(f)D(f,\theta) \rightarrow D(f,\theta) = \frac{E(f,\theta)}{E(f)} \tag{3.24}$$

in which $E(f)$ is the frequency spectrum:

$$E(f) = \int_0^{2\pi} E(f,\theta)\mathrm{d}\theta \tag{3.25}$$

The dimensional spreading for a given frequency $D(\theta)$ can be approximated with a truncated Fourier series (Longuet-Higgins et al., 1963):

$$D(\theta) = \frac{1}{\pi}\left\{\frac{1}{2} + \sum_{n=1}^{\infty}\left[a_n\cos(n\theta) + b_n\sin(n\theta)\right]\right\} \tag{3.26}$$

The buoy only gives the first four Fourier coefficients after the post-processing (from the autospectra and cross spectra of elevation and slope). Therefore, only $n = 1,2$ is to be considered (a_1, b_1, a_2 and b_2).

There are two classes of methods: the first class methods attempt to reconstruct the directional energy distribution (at each frequency), whereas the second class estimate some characteristic directional parameters (at each frequency).

Reconstruction methods intend to approximate the directional distribution $D(\theta)$ by only using the first four Fourier coefficients of the directional energy distribution per frequency. However, it may lead to negative values (while $D(\theta)$ is defined positive by definition). The methods of parametric models are based on an a priori assumed shape of the directional energy distribution but the number of independent shape parameters should not be more than four. A commonly used shape for the directional distribution function is given by Longuet-Higgins et al. (1963) and Kuik et al. (1988):

$$D(f,\theta) = A\cos^{2s}\left(\frac{\theta-\theta_m}{2}\right) \tag{3.27}$$

where θ_m is the mean wave direction, $s(f)$ is a parameter which controls the directional width of $D(\theta)$, and A is a normalization constant. The normalization factor A is computed in such a way that the following property of the directional distribution is satisfied:

$$\int_0^{2\pi} D(f,\theta)\,\theta = 1 \tag{3.28}$$

and the directional width parameter $s(f)$ is computed from the direction spreading $\sigma(f)$, following Kuik et al. (1988):

$$\sigma(f) = \left(\frac{2}{s(f)+1}\right)^{1/2} \tag{3.29}$$

3.3.2 Spectral partitioning

A wave spectrum describes the distribution of the total wave variance over frequency and direction. Such a distribution is the result of the occurrence of a certain number of individual wave systems originating from different meteorological events. Integral parameters rather than whole spectra are preferred. However, while integral parameters describe suitably a wave spectrum composed of a unique wave system, the simultaneous occurrence of different wave systems turns integral parameters less meaningful, unless they refer to individual wave components. Partitioning of wave spectra into independent wave systems provides an excellent tool for comparison of data sets or when evaluating model performance, the analysis at the level of wave systems gives more insight in processes than the analysis of mean parameters of the whole spectrum (e.g., Portilla, 2009).

In the WAM model (Komen et al., 1994) in particular, although the wind wave generation mechanism actually implemented is the one given by Janssen (1991), the identification of wind-sea and swell is based on the formulation of Komen et al. (1984) (Eq 3.30).

If two-dimensional spectrum and wind information is available, a straightforward step to identify wind-sea and swell is to apply a definition for wind-sea. The sea spectrum is the part of the total spectrum, which is under the influence of the local wind speed. The remaining part of the total spectrum is called swell. The term "under the influence of the local wind speed" means that the phase speed of the wave–components is less than the friction velocity assigned to local wind speed component. If U_{10} denotes the wind speed and θ_w the wind direction in 10 m above sea surface, a spectral component $E(f,\theta)$ is defined as swell if:

$$\frac{g}{2\pi f} > 1.2\eta u_* \cos(\theta - \theta_w) \tag{3.30}$$

where the friction factor $\eta = 28$.

The disadvantage of applying such an equation to each grid point is that the frequency direction area that fits the wind-sea-swell criterion, does not necessarily corresponds with a wave system and the spectrum is split even in situations where it is composed of only one wave system. Not surprisingly, more consistent results in terms of wave systems are obtained if partitioning is used (Portilla, 2009).

Chapter 4

Region of study and data used

4.1 Region of study

4.1.1 Location

The area of study is located on the Catalan coast, in the Northwestern Mediterranean, at a latitude between 40°45′N to 42°25′N and longitude between 0°45′E to 3°15′E (see Fig. 4.1). The so-called Northwestern Mediterranean Sea spans from Italy to the Straits of Gibraltar and hence will become the broadest domain taken into account in the present study.

With a surface area of 32,107 km^2, Catalonia has a very diverse and divided orography, with extensive mountain ranges mirroring the coastline, inland depressions, mountain peaks reaching 3,000 km high in the Pyrenees, and just 240 km to the south is a delta that collects the sediments from one of the most abundant rivers of the Iberian peninsula: the Ebro.

The Costa Brava begins where the Pyrenees subside to meet the Mediterranean, and this coastline stretches for 214 km, alternating between rocky areas with numerous coves and some very expansive beaches to the gulf of Roses and Estartit-Pals. The coast continues running southwards and it is 547 km long. The section from the Maresme to the Ebre Delta is mainly flat with large beaches.

Some environmental properties of the Northwestern Mediterranean are highly conditioned by the fact that it is a semi-enclosed sea. Local high and low pressure weather systems are controlled by orographic barriers that determine the spatial distribution of winds and land–sea temperature differences. A comprehensive description of the main features controlled by orography are given in Section 4.1.2.

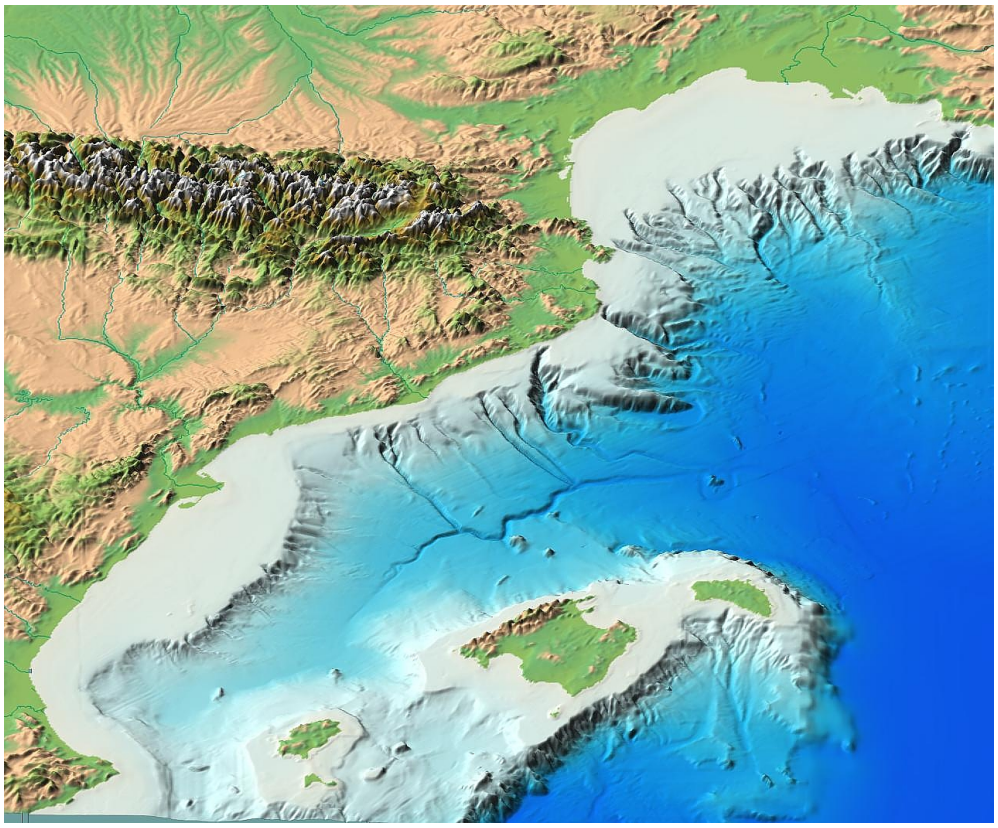

Fig. 4.1 Orography of the Balearic Sea (BS). (Source: Departament de Geociències Marines de l'Institut de Ciències del Mar (ICM). Available from: http://ww2.icm.csic.es/gma/en/content/home/).

4.1.2 Bathymetry

The bathymetry presents a narrow continental shelf northwards the Ebro delta (Tarragona) until the coast of Barcelona, where the 800 m isobaths are only 15 to 20 km offshore. Towards the south, the Ebro Delta is a geographical feature characterized by a gently sloping bathymetry which results in a wider continental shelf.

On the other side, from Barcelona up to the Gulf of Lion, the continental shelf is increasingly wider, exhibiting several very deep canyons. Continental slopes are at the transition between shallow continental shelves and deep basins and are often cut by these submarine canyons. They represent the steepest part of continental margins, which extend from the shelf break, usually at depths of 100–200 m, to the upper continental rise at depths of 1,500–3,000 m. At final spatial and temporal scales, continental-slope morphological features form as a result of mechanisms governed by erosional and depositional processes.

Blanes canyon (41°30′N,2°51′E) and La Fonera canyon (41°51′N,3°24′E), in front of Blanes and Palamós respectively, are the two major submarine canyons. They are are de-

picted in the Fig. 4.2.

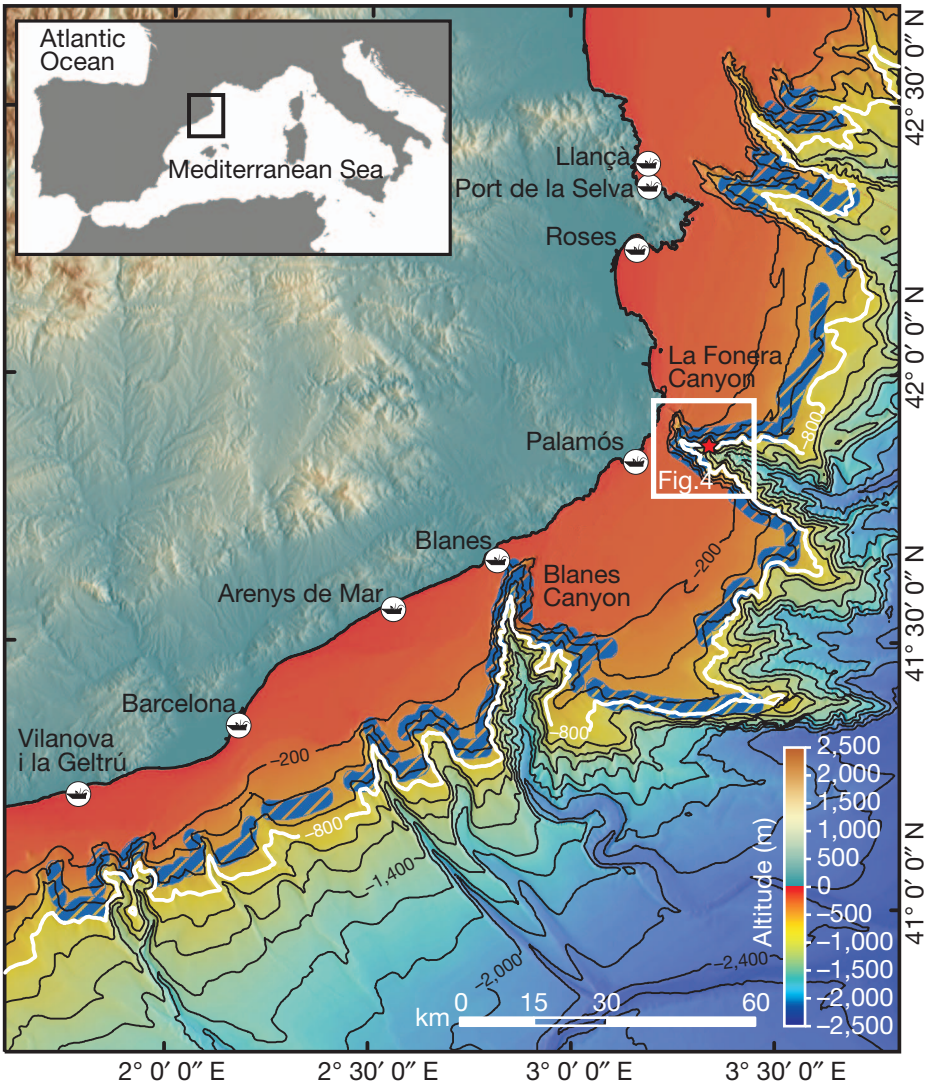

Fig. 4.2 Bathymetric map of the northern Catalan margin (Northwestern Mediterranean Sea) showing the main trawling grounds on the open continental slope and canyon flanks. (Source: Puig et al., 2012).

4.1.3 Wind

The Pyrenees are a physical barrier that strongly modify the wind patterns and produce the so-called Mistral and Tramontane winds in France. The Mistral wind is a typically cold wind flowing towards the Gulf of Lion, coming from the northwest, after sinking and cooling down through the Pyrenees mountain range. These winds are one of the main contributing factors to Mediterranean storms (Flamant et al., 2003) and frequently extend several hundreds of kilometers off the coast, bringing cold and dry air over the Northwestern Mediterranean. They are considered among the most intense and powerful winds due to their high velocities and persistence.

The predominant winds are: NE (Gregale), E (Levant), SW (Garbi) and NW (Mistral). Mistral winds produce local sea characterized by short periods, mainly prevailing between October and May. In winter (February, November), easterly winds are generated by low-pressure centers over the Western Mediterranean. Highest velocities have been registered from these wind directions (Levant). Southwesterly winds usually predominate during the summer (Sánchez-Arcilla et al., 2008) when a high-pressure system takes place in the south of Europe, bringing warm air from the North of Africa.

The Ebro delta certainly is the largest geographic feature directly influencing the atmospheric and oceanographic nature of the Catalan coast. During regional northerly winds, the orography favors wind channeling down the Ebro river and off the Ebro delta. The evolution of wind coastal jets is particularly relevant on this area. Such features carry the most weight at the generation of high wind-seas in fetch-limited conditions directed towards the southeast. The evolution of the air flow channeling through the Ebro river valley can be observed in Fig 6.14.

In the figures below (Fig. 4.3) are shown the wind roses provided by Puertos del Estado at the buoy of Tarragona (Ebre deep). They have been generated from a 10 years' time series (from 2004 to 2014) at such a buoy. From these figures it is observed that predominant directions (coming from) are northwest (mainly during winter and autumn), east and south (during spring and summer).

4.1.4 Waves

The directional distribution of waves in the region agrees with the wind climate and shows a predominance of northwestern and eastern wave conditions, and some southern wave systems. Hence, northwestern waves are associated with Mistral and Tramontane winds under fetch-limited conditions typically occurring during the winter season (see Fig. 4.3a), as pre-

viously introduced. Eastern waves are related to swell wave trains originated far offshore by storm systems. This wave pattern displays a fairly steady behavior throughout the year and largely independent of the local wind field. Additionally, southern wave systems are typically accentuated during the summer months due to the predominance of southwestern winds (Sánchez-Arcilla et al., 2008).

The largest waves come from the east and northeast, which are the directions along the longest fetch. Double peaked (bi-modal) wave conditions are often observed under strong local north-western winds and offshore eastern (or southern) winds (Sánchez-Arcilla et al., 2008), especially in the Ebro Delta region, where these bi-modal spectra can occur more than 50% of the time (Bolaños et al., 2009).

4.1.5 Tides

The Catalan coast is characterized by a microtidal environment. In this low-tide region, circulation is characterized by a quasi-permanent slope current (the Northern Current) that can be modified by meso-scale events. These events consist of current meandering or eddies and constitute the main dynamic agent of the coastal ecosystems. The coastline is 700 km long and includes a wide variety of coastal systems. This results in considerable geomorphological and biological diversity.

The variations of sea level in the Mediterranean Sea due to tides are not as important as in other larger seas or ocean domains (Bolaños et al., 2009). According to these authors, the tidal oscillations are in the order of 10-30 cm. It was also reported that the mean current intensity at a depth of 100 m was approximately 10 $\mathrm{cm\,s^{-1}}$, although it may strengthen during the winter, reaching up to 40 $\mathrm{cm\,s^{-1}}$.

Due to the minor influence of the tidal levels and currents, in the present work they will not be taken into account since its effect on the estimation of the wave fields is minimal (Bolaños et al., 2011).

4.2 Data available

4.2.1 Observational data

Oceanographic instruments

Xarxa d'Instruments Oceanogràfics i Meteorològics, XIOM The XIOM buoy network (Xarxa d'Instruments Oceanogràfics i Meteorològics) was created in 1984 aiming to obtain

measurements and thus provide a better tracking of the Catalan littoral evolution. During the following years, the network grew and implemented new instrumentation. For the present study, the Ebro delta (Tortosa) buoy will be of use. It was deployed in 1990 due to the constant retreat of the coastline at the Ebro delta (Sánchez-Arcilla et al., 2008) and has continued in operation until 2014, when it was withdrawn due to lack of funding. In addition, two more buoys will be considered in order to ensure a larger representativeness of the model validation. These are the buoy of Blanes and the buoy of Llobregat. In the following, more attention is given to the buoy of Tortosa, although the main characteristics of the remaining buoys can be found in Table 4.3.

The buoy of Tortosa is a directional buoy (Directional Waverider MKII) manufactured by Datawell, provided with a stabilized platform sensor, performing heave and direct pitch and roll measurements combined with a 3D fluxgate compass and X/Y accelerometers. It is located at 60 m depth and approximately 8 km away from the coastline. Further specifications are shown in the Table 4.1.

Table 4.1 Description of the buoy of Tortosa belonging to XIOM.

Buoy	Tortosa
Coordinates	40°43′12″N , 0°58′48″E
Depth [m]	60
Diameter [m]	0.9
Sample interval [s]	1/1.28
Resolution	cm
Type of buoy	Directional
Record duration [min]	20
Available recorded period [years]	1990-2012

Wave buoys provide two types of data: (a) processed data which are immediately transmitted and are calculated both statistically and spectrally, (b) raw data which are stored in the buoy's memory and need to be collected in situ. Processed data can be directly used and contain information regarding integral parameters, among others, such as the wave height, period or predominant direction, although it is not possible to obtain the mean spectrum (either scalar or directional).

It is known that raw data recording frequency is not constant and many gaps occur due to either buoy breakdowns or computing problems. The memory requirement of the raw data (of surface elevations) is high. In situations where such memory is unavailable, only the relevant parameters of the surface elevation such as, for example, the significant and maximum wave heights are sent to the control station, and then the rest of the recorded

information is deleted.

Table 4.2 Time series available of processed data from Tortosa buoy.

Year	No. obsevations	Year	No. observations
1990	1795	2002	6505
1991	2775	2003	5814
1992	3138	2004	7372
1993	3175	2005	6120
1994	2623	2006	7566
1995	2177	2007	7780
1996	2016	2008	8019
1997	1975	2009	8021
1998	1634	2010	8315
1999	3188	2011	7740
2000	5826	2012	1558
2001	5397		

Puertos del Estado, PdE Puertos del Estado, the Spanish national port authority since 1996, controls a water buoy network around the coast of mainland Spain, the Canaries and the Balearic Islands. Data are provided from different typology of buoys and simulation points. In the present research, however, support in such databases has been considered not to be necessary since more suitable information is provided by the XIOM buoy network.

The above different observational instrumentation supplies oceanographic data at the Catalan coast and has monitored the evolution of the principal hydrodynamic processes and extreme events that have stricken the shore.

Below the Table 4.3 displays the general properties associated with all buoys belonging to both Puertos del Estado and XIOM. Note that most of them shall not be used in the coming validation process.

4.2.2 Forecasted data

Wave models

Numerical wave prediction models were formulated in terms of the basic energy transport equation for the two-dimensional wave spectrum (see Eq.(2.18)). However, none of those models actually computed the wave spectrum from first principles alone from the spectral transport equation. Additional ad hoc assumptions were introduced in order to force the

Table 4.3 Description of principal buoys at the Catalan coast.

Latitude	Longitude	Depth [m]	Type of buoy	Identifier	Buoy network
40°43′12″N	0°58′48″E	60	Directional	Tortosa	XIOM
41°16′48″N	2°8′24″E	45	Scalar	Llobregat	XIOM
41°39′0″N	2°49′12″E	74	Scalar	Blanes	XIOM
42°10′48″N	3°11′60″E	46	Scalar	Roses	XIOM
40°40′48″N	1°28′12″E	688	Directional	Ebre deep	PdE
41°4′12″N	1°11′24″E	15	Scalar	Tarragona	PdE
41°19′12″N	2°12′36″E	68	Directional	Barcelona	PdE
41°49′48″N	3°11′24″E	90	Directional	Palamós	PdE
41°55′12″N	3°38′60″E	1,200	Directional	Begur deep	PdE

spectrum to comply with some preconceived notions of wave development that could not be readily expressed by the source function used in the transport equation.

First generation models avoided explicitly modeling the complete energy balance. It was assumed that wave components suddenly stopped growing when they reached a universal saturation level. Thus, for growing wind-seas, the prognostic region of the modeled spectrum was limited to wave components close to the spectral peak. Furthermore, it is known that first generation models overestimated the wind input and underestimated the strength of the nonlinear transfer.

In the 1970s, wave growth experiments lead to a change on the view of the spectral energy balance resulting in a development of second generation wave models. However, for these models also, restrictions due to simplified nonlinear transfer parameterization required the spectral shape of the wind-sea spectrum to be prescribed for frequencies higher than the peak frequency. Second generation models were unable to properly simulate complex wind-seas generated by rapidly changing wind fields. The models also lacked in the treating the transition between wind-sea and swell.

Third generation wave prediction models were born under the conception of overcoming the numerical limitations that the previous models had experienced. These new models would allow the wave spectrum to be computed alone by integration of the basic spectral transport equation, without any prior restriction of the spectral shape. The first third generation wave model presented was the WAM (WAve Modeling) program (WAMDIG, 1988).

In order to remove restrictions on the spectral shape, two steps were needed:

First, a parameterization of the exact nonlinear source function had to be developed that contained the same number of degrees of freedom as the spectrum itself since models that do not share the same number of degrees of freedom between spectrum and nonlinear transfer

parameterization are unstable. In the present model, the discrete interaction approximation of Hasselmann et al. (1985) is used, which retains the same cubic operator structure as the original Boltzmann integral.

Second, the energy balance had to be closed by specifying the unknown dissipation source function. The input source function was adopted from measurements of Snyder et al. (1981) whereas the dissipation source function corresponds to the form introduced by Komen et al. (1984) on the basis of a series of numerical integrations of the transport equation using prescribed source function for the input and exact computations of the nonlinear transfer. The dissipation was tuned to reproduce the observed fetch-limited wave growth and the fully developed Pierson-Moskowitz spectrum.

It is still needed to readjust the source functions; however, it was expected that further modifications should only be required in the source functions representing the physics, rather than modifying the form of the resultant wave spectrum.

Atmospheric models

In this section the main providers of regional simulated wind data are introduced:

MM5 The MM5 (Fifth-Generation NCAR / Penn State Mesoscale Model) is a forecasting non-hydrostatic and limited area meteorological model designed to simulate mesoscale atmospheric circulations. These include those phenomena which occur at spatial scales ranging from a few kilometers to a few hundred, such as storms, breezes, or frontal systems among others. Despite being a model that is no longer under development, is still used in many operational centers.

WRF WRF (Weather Research and Forecasting Model) is a forecasting numerical model designed for operational and research applications. One of its objectives is precisely to accelerate the introduction of advances in research to operational processes. Currently, WRF can use a broad range of scales, which can act as a large-r or small-scale model, allowing very high resolution simulations.

Specifically, it has been implemented the version known as WRF-ARW (Advanced Research WRF), developed under the leadership of NCAR (National Center for Atmospheric Research, USA) and operates as a limited area model with the aim of simulating mesoscale atmospheric circulations. These include those phenomena which occur at spatial scales between a few kilometers to a few hundred.

The model uses terrain-following, hydrostatic-pressure vertical coordinate with the top of the model being a constant pressure surface. The component programs of the WRF Modelling System exchange data between each other. The structure of the model can be roughly understood by assuming the same three main programs that characterize the WAM Model: a pre-processing (reading the inputs and re-writing in terms of the model, so that the main program can use such data), main (computing the physics of the model) and post-processing (outputting results into specific formatted files) systems.

The Weather Research and Forecasting model (WRF) was designed as the successor to MM5 and includes all capabilities available within the MM5. Given the relatively larger implementation, the tuning of the wave model's dissipation function shall be based on WRF winds and MM5 are not considered further.

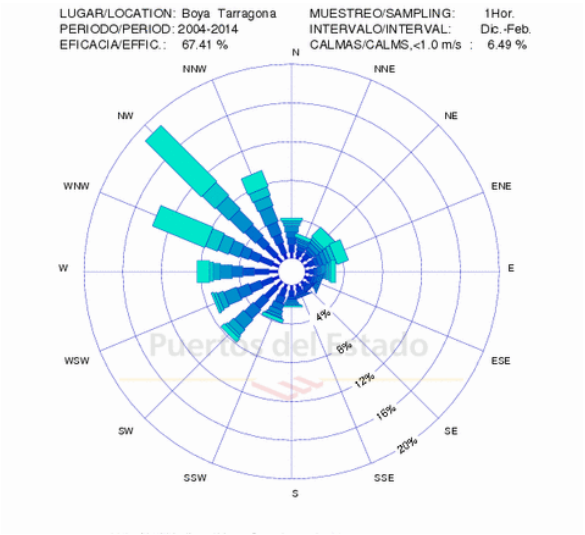

(a) Winter season

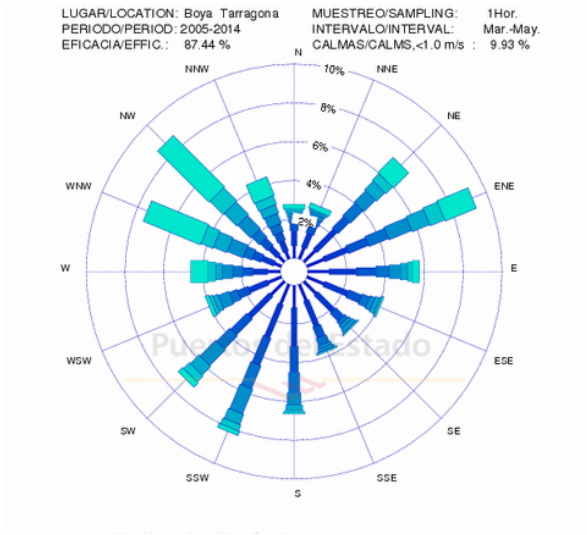

(b) Spring season

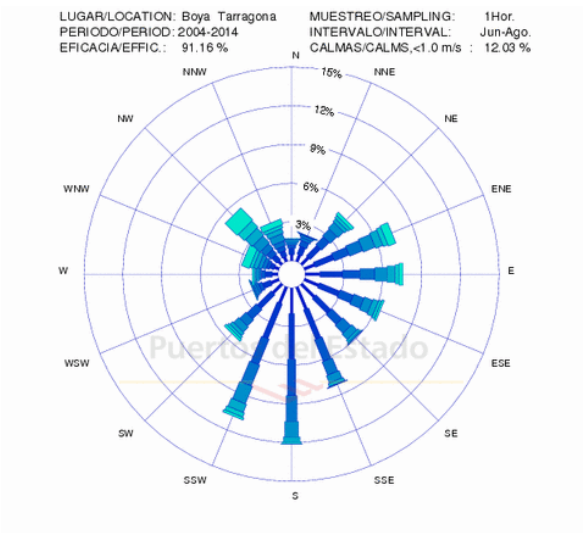

(c) Summer season

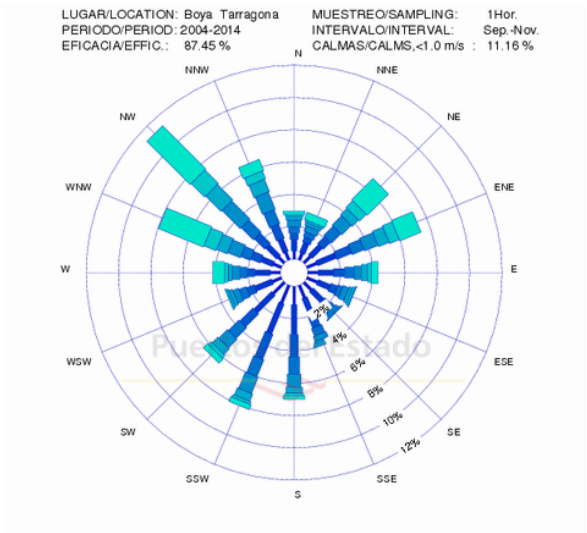

(d) Autumn season

Fig. 4.3 Wind roses (U_{10}) at the buoy of Tarragona (Ebro deep) belonging to Puertos del Estado. Each partition represents 1 $\mathrm{m\,s^{-1}}$.

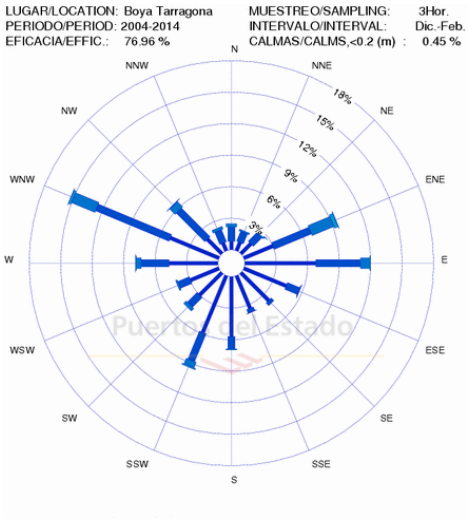

(a) Winter season

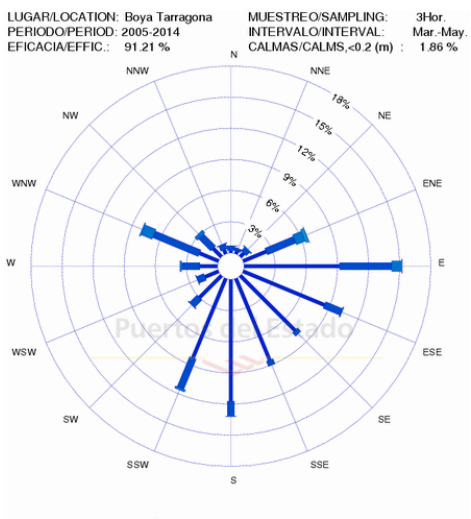

(b) Spring season

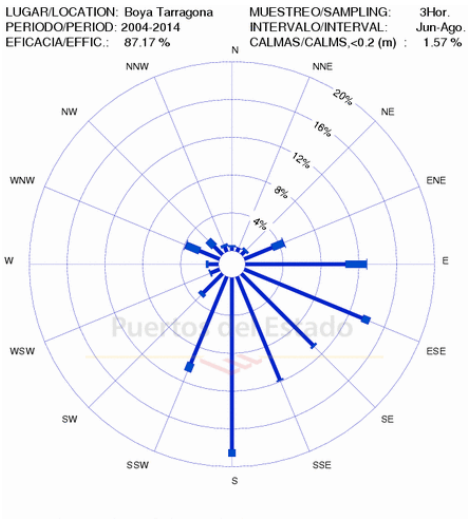

(c) Summer season

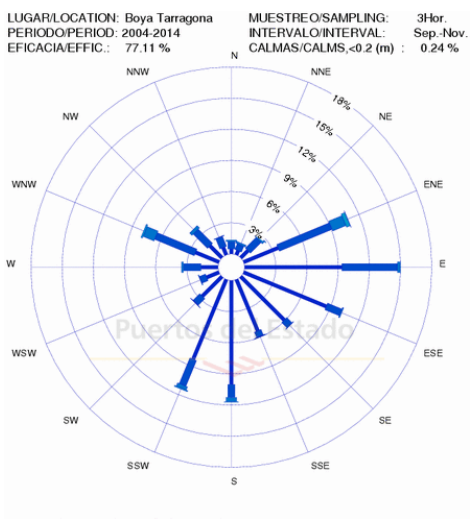

(d) Autumn season

Fig. 4.4 Wave roses (H_s) at the buoy of Tarragona (Ebro deep) belonging to Puertos del Estado. Each partition represents 1 m.

Chapter 5

Study interval and set-up of the WAM model

A review of the main settings of the WAM wave model is given in Section 5.1. The characteristics of the computational, bathymetric and forcing input grids are provided, as well as further aspects that have been taken into account. Subsequently, Section 5.2 introduces the selected study interval and a general description of the main properties is given. Wave model results and discussion are detailed in the following chapter in order to keep the pre-processing and post-processing separate from each other. Lastly, Section 5.3 presents a set of validation tools that shall be used in the following chapter to carry out statistical analysis of the results.

Appendix A presents a review of the wave model structure and further relevant features.

5.1 Relevant features and set-up of WAM wave model

In this study, WAM Cycle 4.5.3 was used for the wave simulations (Günther and Behrens, 2011). Although the physics of the model have already been introduced in the Chapter 2, there are several aspects that are presented in this new update of the model. WAM Cy 4.5[1] is an update of the WAM Cy 4 wave model, which within the last twenty years it has become a standard tool for operation wave prediction and engineering application, and which is described in Komen et al. (1994) and Günther et al. (1992). The basic physics and numerics are kept in the new release, although several improvements have been incorporated such as the source function integration semi-implicit scheme made by Hersbach and Janssen (1999)

[1]WAM Cy 4.5.3 and WAM Cy 4.5 are herein mentioned indistinctly since no major changes (minor bug fixes) exist between both versions as for the purpose of this research.

and technical improvements, which take into account the new possibilities of Fortran 90. On this matter, among other features, this new update has allowed the output of spectra at specific output sites and multiple nesting in the coarse grid, which shall be of great utility in this research (see Günther and Behrens (2011) for further information).

The present study is then focused mainly on the Catalan coast and it will therefore be the spatial domain where simulations shall be carried out. As it was already introduced in Section 4.1.1, the coast extends from the coastline of Portbou, the northernmost Catalan municipality, to the mouth of the river La Sènia, south of the Ebro delta. The considered domain is then located between the latitudes 40°45′N and 42°25′N and the longitudes 0°45′E and 3°15′E, with an approximately overall extension of 700 km.

Wave and depth maps The model is executed in third generation and non-stationary mode with spherical coordinates. The computational grid covers the Western Mediterranean Sea (WM) and a finer, nested grid incorporating the entire Balearic Sea (BS) shall be implemented. These two grids are the so-called computational grids and they comprise the domains where the model will execute computations upon (see Table 5.1).

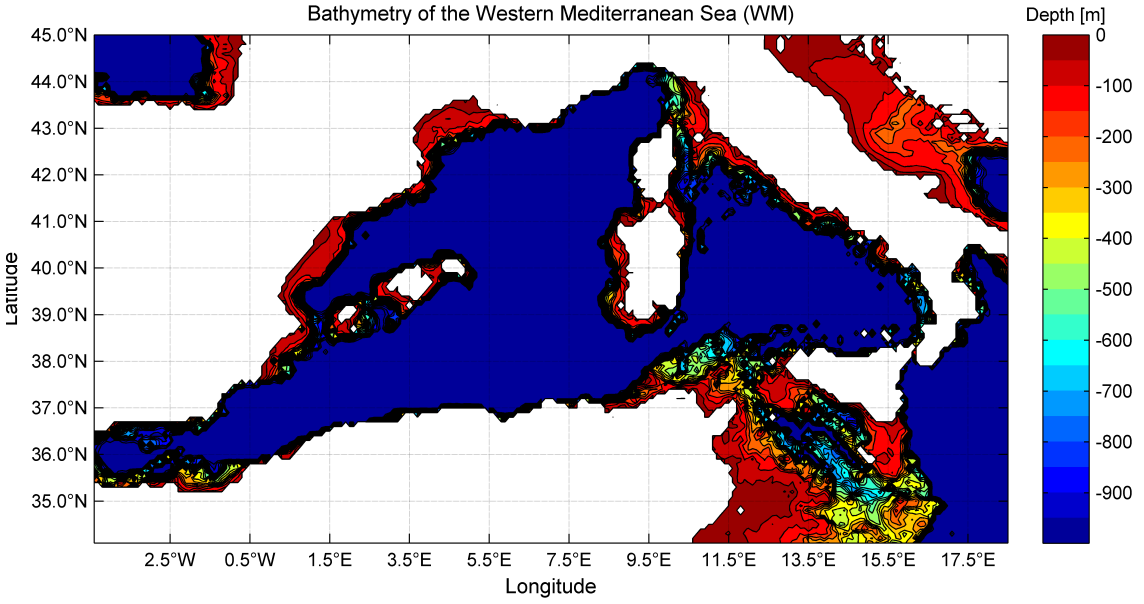

Fig. 5.1 Bathymetry of the Western Mediterranean Sea (WM).

The bathymetry database that will be used throughout the entire study is enclosed in a ASCII text document and has been pre-processed with the wave model. For its requirements, two domains have been computed from such a file (using a bilinear interpolation scheme,

in order to yield a resolution approximately equal to the computational grids'). The more extensive covers the whole Western Mediterranean Sea (see Fig. 5.1) and the nested, high-resolution includes the Catalan coast and the Balearic Sea (see Fig. 5.2). The characteristics of these grids are shown in Table 5.2.

Table 5.1 Computational grids implemented in the wave model run for both Balearic (BS) and Western Mediterranean Sea (WM).

	Western Mediterranean Sea (WM)	Balearic Sea (BS)
Longitudes	4.95°W - 16.00°E	0.45°W - 5.58°E
Latitudes	35.10°N - 44.62°N	39.00°N - 43.66°N
Mesh size	196×119	168×173
Grid resolution	9 km (0.107°×0.081°)	3 km (0.036°×0.027°)

Table 5.2 Grids implemented for the creation of the bathymetry file for both Balearic (BS) and Western Mediterranean Sea (WM).

	Western Mediterranean Sea (WM)	Balearic Sea (BS)
Longitudes	4.95°W - 17.95°E	0.83°W - 5.68°E
Latitudes	34.05°N - 44.95°N	38.43°N - 43.95°N
Mesh size	230×110	218×185
Grid resolution	9 km (0.1°×0.1°)	3 km (0.03°×0.03°)

The buoys that are depicted in Fig. 5.2, have been placed according to the bathymetric grid. However, the model is ordered to output integral parameters and spectra at specific locations (buoy) during the post-processing phase.

Wind The atmospheric forcing data used as main input to the WAM model were the daily wind fields (four analyses fields per day, at 00:00, 06:00, 12:00, and 18:00 h) of the wind velocity at 10 m from the WRF atmospheric model (see Section 4.2.2). This database provides gridded data (spatial resolution: 0.1° in longitude, 0.1° in latitude) with a temporal resolution of 6 h. Table 5.3 shows the dimensions of the grids implemented in the atmospheric model. It is noticeable that the size of such a mesh is slightly larger than the computational grid implemented by the wave model (cf. Table 5.1).

The first wind domain covers the full Western Mediterranean Sea (WM), with a spatial resolution of 0.1° (roughly 9 km); new wind files are updated every 24 h with a temporal resolution of 6 h. The input time step, however, is 3 h and the output time step is 1 h, leading to hourly results (note that this is not the temporal resolution of the actual wind field). The

smaller computational grid, covering the Balearic Sea (BS), is forced by a second wind field with a spatial resolution of 0.03° (roughly 3 km) and a similar temporal resolution of 6 h, with both input and output time steps of 1 h.

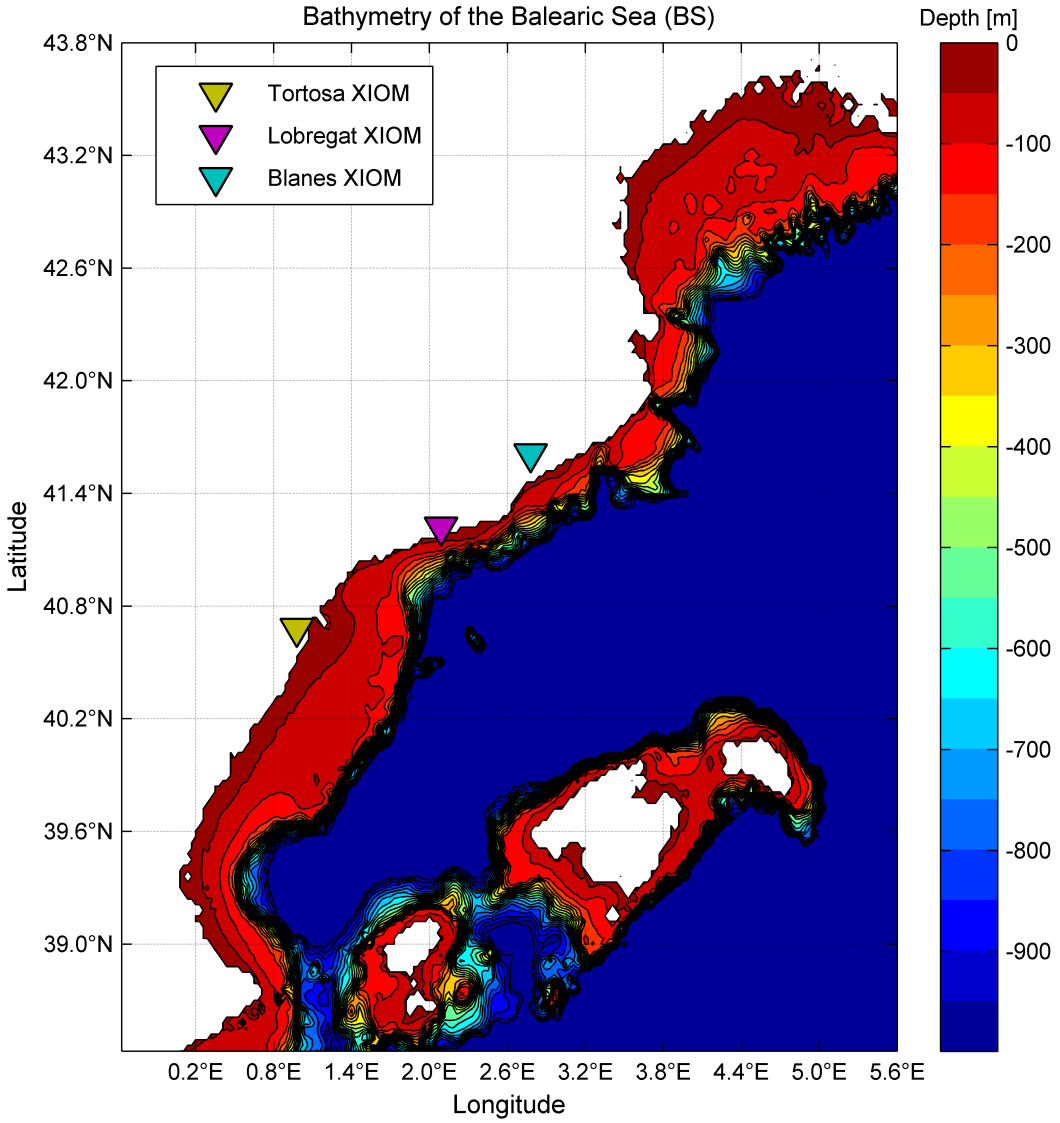

Fig. 5.2 Bathymetry of the Balearic Sea (BS).

Time-steps It has been used a time step of 3 min for the propagation scheme and also 3 min for the implicit scheme with regard to the source terms computation for the large grid (Western Mediterranean Sea). Since the resolution of the nested domain is larger, shorter time steps for both the propagation and source terms schemes are set by default (90 s for

both).

Table 5.3 Grids implemented in the computation of the atmospheric model run (WRF).

	Western Mediterranean Sea (WM)	Balearic Sea (BS)
Longitudes	5.00°W - 18.00°E	0.83°W - 5.68°E
Latitudes	34.05°N - 45.00°N	38.43°N - 43.95°N
Mesh size	231×110	218×185
Grid resolution	9 km (0.1°×0.1°)	3 km (0.03°×0.03°)

Frequency range The frequency range considered is chosen according with the buoy frequency domain, which is 0.03–0.625 Hz. Values are logarithmically spaced with a frequency resolution of $\mathrm{d}f/f = 0.1$. Therefore, in order to determine the exact number of frequency values the following rule has been applied:

$$0.03 \times 1.1^{\mathrm{ML}-1} = 0.625 \tag{5.1}$$

resulting in 33 frequency values that range from 0.03 Hz to 0.633 Hz. According to Pallares et al. (2014), with this adjustment only one part of the total energy spectrum is integrated and therefore a part of the total energy corresponding to the higher frequencies is not being considered, leading to a decrease of the wave momentum and their derived parameters. This effect can be enhanced for spectra with more energy in higher frequencies (wind-wave dominated storm events), where a part of the energy is located outside the integration range considered for the validation. Nevertheless, this adjustment is essential in order to compare model results with instrument measurements under the same terms.

Initialisation and model Boundaries Additionally, the model runs are computed using a cold start. When enabled, the initial state of the sea surface is equal at every grid point ($\eta = 0$). If existence of wave trains at $t = 0$ would have large influence in the model simulations, it would be advisable to impose a different initial state of the sea surface. It has been observed, however, that the generation of wave forcing at the southern boundary of the coarse grid (WM), between the longitudes 10°E and 12°E, lead no changes in the estimations at the three buoy stations and, therefore, cold stat option were eligible. Note that this is only implemented at the very first step of the computation run; every new step assumes that the initial sea state is equal to the previous time step.

That concludes the processing control parameters set-up, and definition of parameters regulating the post-processing follows below.

Partitioning scheme The WAM model is characterized by computing the total spectra at each grid point. However, the results (integral parameters and spectra) may be requested for the total, swell or wind sea spectrum. It is during the post-processing phase that the model implements a partition technique on the total spectra from which both swell and wind sea spectra are derived. On the basis of the assumption that spectral components for which $u_{10}/c < 1$ receive a no direct atmospheric forcing (Komen et al., 1984), the corresponding subroutine of the WAM model assigns the value of the total spectrum to swell. Once the swell spectrum is defined, the wind sea spectrum results from the subtraction of the total and the swell spectrum (cf. Section 3.3.2).

Definition of specific output locations Other requirements that are commanded during the post-processing phase are specific output locations where spectra and parameters are solicited. The model uses the values found during the computations at each neighboring node of the grid and obtains such estimates at those locations via interpolation. Four instruments are used for the calibration and are shown in the Table 5.4.

Table 5.4 Locations of wave measurement stations.

Instruments	Blanes (XIOM)	Llobregat (XIOM)	Tortosa (XIOM)
Longitudes	2.82°E	2.14°E	0.98°E
Latitudes	41.65°N	41.28°N	40.72°N
Depth	74 m	45 m	60 m

5.2 Study interval

The principal reason that shall determine the choice regarding the study interval is the existence of available wind fields. Since some of the computations, including both the atmospheric and oceanographic models, were carried out at the Laboratori d'Enginyeria Marítima (LIM–UPC), the wind database that served as input of the WAM model was itself already obtained from the WRF-ARW or MM5 models at the laboratory. Information about those computations is shown in Section 5.1.

Therefore, the study interval from which the validation is based on begins on January 6, 2010, and finishes on January 18, 2010. During this period of observation, waves were

monitored by several wave-measuring instruments although the study presented herein uses three main buoys (Tortosa, Llobregat and Blanes). However, special emphasis has been placed upon the buoy of Tortosa due to the aforementioned reasons (Chapter 4).

Plotted below (see Figs. 5.3, 5.4 and 5.5) are the time series of the buoys of Tortosa, Llobregat and Blanes covering the period of interest. It is noticeable from the Fig. 5.3 that time series of the buoy of Blanes do not hold data during the first days of the selected period (up to January 14, 2010). This is due to the fact that, for a lapse of time, this device worked as a scalar buoy and directional time series may exhibit considerable interruptions (the same occurred at the buoy of Llobregat).

Data from time series have been filtered in order to isolate the different storm events. Visual identification criteria (steep increase of h_{m0} and eventually a relatively milder decrease) matched with quantitative criteria (when the threshold is exceeded).

Furthermore, selection of storm events shall be based upon a reasonable threshold of 1.5 m of significant wave height during more than 6 h (Bolaños, 2004). The maximum time span in between independent storms during which the threshold is not to be exceeded is set to 24 h. The latter condition is commonly used for extreme analysis since storms (stochastic events) need to be independent. Here, however, short-term analyses do not require this condition. From this study interval, two storm events can be therefore recognized:

- From the January 7 at 12:00 h until the January 10 at 3:00 h.
- From the January 14 at 07:00 h until the January 16 at 18:00h.

First storm event (January 7 to January 12, 2010) The first storm event has two fairly distinguishable directions (see Fig. 5.6). Waves started growing on late January 7, approaching the coast from the east. This part of the storm is much more powerful than the second part and suggests the possible occurrence of a typical bi-modal event. Particularly, eastern wave groups are commonly associated with incoming swells generated far away from the coast. Furthermore, substantially longer periods ($T_p > 10\,\mathrm{s}$) are exhibited during this first part of the storm, which clearly indicates the presence of long waves, i.e., swell trains. From the January 9 on, shorter waves approaching the coast from the northwest (and eventually south) prevail. Sánchez-Arcilla et al. (2008) pointed out the occurrence of doubled peak spectra in this region, consisting of pre-existing eastern or southern swells and, eventually, northwest wind waves. It can be seen that wave heights drop during this second phase of the storm at the buoy of Llobregat and wave directions are not parallel to the northwest. This fact emphasizes the spatial gradient which the Catalan coast is subject to.

Therefore, the first storm event is expected to be represented by such a bi-modal spectrum if presence of swell is maintained throughout the length of the storm at Tortosa, whereas only presence of swell is expected at Llobregat, due to the low variability observed in wave periods and directions.

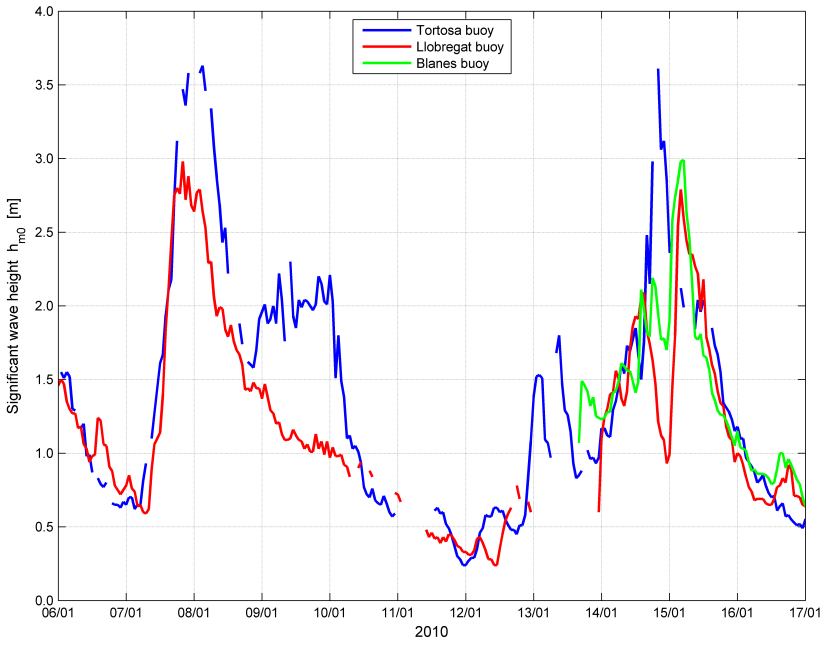

Fig. 5.3 Significant wave heights at the buoys of Tortosa, Llobregat and Blanes during the study interval (January 6 to January 17, 2010).

Second storm event (January 14 to January 16, 2010) The second storm is suspected to be originated by offshore-blowing winds that generated growing wind waves approaching from the north – northwest in fetch-limited conditions at the buoy of Tortosa. Significant wave heights increased substantially on January 15 and reached values above 3.5 m at the southernmost buoy. Although no regular directions held for the course of the storm event, north–northwestern energetic waves may be associated with wind generation in the aforementioned fetch-limited conditions and eastern or southern swells superposed may took place during the beginning and end of the period of consideration (see Fig. 5.6).

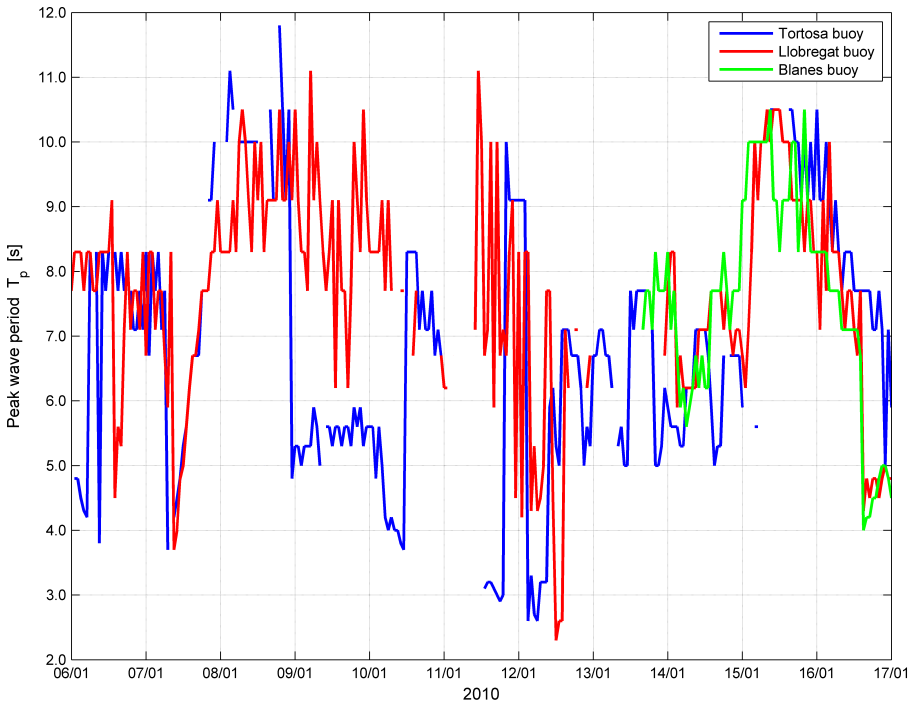

Fig. 5.4 Peak wave periods at the buoys of Tortosa, Llobregat and Blanes during the study interval (January 6 to January 17, 2010).

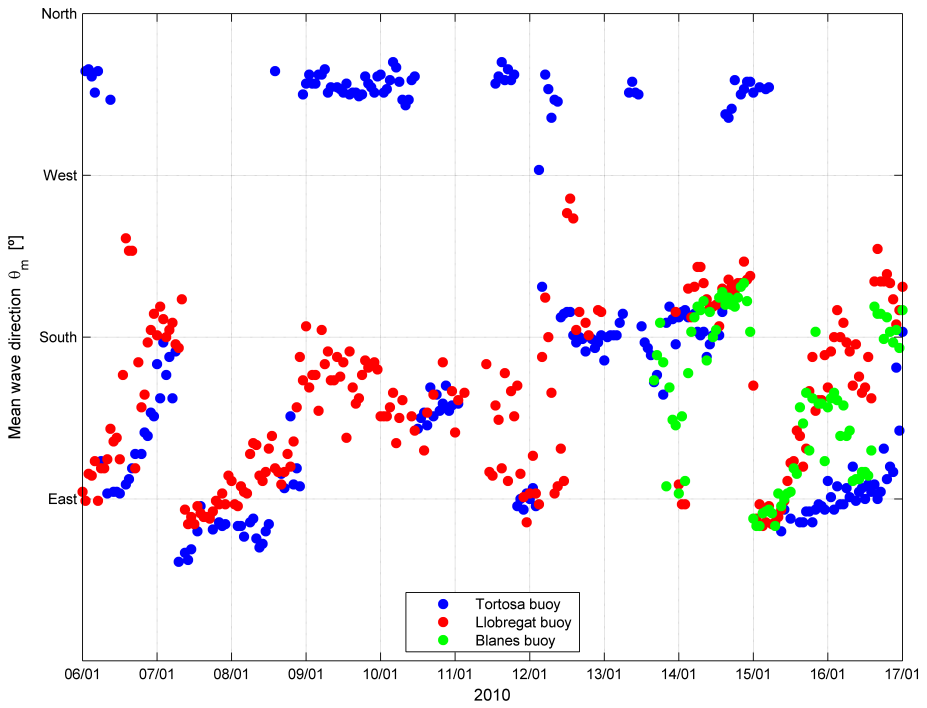

Fig. 5.5 Mean wave directions at the buoys of Tortosa, Llobregat and Blanes during the study interval (January 6 to January 17, 2010).

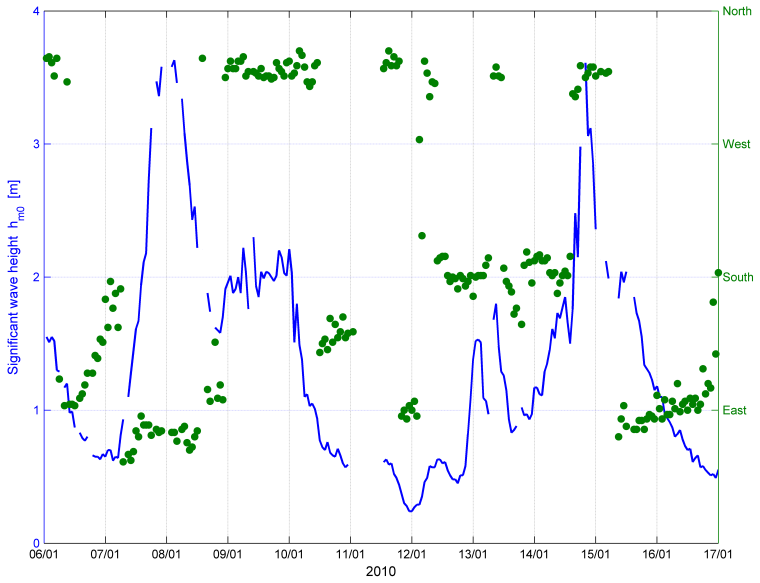

Fig. 5.6 Significant wave height and mean wave direction during the study interval (January 6 to January 17, 2010) at the buoy of Tortosa.

5.3 Validation tools

Even though these parameters are statistically representative when long time series are available (at least two or threes months of simulation), they give a quantitative evaluation of the degree of accuracy of model results. Therefore, the main parameters explored are: the root mean square error (RMSE), bias parameter, scatter index (SI), correlation coefficient (R) and mean absolute error (MAE). These statistical parameters are calculated as follows:

$$\mathrm{RMSE} = \sqrt{\frac{1}{N}\sum_{i=1}^{N}(S_i - O_i)^2} \tag{5.2}$$

$$\mathrm{bias} = \sum_{i=1}^{N}\frac{1}{N}(S_i - O_i) \tag{5.3}$$

$$\mathrm{SI} = \frac{\mathrm{RMSE}}{\frac{1}{N}\sum_{i=1}^{N} O_i} \tag{5.4}$$

$$R = \frac{\sum_{i=1}^{N}\left\{\left(S_i - \bar{S}\right)\left(O_i - \bar{O}\right)\right\}}{\sqrt{\left\{\sum_{i=1}^{N}\left(S_i - \bar{S}\right)^2\right\}\left\{\sum_{i=1}^{N}\left(O_i - \bar{O}\right)^2\right\}}} \tag{5.5}$$

$$\mathrm{MAE} = \frac{\sum_{i=1}^{N}\Delta\theta_{O,S}}{N} \tag{5.6}$$

where O_i is the observed value, $\bar{O}$ is the mean value of the observed data, S_i is the simulated value, $\bar{S}$ is the mean value of the simulated data and N is the number of data. The shortest distance $\Delta\theta_{1,2}$ between two directions is computed as: $\Delta\theta_{1,2} = 180 - |180 - |\theta_1 - \theta_2||$. The four integral parameters used for validation are submitted for statistical analysis in Section 6.3.

Chapter 6

Results and discussion

All in all, as previously introduced, the aim of this report is to find out the reasons why disagreement exists between observed and estimated integral parameters from a physics point of view. Therefore, instead of statistically derive a combination of parameters (dissipation function) that best fits with observations, a comprehensive assessment on the actual impact in both spectral and integral domains shall be performed. In fact, the use of this approach will provide more insight into the relative contribution of spectral dissipation to the overall wave spectrum at this particular location.

In the same way as in Section 5.2, the main wave parameters resulting from the computations shall be compared with buoys' at the various available locations. The selected parameters for the study are: the significant wave height h_{m0}, the peak and mean periods, T_{m02} and T_p, and the mean wave direction θ_m. It is important to recall that these parameters are defined within the spectral domain although can be directly compared with integral parameters obtained from measuring instruments through the formulation provided in Section 2.2. In order to properly understand the evolution of each storm event, as mentioned above, conclusions drawn from visual analysis shall be tightly wedded to the spectral description of waves.

The notation used in this chapter (e.g., see Fig. 6.7) is explained below:

- (WM) and (BS) refer to both the coarse and fine computational domains (Western Mediterranean and Balearic Sea, respectively),
- the combination of two values (e.g., 0.0-0.5) stands for the delta and dissipation coefficient values (δ and C'_{ds}, respectively).

Furthermore, wind and wave directions are provided in accordance with the criteria displayed in Fig. 6.1, where values are assumed to "come from" such a direction.

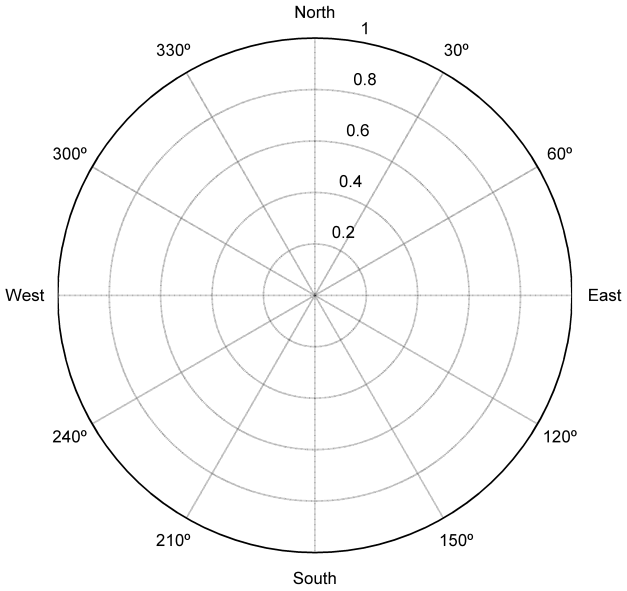

Fig. 6.1 Wind- and wave-directional criteria.

6.1 First storm event (January 7 to January 12, 2010)

The typical synoptic generation of storms at the NW Mediterranean shows the development of a low pressure system established in the Southwestern Mediterranean, producing strong winds from the east and northeast with a fetch of approximately 500 km at the Catalan coast. Wind turns from east to northeast and north (almost always northwest Tortosa due to the funneling through the Ebro river valley).

Therefore, wind coming from the east may correspond to air fluxes from the low pressure center over the sea. It is in this direction where developed wave conditions (associated with swell wave groups) may occur. On the other hand, winds coming from the northwest (at Tortosa) correspond to air flow channeled by the Ebro river valley and blow towards the sea through the opening in the coastal mountain chain. The latter characteristic offshore-blowing winds result in a fetch- and duration-limited growth conditions that commonly produce wind-sea waves at Tortosa.

The storm gains intensity and propagates towards the north, moment at which winds turn in an anti-clockwise fashion. Fig. 6.2 shows the evolution of the wind field for the previous hours to the beginning of high-intensity phase of the storm (hereafter referred as the peak of the storm, on January 8, at 00:00 h). It can be clearly seen the abovementioned wind-direction turn and a certain degree of correlation between growing wind velocities and wave heights (Fig. 6.3). This shall serve as a basis for the reasoning behind the very first impact of the storm at the regional scale of analysis.

First, wave groups generated outside the Balearic Sea reach the coast. These wave groups are associated with longer fetches from the east-northeast and their effect is by far the largest at the coast, within the storm event. A second part of the storm is clearly visible due to the fact that wave height appears to significantly differ among the different buoy stations. This effect is assessed later in this chapter, but it can be foreseen that the wind spatial gradient over the coast, and the corresponding wind-wave growth, determine such differences. Fig. 6.4 displays the temporal evolution of the significant wave height, both observed and simulated.

There is an important spatial gradient in terms of integral wave parameters at the Catalan coast, specially determined by the effect of littoral orography on the spatial evolution of wind patterns. This fact, which is explained next, brings added value to the selection of this storm, which agrees with the typical bi-modal events in the region: a northwestern wind blowing over a pre-existing eastern swell. Wind-wave growth conditions, however, are only expected at the buoy of Tortosa due to the wind channeling through the Ebro river valley.

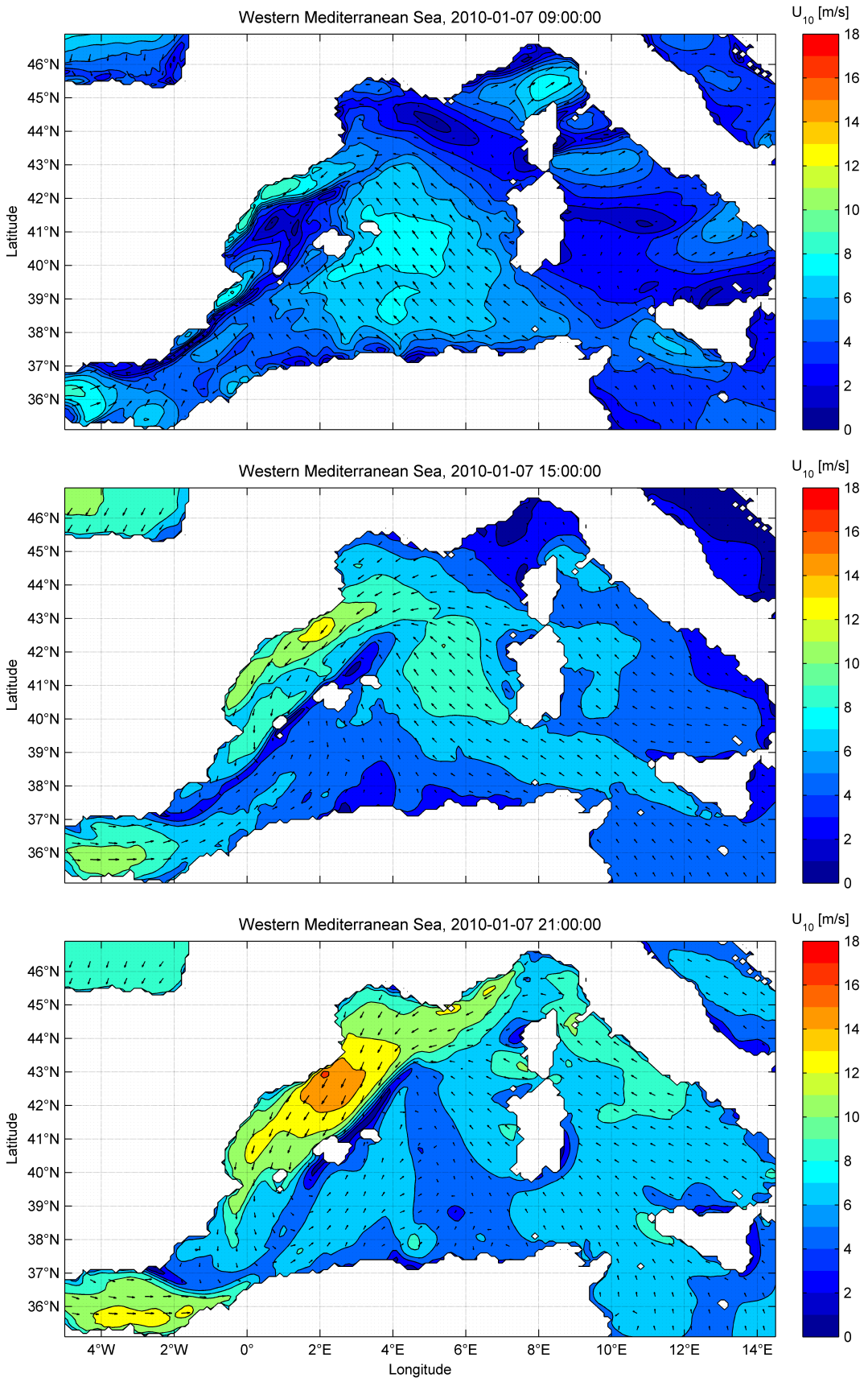

Fig. 6.2 Wind field evolution on late January 7, 2010. Arrows indicate the mean wind direction. Western Mediterranean Sea (WM) grid.

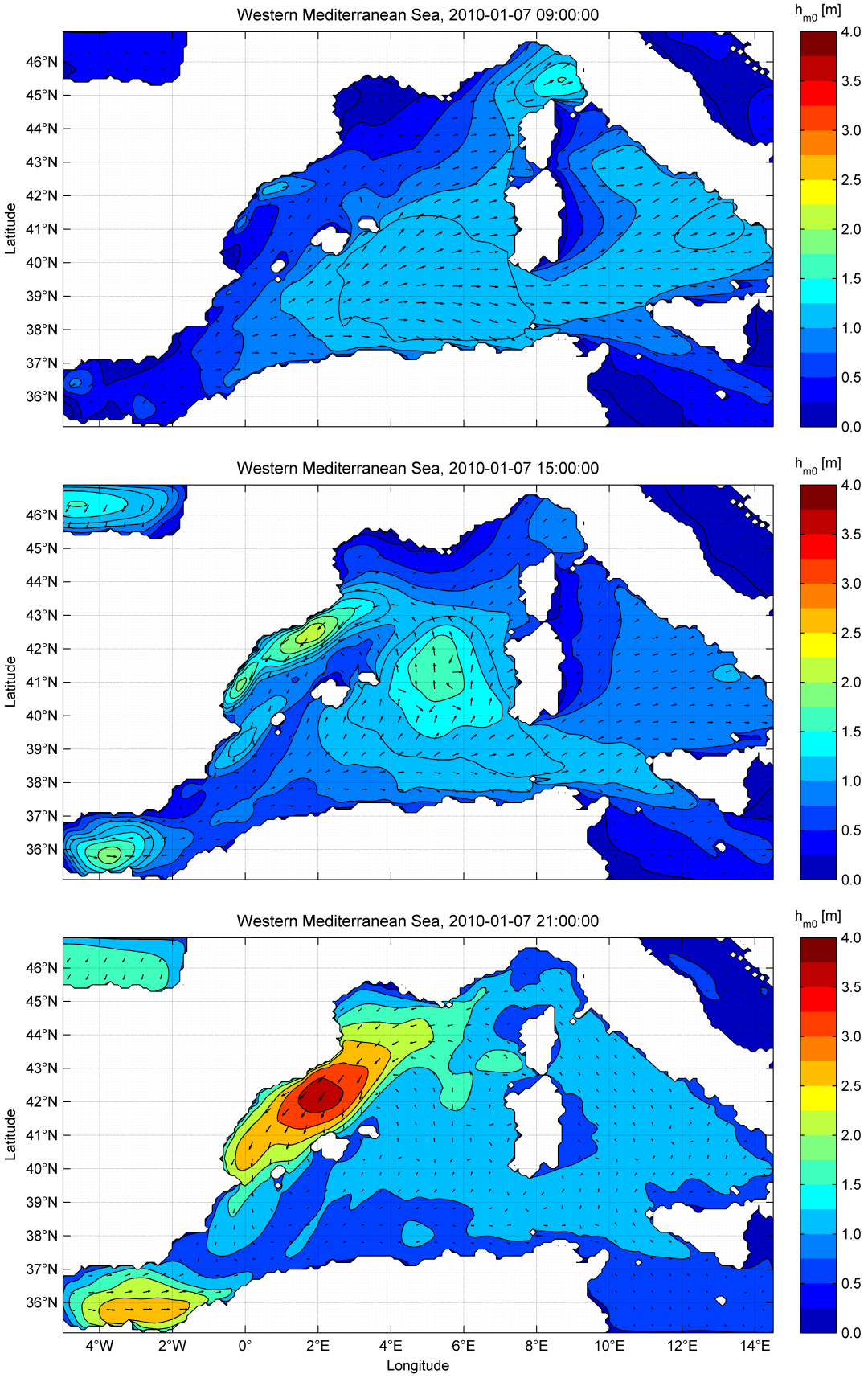

Fig. 6.3 Mean wave height evolution on late January 7, 2010. Arrows indicate the mean wave direction. Western Mediterranean Sea (WM) grid.

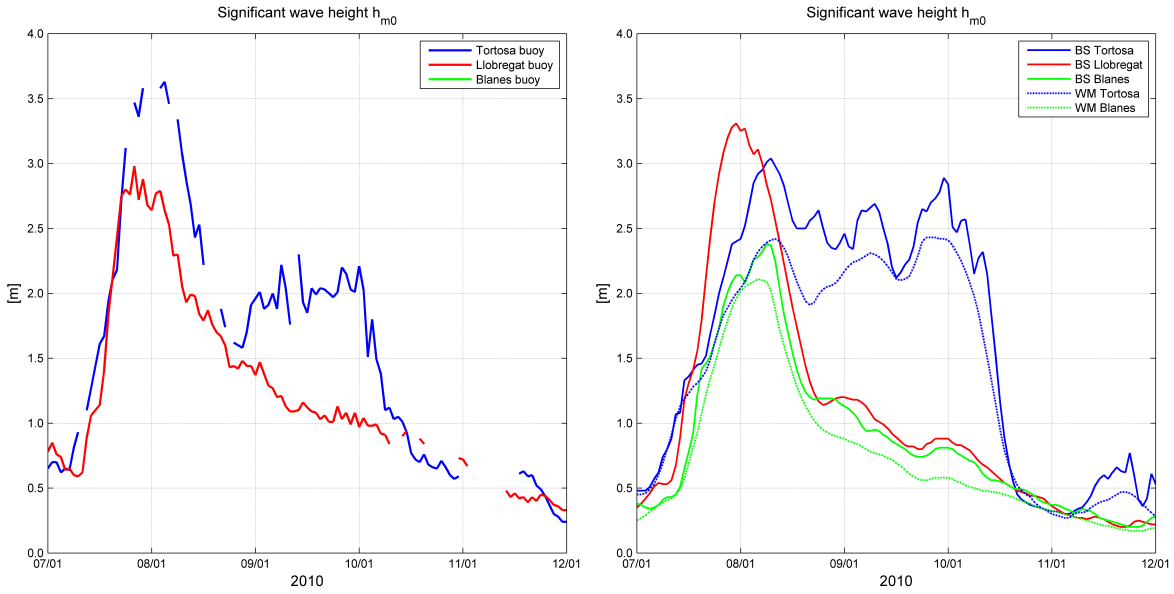

(a) Observed significant wave heights

(b) Computed significant wave heights

Fig. 6.4 Temporal variation of (a) observed wave heights and (b) estimated wave heights at the three different locations during the first storm event. Note that no observed measurements from the buoy of Blanes are available during this storm.

The latter can be clearly deduced from the temporal evolution of the wind speed (Fig. 6.5). At the buoy of Tortosa, wind velocity gradually grows until a few hours before the end of the storm (January 10, at 12:00 h), whereas at higher latitudes, Llobregat and Blanes, wind speed rapidly drops shortly after the peak of the storm (January 8, at 00:00 h). Additionally, during the second part of the storm, wind clearly tends to turn towards the northwest, most evidently at the buoy of Tortosa. Therefore, the northeastern wind that initially enhances the incoming eastern swell turns in an anti-clockwise direction, promoting the generation of wind-sea waves parallel to the northwestern offshore-blowing wind. The latter wave groups are responsible for the relatively high wave heights present at Tortosa after the peak of the storm, whereas due to the weak influence of wind, wave heights are considerably lower at the remaining locations.

The existence of significant input of energy by wind, when swell waves are also present, leads to the frequently, and virtually exclusive, occurrence of bi-modal wave spectrum near the Ebro delta. Even though it has been reported that winds exhibit high variability (both temporal and spatial), the fact that it is effectively channeled by the Ebro river valley leads to a steady, in directional terms, and gradually faster air-flow directed towards the coast near the delta. Consequently, though in fetch-limited conditions, waves are capable of being

developed due to wind-energy input.

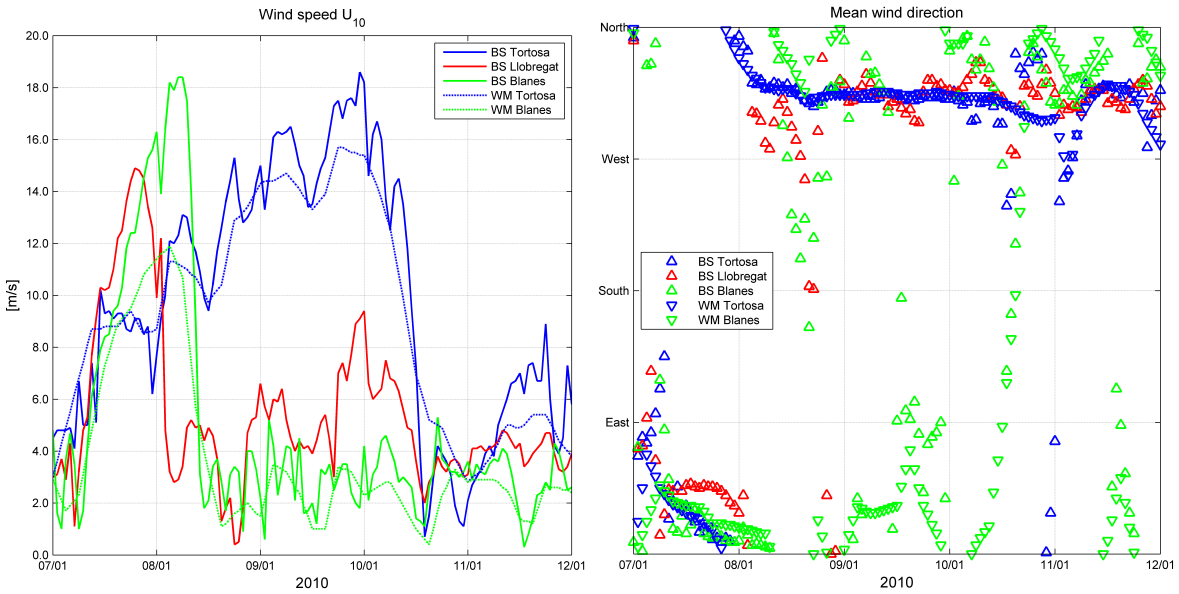

(a) Computed wind speeds

(b) Computed mean wind directions

Fig. 6.5 Temporal variation of estimated (a) wind velocities and (b) mean wind directions at the three different locations during the first storm event.

As a final note, with reference to the wind field, it is important to understand the main drawback that hinders the proper simulation of reliable wind velocities coming from the land. Simulation models assume that wind velocities are zero at land grid points and, thereafter, grid cells that contain both land and sea grid points will be dramatically influenced by the sharp gradient in wind velocities (between neighboring grid points during the bilinear interpolation performed). This effect is subject of discussion and many authors have reported the non-negligible interference from land presence when validation with instrumentation near the coast (de León and Orfila, 2013). All in all, even though not assessed in this research, it must be borne in mind that offshore-blowing wind, especially present at Tortosa buoy, is likely to be influenced by the nearby coast.

In the following, attention is drawn to the buoy of Tortosa and most part of the analysis is based on conclusions extracted at that location. As introduced in this chapter, a reasoning founded on physics of integral parameters shall be driven through spectral analysis and, thus, reference is first given to the evolution of the spectral energy density.

Spectral analysis On the January 7, the high-frequency energy grows and slowly migrates to lower frequencies. During this growth phase, the wind direction gradually turns first to the north and eventually to the northwest. This direction is associated to the offshore-blowing winds commented above. Wind velocities continue growing although the energy spectrum is overpowered by the low-frequency energy of the incoming swell.

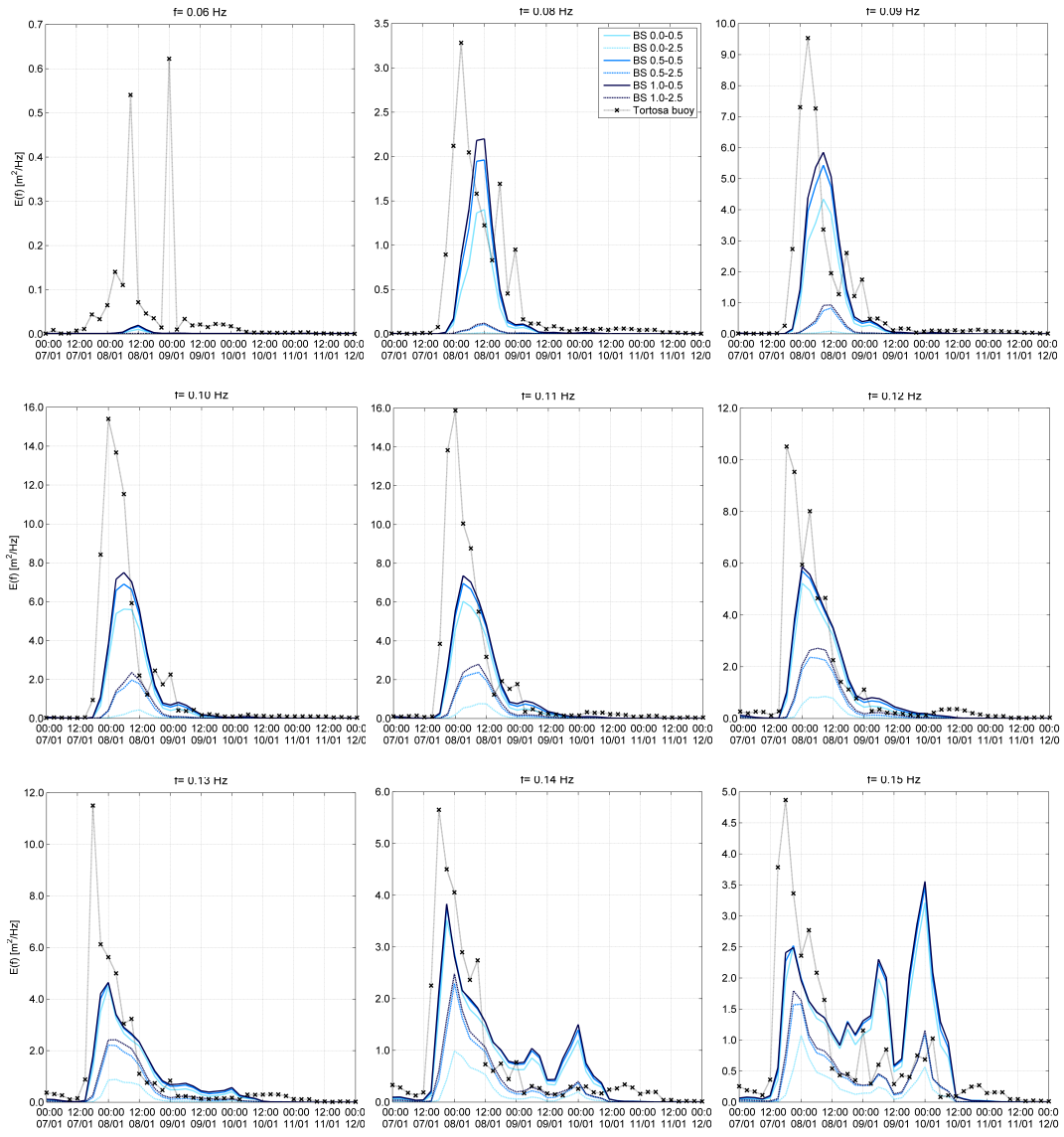

Fig. 6.6 Time series of frequency spectra at Tortosa buoy (low-frequency range) during the first storm event. Buoy data are compared with WAM data with different combinations of whitecapping coefficients. Note that scaling of ordinate axis is not constant, so the comparison is essentially normalized.

The energy level rapidly grows and the peak frequency eventually reaches 0.11 Hz. It is during this time where it can be concluded that low-frequency energy is notably underestimated, regardless of the combination of parameters (see Fig. 6.6, specially 0.10 and 0.11 Hz). Therefore, the reason of the clear underprediction of some of the integral parameters (e.g., significant wave height) is mainly due to the substantially low amount of energy at that range of frequencies. It should be stated that using a small dissipation coefficient dramatically yields much more energy, thus reducing the insurmountable difference at low-frequencies and, additionally, the delta value even enhances the energy level when equal to 1. This effect can be clearly observed in both Fig. 6.6 and Fig. 6.8.

Alternatively, it is likely that insufficient energy input at low frequencies causes this large underprediction. If so, it should be assessed whether the wave conditions at the boundaries of the computational grid may affect the estimations at the Catalan coast. Since the fine grid (BS) is nested within the coarse grid domain (WM), integral parameters from both grids have been compared at the neighboring grid points of the eastern boundary of the subgrid in order to report possible errors. Additionally, it has been analyzed whether the generation of a wave forcing at the southern boundary of the coarse grid (WM), between the longitudes 10°E and 12°E, may have influence at the study area. However, none of the above assumptions has led to changes in the estimations at the three buoy stations. This admits of the conclusion that larger amount of energy derived from observations existed during the swell arrival, whereas the wave model yielded a lower amount.

After the peak of the storm (January 8, at 00:00 h), swell energy is gradually dissipated and there is no apparent, subsequent growth of high-frequency energy (at the buoy), whereas computed energy is quickly pumped up to high frequencies. Therefore, the total amount of energy coming from both buoy and wave model are approximately the same, at that time, and hence wave heights are seemingly similar.

A few hours later, energy is transferred to high frequencies due to the growing wind-energy input. Spectral distribution of wave energy is rather stable during the wind-wave growth phase although the amount of energy is highly variable between consecutive wave records (at the buoy). The fact that a JONSWAP spectrum shape is recognizable on simulated spectra satisfies the reasoning followed, concluding that most of the present energy is supplied by wind. This is also true for observed spectra, although it can be seen that wind variability leads to a multi-peaked spectrum (with a dominant high-frequency peak associated to the most frequent direction in which the wind blows), steering away from the smooth JONSWAP spectrum computed by the model, and therefore denoting the lack of temporal resolution in the simulations (see Fig. 6.7). It was explained that the fact that the Mediter-

ranean Sea can be understood as a semi-enclosed basin with rather short-fetches influencing the Catalan coast discards the observation of spectra developed in more ideal conditions, such as those upon which the JONSWAP spectrum was defined.

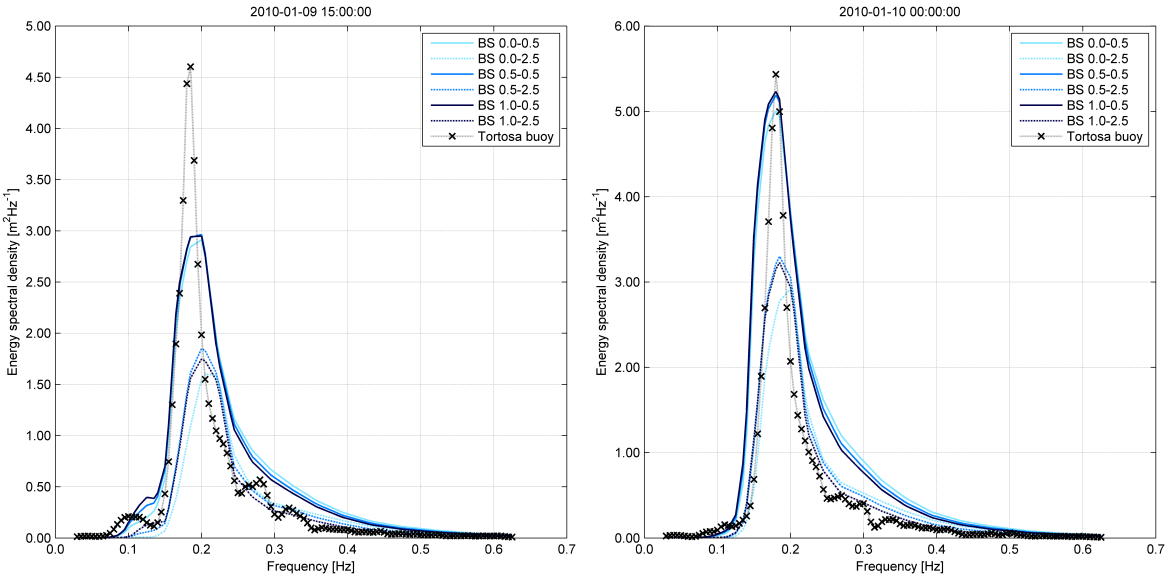

Fig. 6.7 Wave spectra computed at Tortosa buoy, using proposed combinations.

During this time, it can be seen that dissipation free coefficients largely influence the energy level of the spectral peak. This outcome was expected since whitecapping model implemented is almost the mirror-image of the feedback mechanism for wind-induced growth (majorly affecting wind-waves), and hence it actively influences the high-frequency energy. Furthermore, the parametric tail implemented by the WAM model seems to overestimate energy at high-frequencies, i.e., above the peak frequency when uni-modal spectrum (see both Fig. 6.7 and Fig. 6.8). This, unfortunately, is enhanced when the dissipation coefficient is low ($C'_{ds} = 0.5$) and, within the limitations, can be slightly corrected by a high value of delta ($\delta = 1$).

Ultimately, when the wind speed ceases, rather weak, but nonetheless existent, eastern swell waves (which reached the coast during the whole storm) are depicted in the observed spectrum. Similarly to previous analyses, low-frequency waves are not correspondingly well estimated.

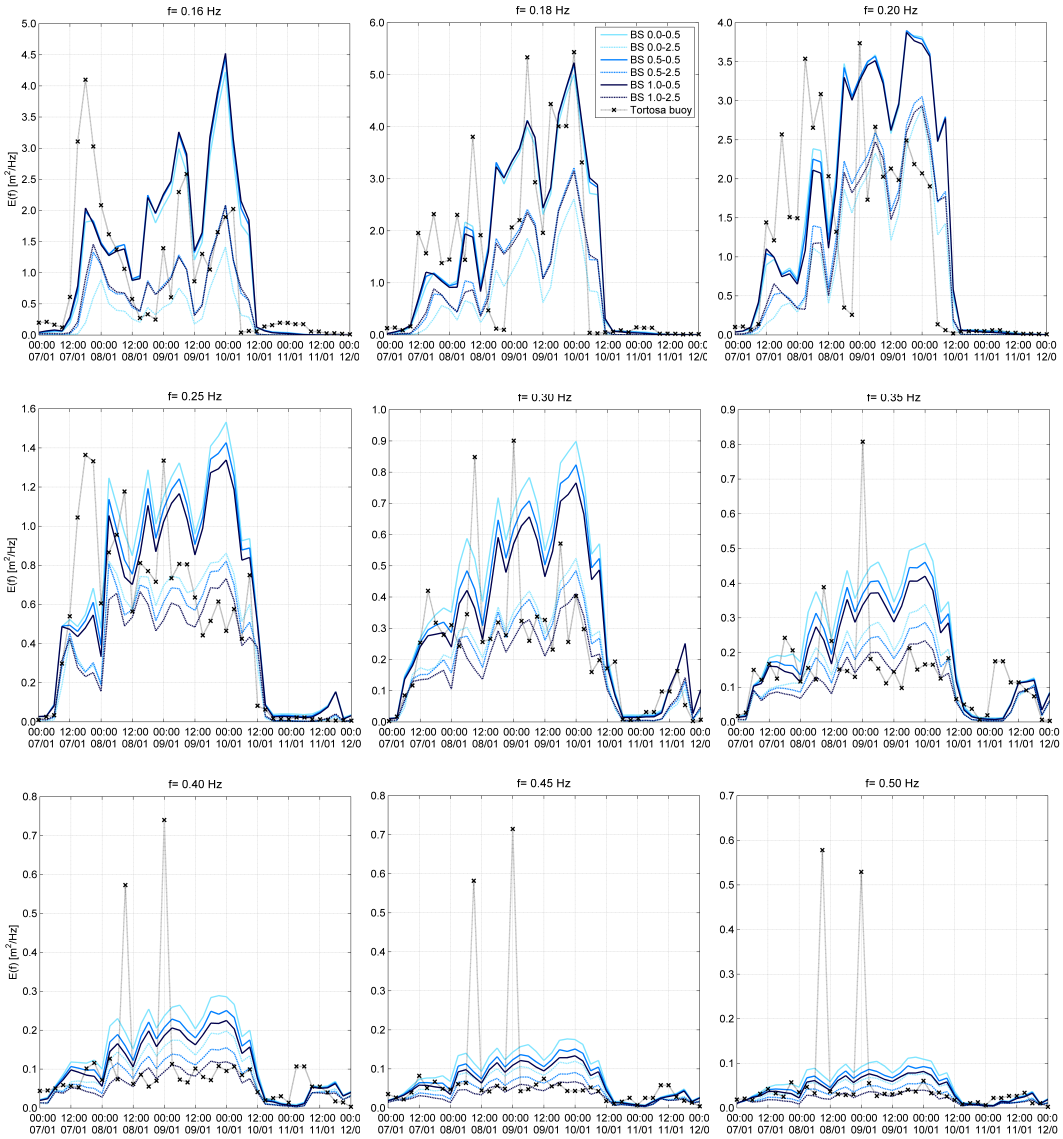

Fig. 6.8 Time series of frequency spectra at Tortosa buoy (high-frequency range) during the first storm event. Buoy data are compared with WAM data with different combinations of whitecapping coefficients. Note that scaling of ordinate axis is not constant, so the comparison is essentially normalized.

Thus, anomalies detected in the evolution of the wave energy explain the disagreement found between observed and computed integral parameters during this first storm event.

Integral analysis First, an overview of the significant wave height validation is provided. It is evident that a clear underprediction of wave height occurs during the peak of the storm due to the large underestimation of low-frequency energy mentioned above. The second part of the storm, associated with the wind-wave growth phase, displays better agreement

for the high-dissipation combination ($C'_{ds} = 2.5$), whereas low dissipation ($C'_{ds} = 0.5$) yields too large wave heights.

The large and general underprediction of low-frequency can be attributed to the fact that the presence of wind-sea causes swell (approximately 0.05-0.12 Hz) to dissipate. This occurs because of the dependence of the whitecapping sink term on integrated wave steepness. This effect is illogical and is not observed in the buoy data. On the other hand, the overestimation visible during the second phase of the storm might be due to underdissipation (i.e., whitecapping coefficients, for low-dissipation, lead to an excess of wave energy when the uni-modal spectrum is dominated by wind-sea). Another solution suggests that the wind field might be overestimated, thus inputting too much energy. The latter conclusion cannot be validated due to the absence of measured data with regard to wind fields.

All in all, it can be concluded that largest influence in significant wave height lies on the dissipation coefficient, C'_{ds} (see Fig. 6.9), rather than the delta value.

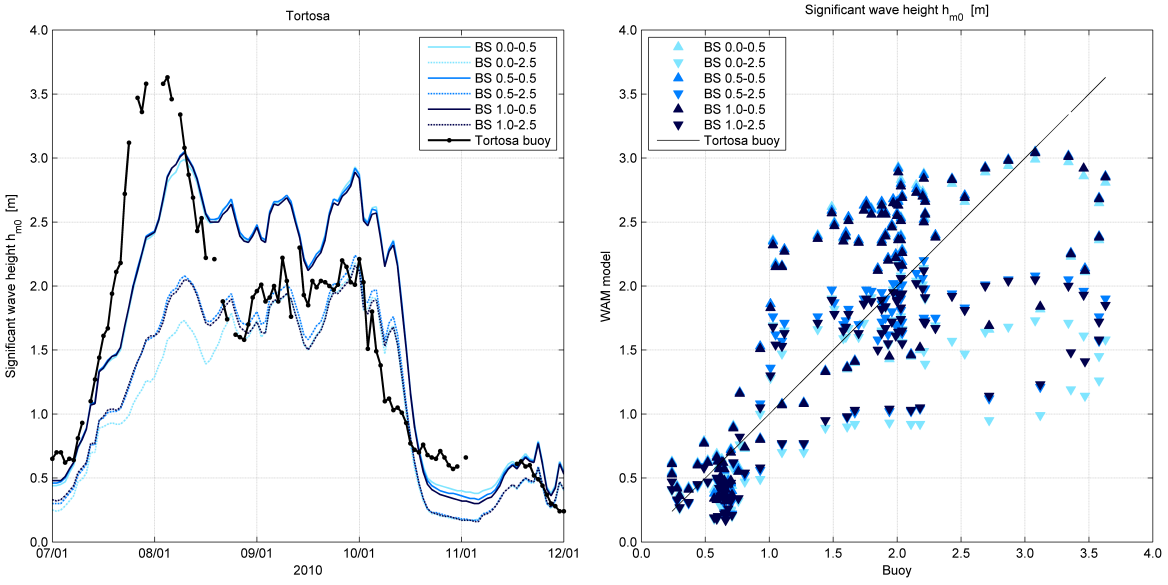

(a) (b)

Fig. 6.9 (a) Comparison of temporal evolution of the significant wave height for different whitecapping coefficients and (b) the corresponding scatter plot at the buoy of Tortosa during the first storm.

Peak wave period shows relative underestimation during the peak of the storm (swell dominance), although better agreement is found during the second part, when swell energy is dissipated and the maximum peak is located at higher frequencies, associated with the northwestern wind-sea (see Fig. 6.10). One can argue that the magnitude of the parameter in question depends on the peak frequency (i.e., the location of the spectral peak on the frequency axis), and thus an underprediction of the peak period should correspond to a larger peak frequency. Alternatively, it can be related to inaccuracies in the computation of the quadruplet wave-wave interactions in the sense that not enough energy is transported to lower frequencies (process known as "downshifting") over the whole evolution of the wave spectrum during the swell-energy growth phase.

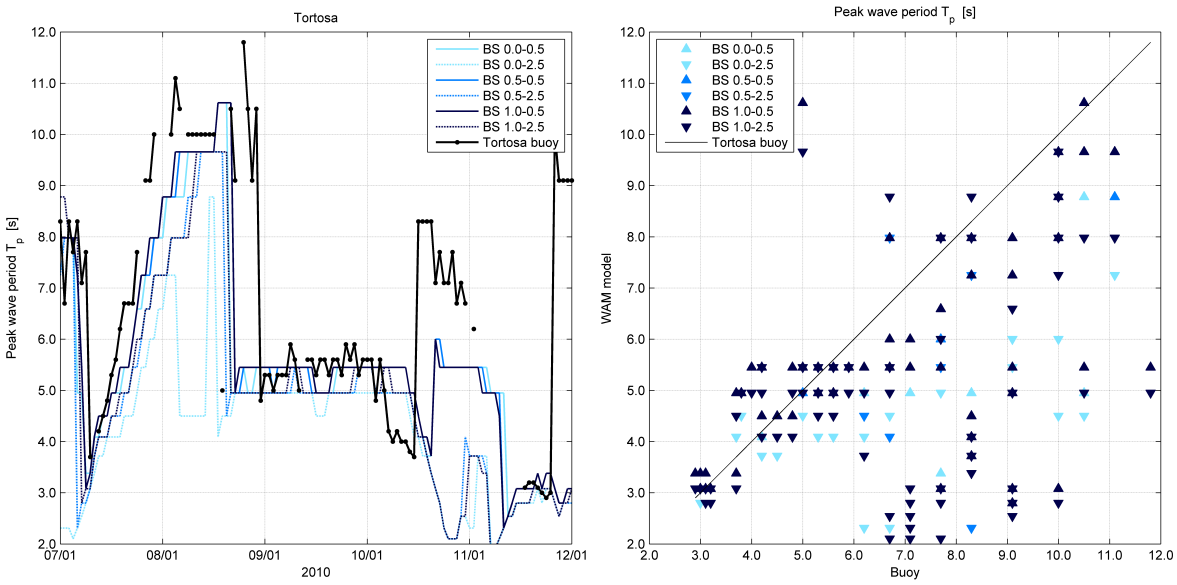

(a) (b)

Fig. 6.10 (a) Comparison of temporal evolution of the peak wave period for different whitecapping coefficients and (b) the corresponding scatter plot at the buoy of Tortosa during the first storm.

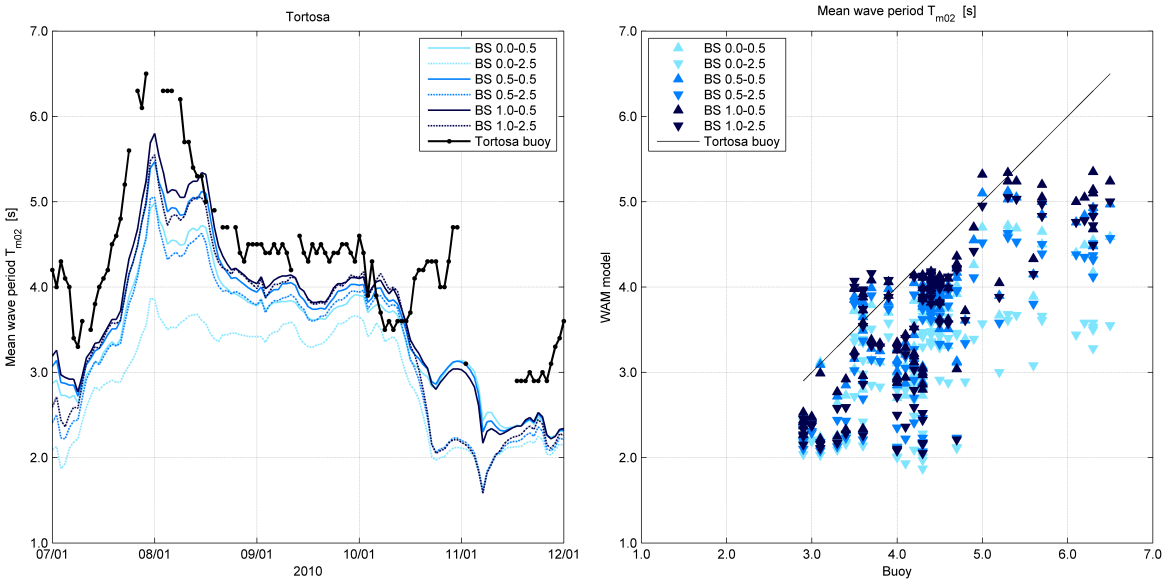

(a) (b)

Fig. 6.11 (a) Comparison of temporal evolution of the mean wave period for different whitecapping coefficients and (b) the corresponding scatter plot at the buoy of Tortosa during the first storm.

On the other hand, mean wave period T_{m02} is underestimated throughout the length of the storm (Fig. 6.11). It has been concluded that this is the result of an overprediction of high-frequency energy in the wave spectrum. It has been previously reported that spectral energy at that frequency range is significantly larger likely due to low dissipation of wind-sea when presence of swell or, alternatively, a poor fit of the parametric tail implemented by WAM, yielding too much energy at high frequencies (see Figs. 6.7 and 6.8).

The physical description of the mean wave period T_{m02} is very sensitive to the amount of high-frequency energy due to the dependence on the second-order spectral moment m_{02}, which in turn is largely influenced by the square of the frequency (see Eq.(2.8)). Therefore, the second-order spectral moment dramatically gives more weight to energy at high frequencies. Consequently, overestimation of m_{02} leads to an underestimate of the mean wave period T_{m02}.

As a final remark, mean wave period can be substantially modulated and, most importantly, corrected by using a low dissipation coefficient and a large delta value (see large scatter in Fig. 6.11b).

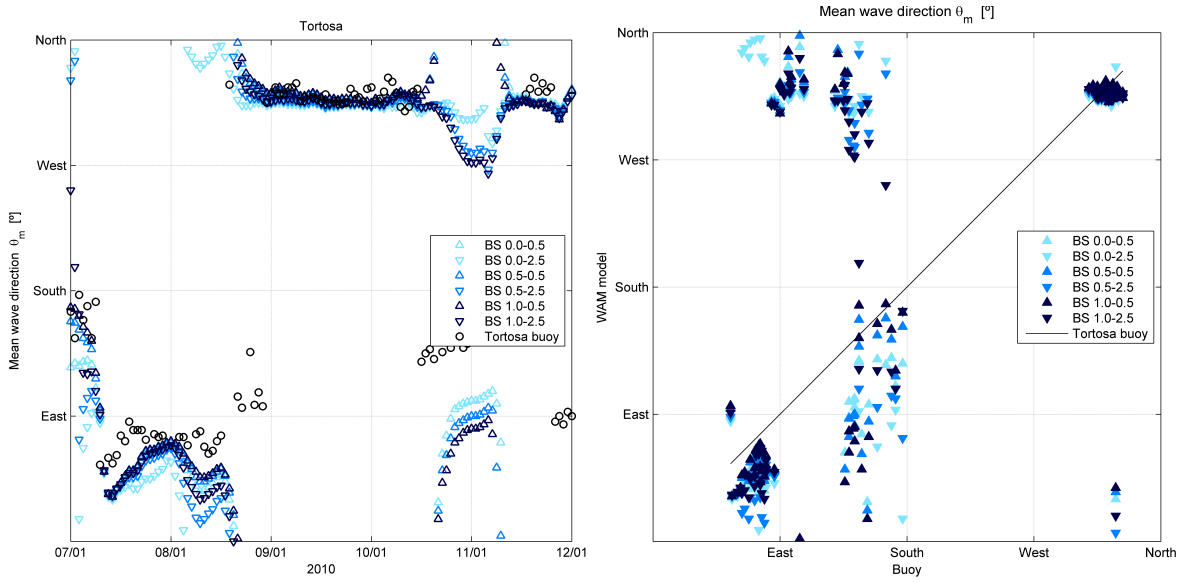

(a) (b)

Fig. 6.12 (a) Comparison of temporal evolution of the mean wave direction for different whitecapping coefficients and (b) the corresponding scatter plot at the buoy of Tortosa during the first storm.

Ultimately, mean wave directions are well reproduced by the model. Note that, however, at some point, mean wave directions turn to the southeast during both the second halves of January 8 and January 10 (see Fig. 6.12) and model's estimates do not correspond with a similar change. These two sudden changes (towards the southeast) occur when there is a marked drop in some of the other integral parameters (significant wave height and mean and peak periods).

The first observed disagreement occurs on January 8, at 15:00 h, moment at which there is a flow of energy from low to higher frequencies in the spectrum (and there is also a transition between underestimation of wave height to overestimation). Seemingly, energy spectrum, although bi-modal, shows earlier enhancement of the wind-sea peak on the estimates, whereas the observed spectrum takes more time. An underestimation of low-frequency energy (swell) and the possibility of an overprediction of the wind field by part of the wind model might have hindered the presence of a southeastern low-frequency wave train.

Second mismatch in wave directions occurs when wind velocities dramatically drop and the eastern swell train reaches the buoy of Tortosa. This low-frequency energy is not captured by the model when dissipation is large ($C'_{ds} = 2.5$). However, even though it is still underestimated, the three combinations with small C'_{ds} value enhance the amount of energy at low frequencies (see Fig. 6.13) and, therefore, better adjustment is found for these

combinations when it comes to mean wave directions. Therefore, the large scatter found between east and south directions (Fig. 6.12b) is due to overdissipation at low-frequencies.

Computations regarding the mean wave direction at the peak of the wave spectrum are strongly dependent on the amount of energy associated to the actual peak and, therefore, situations in which there is little energy lead to large uncertainty. For instance, when observed wave direction come from the southeast on January 10, at 12:00 h (see Fig. 6.12a), significant wave heights have dropped below 0.7 m at the buoy (see Fig. 6.9a) and, therefore, estimates from these directions should be disregarded as they are not representative.

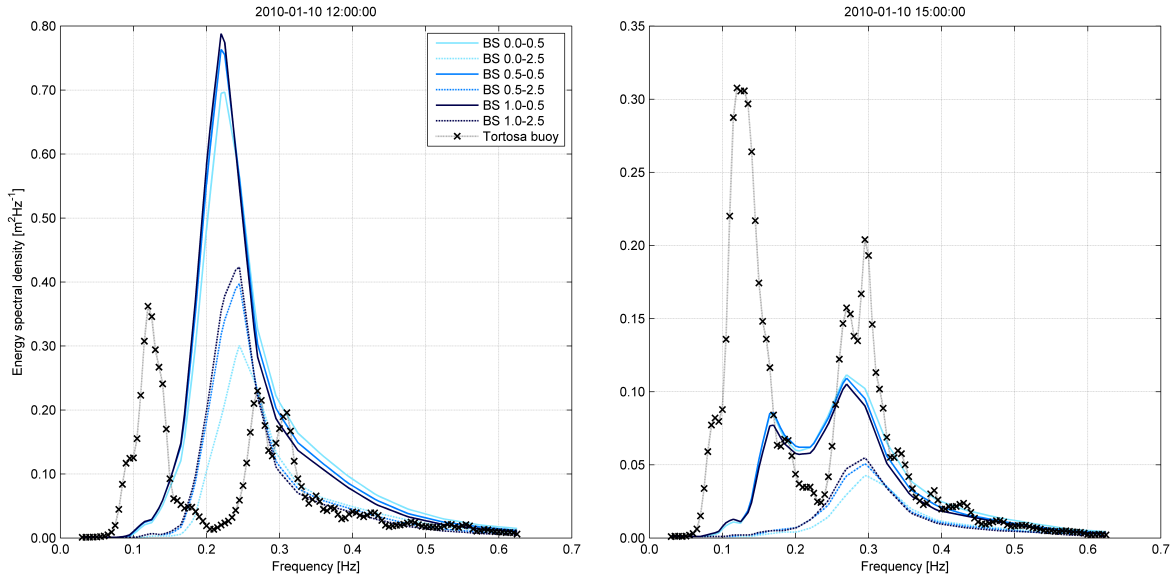

Fig. 6.13 Wave spectra computed at Tortosa buoy, using proposed combinations.

6.2 Second storm event (January 14 to January 16, 2010)

The distinctive feature of the present storm event is the occurrence of a strong coastal wind jet off the coast at the Ebro delta (Fig. 6.14). Even though presence of swell trains is reported during the beginning and end of such a storm, the most intense moments are driven by the high wind-energy input by part of the offshore-blowing wind associated with the coastal wind jet. In short, the main difference between the second and the first storm is the sudden growth in wind speeds at Tortosa (see Fig. 6.5a and Fig. 6.15a).

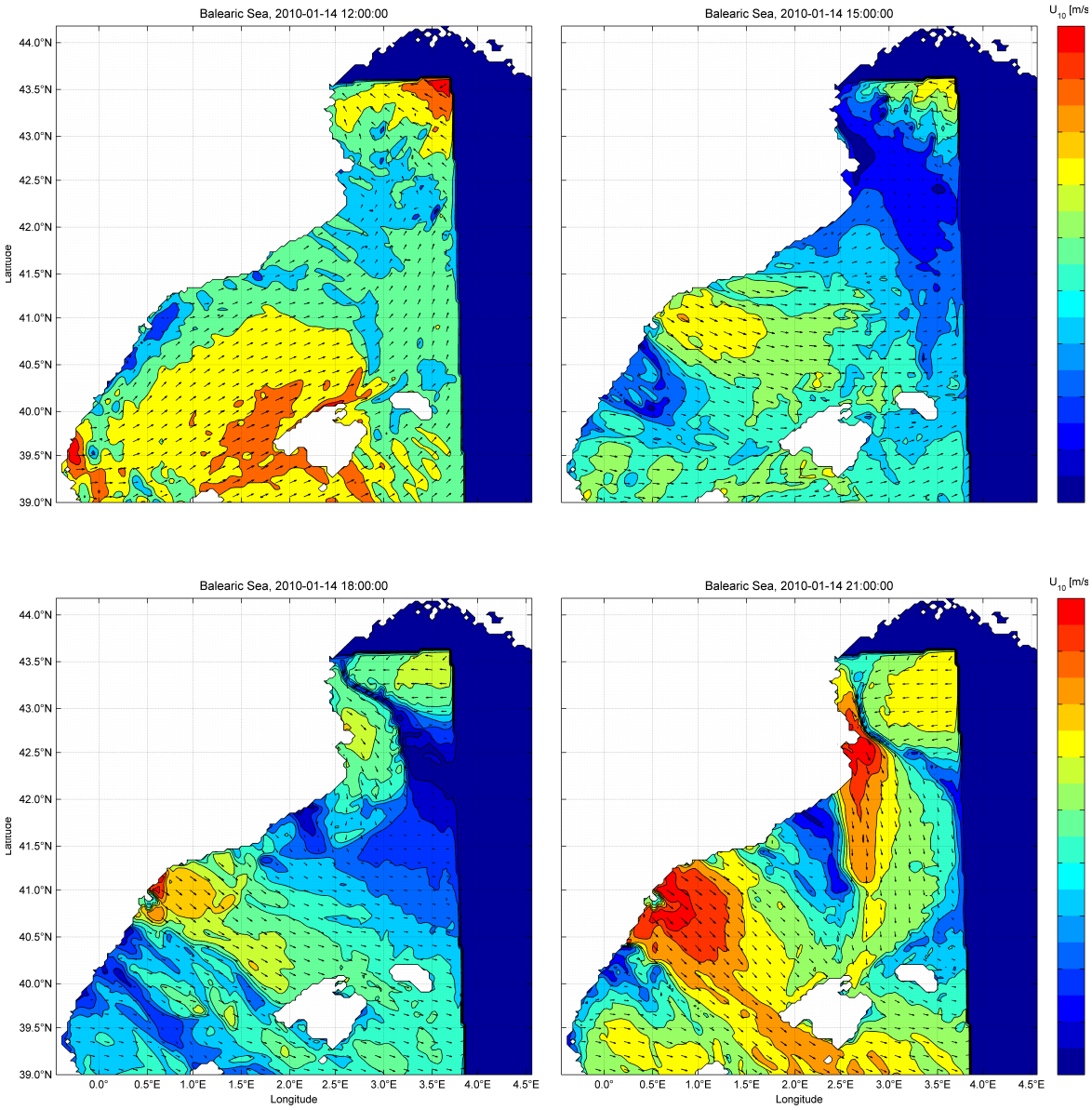

Fig. 6.14 Temporal evolution of the coastal wind jet at the Ebro delta on the January 14, 2010. These results are generated by the WAM model. Arrows indicate the mean wind direction.

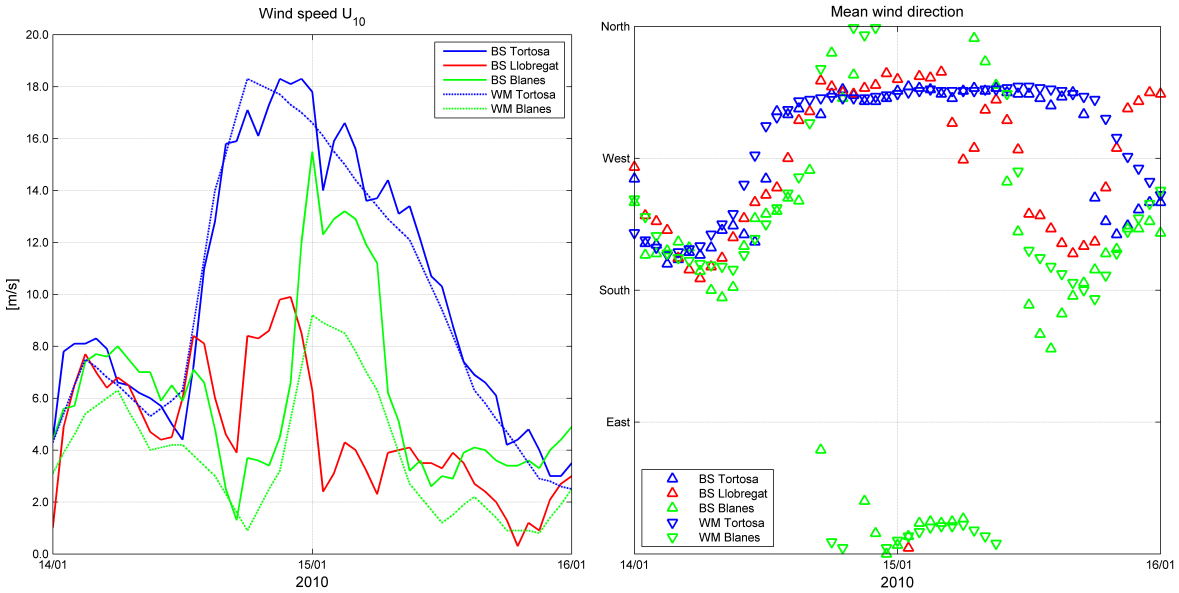

(a) Computed wind speeds

(b) Computed mean wind directions

Fig. 6.15 Temporal variation of estimated (a) wind velocities and (b) mean wind directions at the three different locations during the second second event.

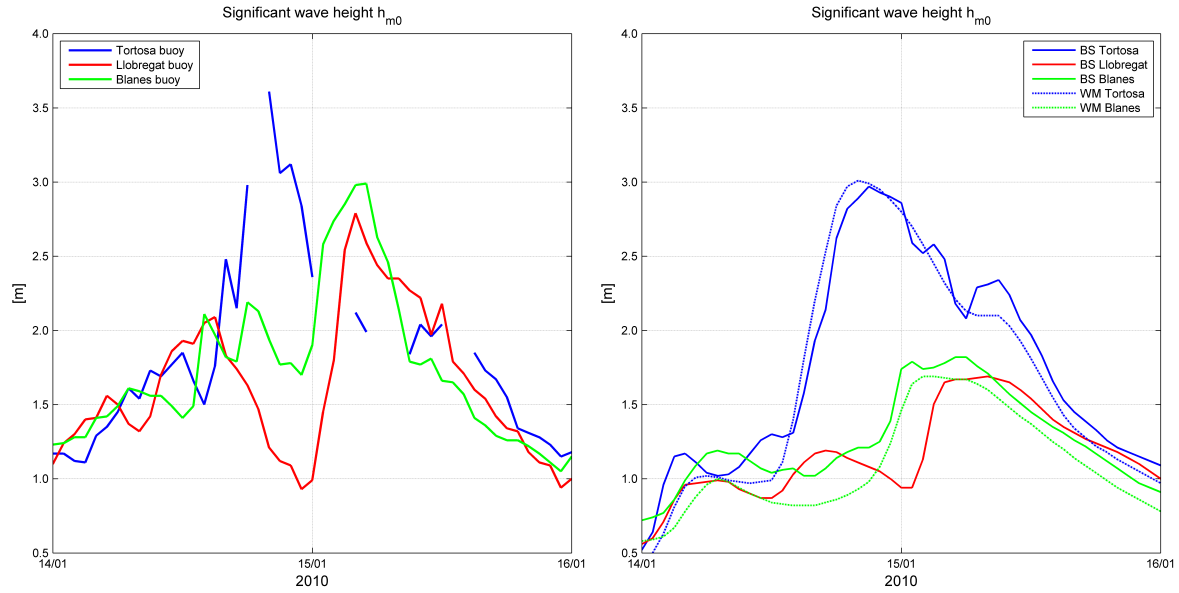

(a) Observed significant wave heights

(b) Computed significant wave heights

Fig. 6.16 Temporal variation of (a) observed wave heights and (b) estimated wave heights at the three different locations during the second storm event.

Spectral analysis The second storm starts with a swell train from the south, although local wind is also blowing from the same direction, which means that local wind is inputting energy at high frequencies. Consequently, two or more energy peaks from the same direction appear at higher frequencies (Fig. 6.19). Estimated spectra present marked underprediction of wave energy, especially during the enhancement of the low-frequency peak recorded by the buoy of Tortosa. The secondary (and narrower) peaks were observed to merge from time to time with each other (or with the main peak), leading to a broad energy spectra along the frequency domain. This multi-peaked pattern is not well captured by the model, which displays a rather smooth peak.

Swell energy is gradually dissipated on January 14, between 12:00 and 15:00 h, point at which wind speed dramatically grows and blows offshore-directed from the northwest (associated with the wind channeling along the Ebro river valley).

During the rest of the January 14, 2010, and until the end of the actual storm (January 15, at 12:00 h), fairly unimodal wave spectra are primarily ruled by the northwestern wind-sea. The peak frequency, which is relatively steady during this phase, is equal to 0.15 Hz, and the maximum energy level occurs just before the January 15, at 00:00 h, when wind velocities attain their maximum speed. At that moment, wind speed gradually diminishes and the amount of energy associated with the wind-sea group similarly decreases, until an eastern swell train propagates towards the coast around January 15, at 12:00 h (see Fig. 6.15).

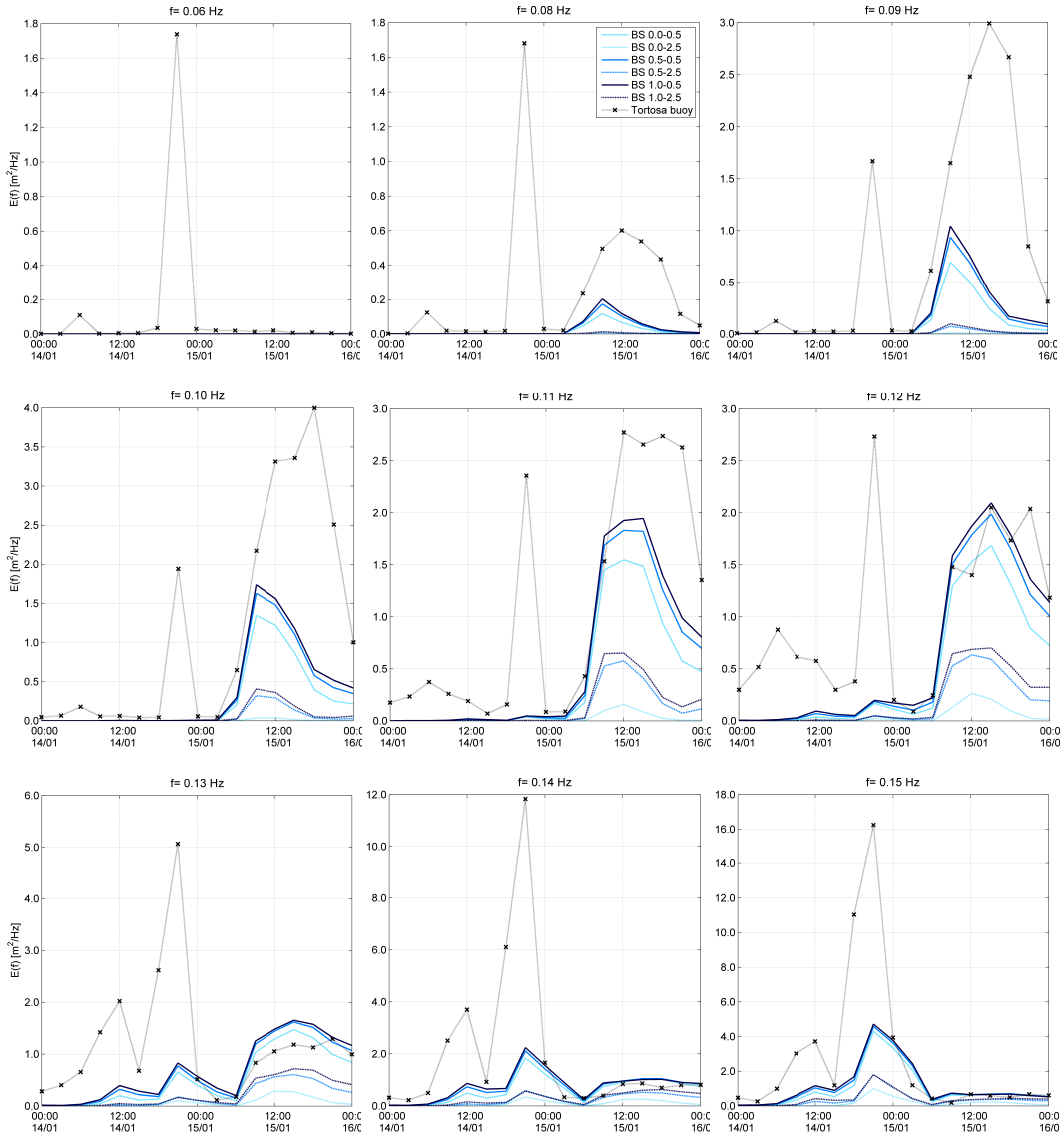

Fig. 6.17 Time series of frequency spectra at Tortosa buoy (low-frequency range) during the second storm event. Buoy data are compared with WAM data with different combinations of whitecapping coefficients. Note that scaling of ordinate axis is not constant, so the comparison is essentially normalized.

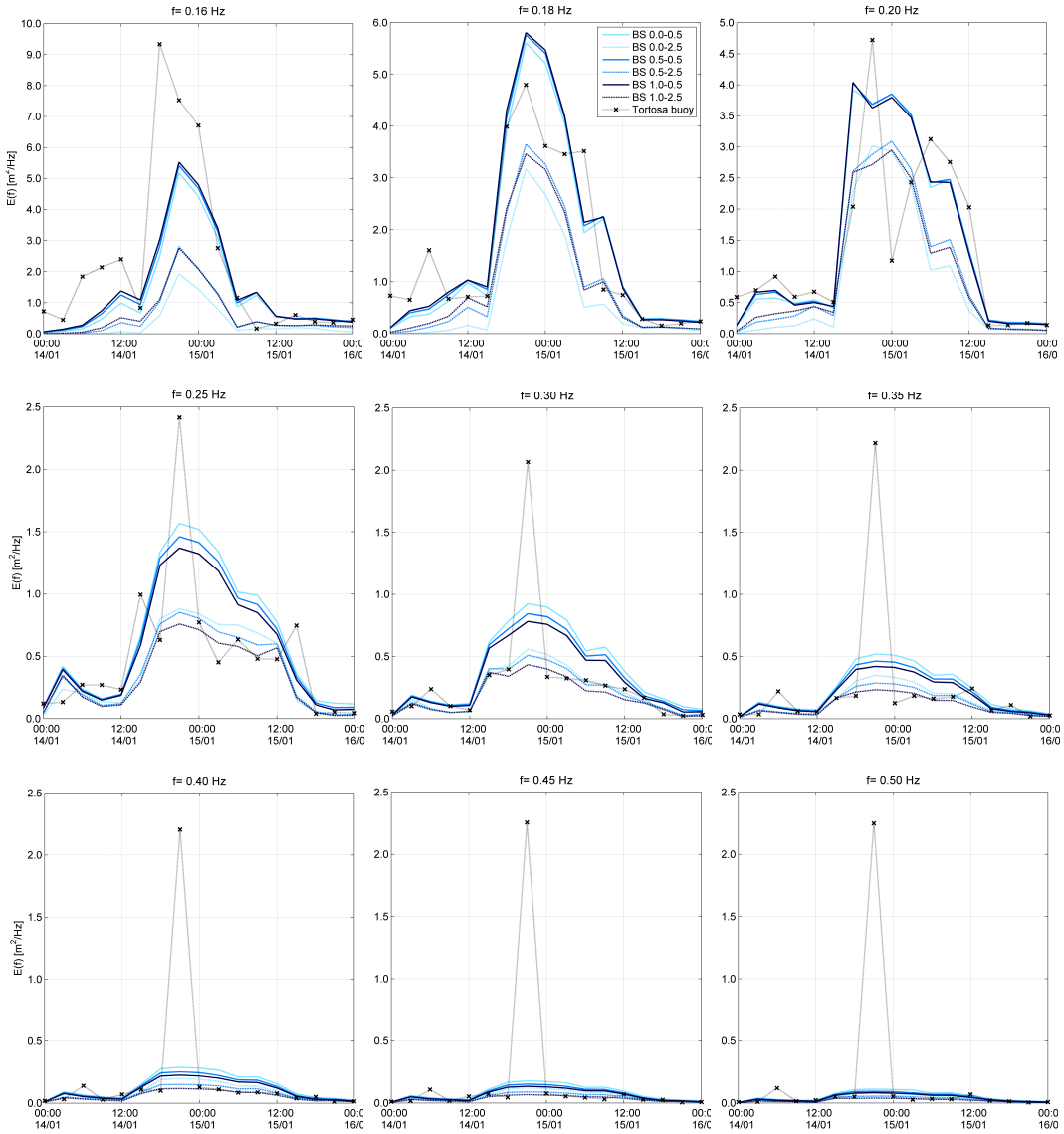

Fig. 6.18 Time series of frequency spectra at Tortosa buoy (high-frequency range) during the second storm event. Buoy data are compared with WAM data with different combinations of whitecapping coefficients. Note that scaling of ordinate axis is not constant, so the comparison is essentially normalized.

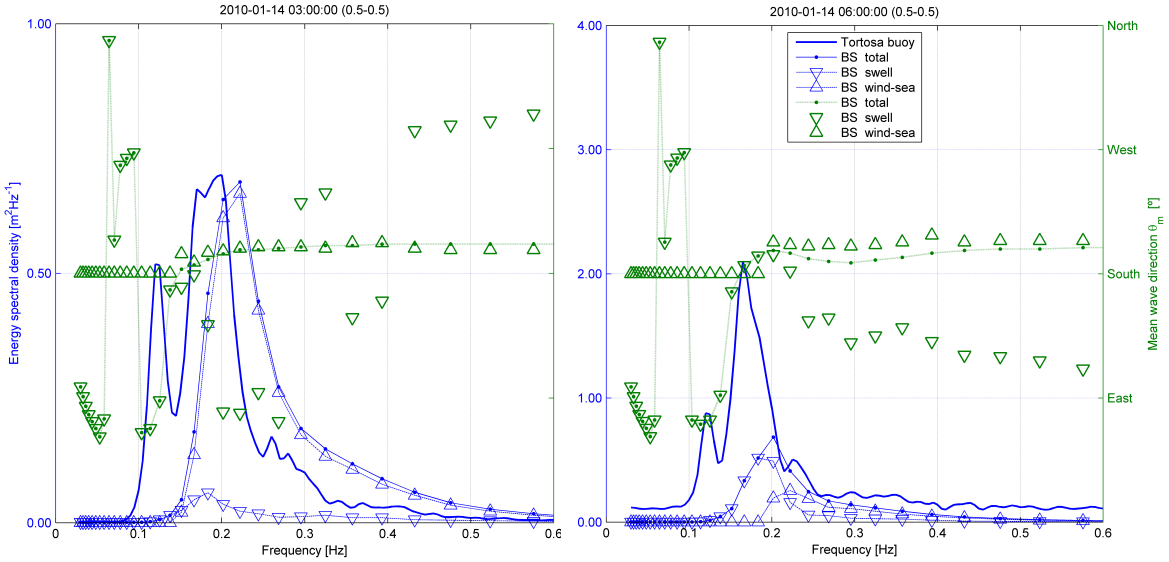

Fig. 6.19 Observed and computed wave spectra at Tortosa buoy. Partitioning of swell and wind-sea states is requested from the model and both spectral energy and mean wave directions are given for the total, swell and wind-sea spectra. Blue data are referred to the primary vertical axis (energy spectral density), whereas green data to the secondary vertical axis (mean wave direction).

Integral analysis The second approach, based on integral parameters, is introduced next. Even though it could be stated that there is a generalized underprediction of wave periods and wave heights (not always true for the latter), better agreement between observed and estimated data exists in this second storm event.

Despite the slight underestimation, significant wave heights are reasonably well predicted (for low-dissipation coefficients), although any of the proposed modifications captures the peak of the storm on January 14, at 21:00 h. The low-frequency energy (0.11-0.15 Hz), present during the first hours of the storm event, is clearly underpredicted (see Fig. 6.17), thus explaining the small wave heights at the beginning. Moving chronologically through the storm it can be seen that good agreement exists when it comes to low-dissipation coefficient combinations ($C'_{ds} = 0.5$; the delta value hardly influences wave heights, in accordance with the first storm).

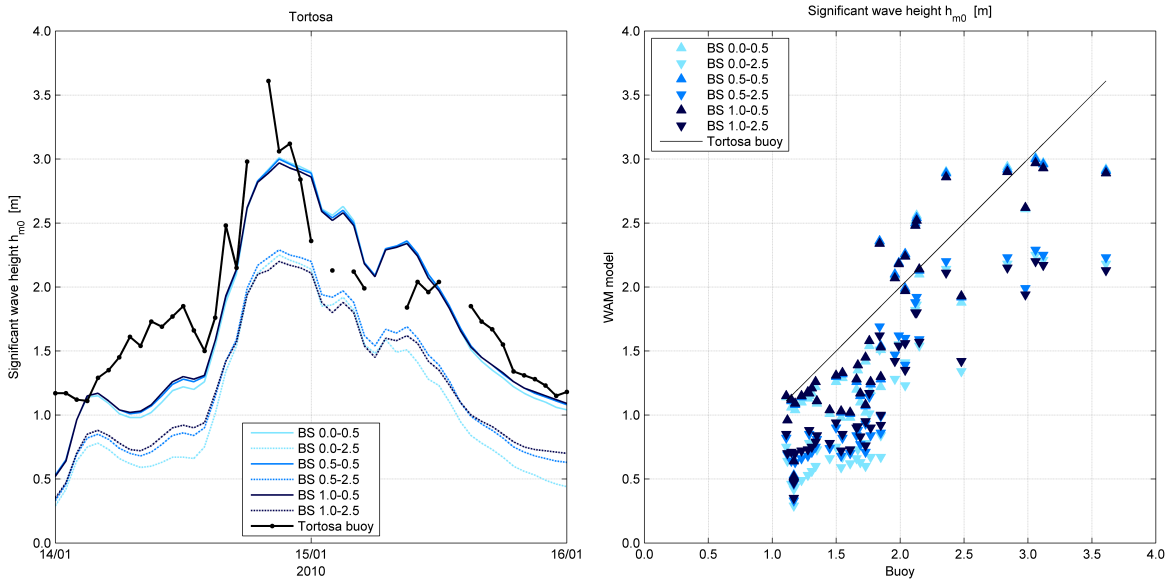

(a) (b)

Fig. 6.20 (a) Comparison of temporal evolution of the significant wave height for different whitecapping coefficients and (b) the corresponding scatter plot at the buoy of Tortosa during the second storm.

The fact that an energy peak is generated right at the peak of the storm, over the whole frequency range, puts on record the high intensity and short duration of the coastal wind jet (see Figs. 6.17 and 6.18). However, it is not captured by the wave model and suggests that this shortcoming lies in the fact that input wind fields have not correctly reproduced the sudden growth in speed. This point shall be reviewed at the end of this chapter since more insight is likely to be gained as further integral parameters are analyzed.

Next, the evolution of the mean and peak wave periods exposes the recurrent underprediction problem reported by many authors in semi-enclosed basins and bays. Therefore, both peak wave T_p and mean (zero-crossing) periods T_{m02} display differences of more than 1 s on average. However, in accordance with the analysis of the previous storm, the (1.0-0.5) combination provides best fitting (see Figs. 6.21 and 6.22). It can also be observed that there is large scatter, suggesting that wave periods are strongly influenced by these two parameters (especially delta value, which balances the low- and high-frequency energy).

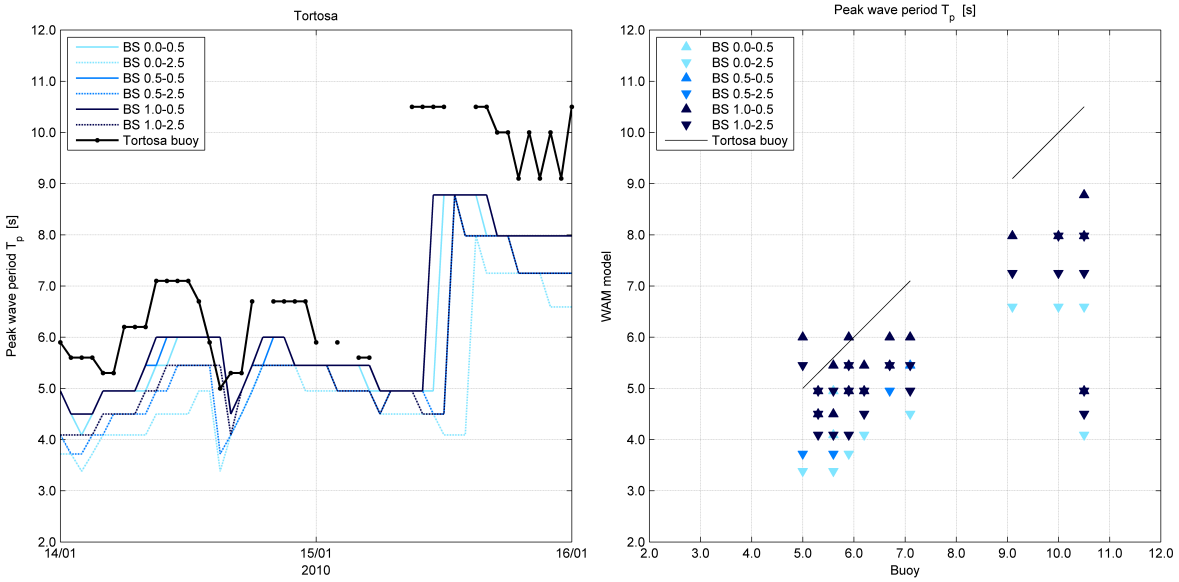

(a) (b)

Fig. 6.21 (a) Comparison of temporal evolution of the peak wave period for different whitecapping coefficients and (b) the corresponding scatter plot at the buoy of Tortosa during the second storm.

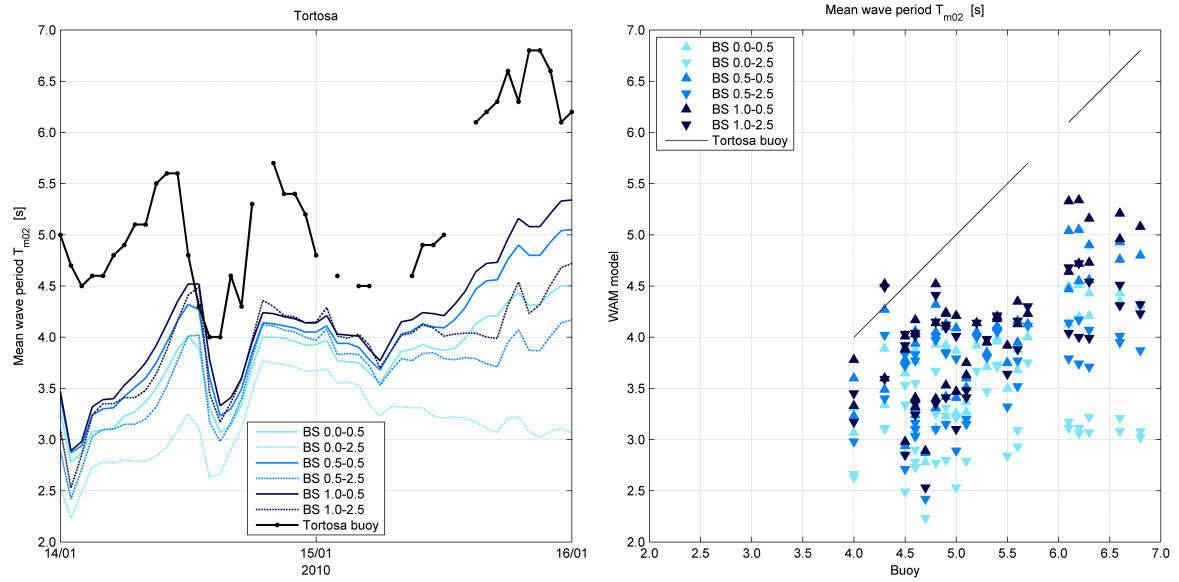

(a) (b)

Fig. 6.22 (a) Comparison of temporal evolution of the mean wave period for different whitecapping coefficients and (b) the corresponding scatter plot at the buoy of Tortosa during the second storm.

The last integral parameter reviewed is the mean wave direction, which is fairly well estimated, in particular wave groups coming from the south (January 14, between 00:00 and 15:00 h) and, later, associated with directions coming from the northwest (between the January 14, at 15:00 h and January 15, at 09:00 h). Greater dispersion, however, is shown at the end of the storm, when estimated wave directions seem to turn from northwest to east. This may be due to the fact that this gradual change is not observed on the buoy measurements; on the contrary, a sudden variation from northwest to east is noticeable (Fig. 6.23).

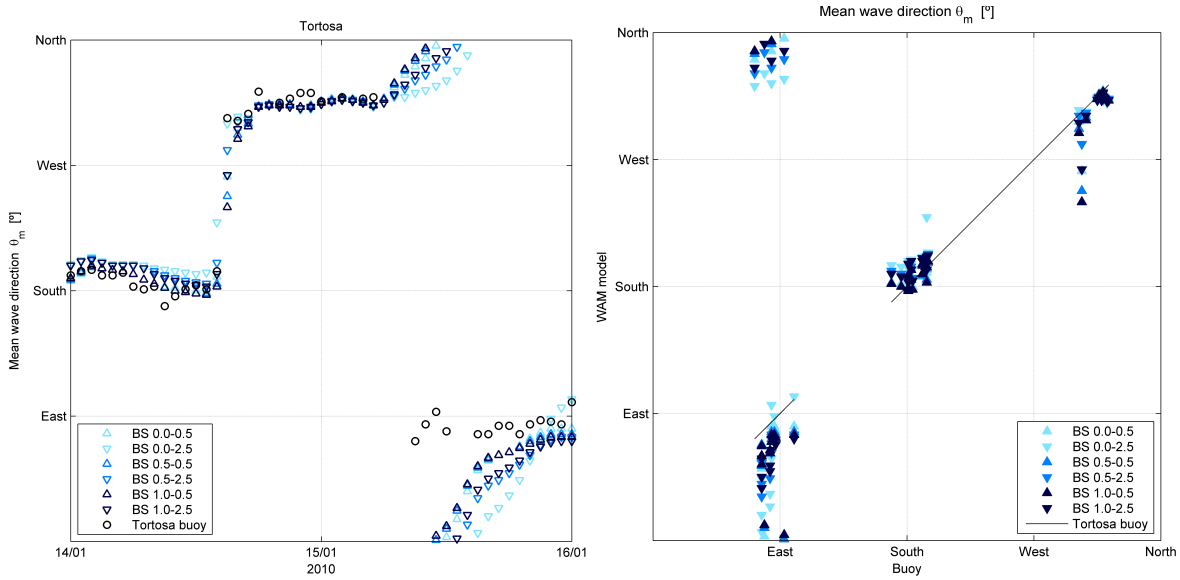

(a) (b)

Fig. 6.23 (a) Comparison of temporal evolution of the mean wave direction for different whitecapping coefficients and (b) the corresponding scatter plot at the buoy of Tortosa during the second storm.

This phenomenon can be better understood by analyzing wind velocities and directions (see Fig. 6.15). High velocities (larger than 13 $\mathrm{m\,s^{-1}}$) occur between the January 14, at 15:00 h and January 15, at 09:00 h, approximately, and are caused by the so-called coastal wind jets. The disagreement found in the mean wave direction analysis can be produced by inaccuracies inherent in the simulated wind fields. As previously commented, not only spatial but sharp temporal gradients in the Catalan coast lead to high wind variability, and many authors have concluded that using wind fields with, at least, a temporal resolution of three hours is necessary if aiming to capture the temporal scales of coastal wind jets. In addition, Alomar (2012) suggested that, in wind wave growth conditions, wave energy

responds within the same hour to wind speed and, therefore, increasing the wind input frequency from 3 h to 1 h permits rapid responses of waves to changing winds, if the wave model reaction time is, accordingly, short enough. Due to the fact that the response of wind-sea waves to wind is generally immediate (within 1 h), the fact that the mean wave directions display a gradual turning, instead of a sudden change, is likely to be induced by low resolution of the wind input and, additionally, a time-stepping excessively long in the wave simulation model.

That concludes the review of the second storm. A more general discussion of both storms is given in the next section.

6.3 Discussion

Impact on spectral energy So far, underestimation of low-frequency energy has become a systematic error. Rogers et al. (2003) suggested that underprediction of low-frequency energy can be attributed to one or more of the three deep-water source/sink terms and, focusing in the spectral dissipation, affirmed that can be also related to bulk parameters (e.g., mean steepness) that are influenced by the overprediction of high-frequency energy.

The wave model (WAM Cy 4.5.3) dissipation source function was reformulated in terms of a mean wave steepness and a mean frequency in order to give more emphasis on the high-frequency part of the spectrum (based on Hasselmann's (1974) analytical model for whitecap dissipation according to Komen et al., 1984). Unfortunately, all tests by Komen et al. (1984) were performed for wind-sea growth in the absence of swell, which was later found to generate problems inherent to the definition of a mean steepness from the entire spectrum, leading to overestimations of wind-sea growth in the presence of swell, even with the latest modification to Komen et al.'s formulation by Bidlot et al. (2005).

This shortcoming can be clearly seen during the low-frequency energy dominant peak generated at the beginning of the first storm event, in presence of a wind-energy input at higher frequencies or similarly when the wind-wave growth develops after the dissipation of the eastern swell in the same storm (Fig. 6.24). Bi-modality exists in both situations although a dominant wave group can be discerned in each one. Even though one might need to carefully examine it, low-frequency energy is always underestimated (below 0.10 Hz) and high-frequency energy is overestimated most of the time, especially when wind-sea energy is dominant (above 0.30 Hz). The latter overestimation might not be only induced due to low dissipation (resulting from mean wave steepness) but the approximation of the spectral tail, which seems to substantially yield too much energy at high frequencies.

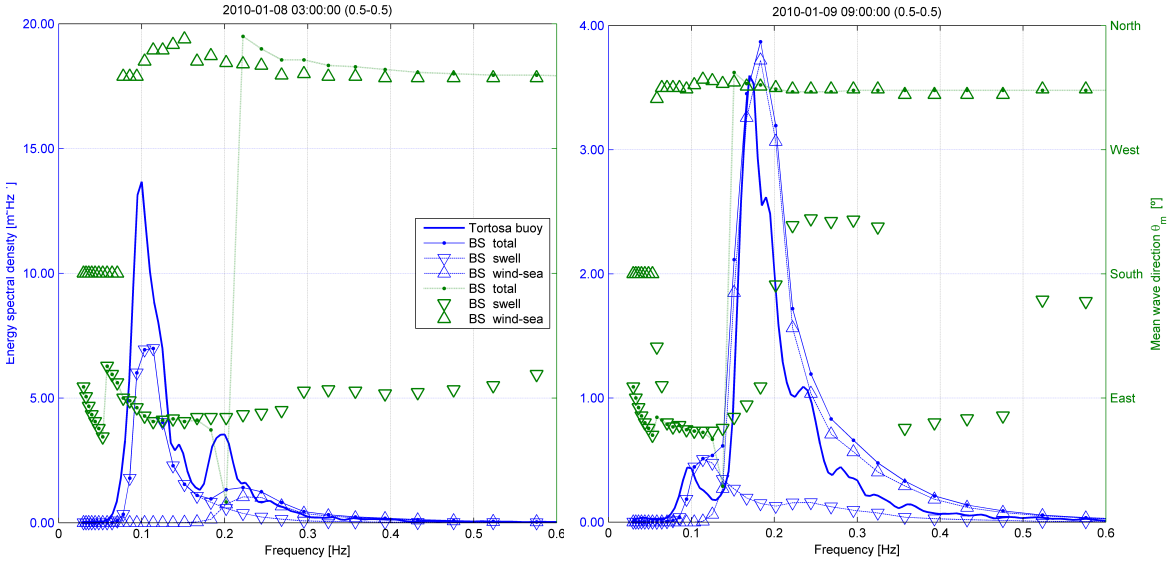

Fig. 6.24 Observed and computed wave spectra at Tortosa buoy. Partitioning of swell and wind-sea states is requested from the model and both spectral energy and mean wave directions are given for the total, swell and wind-sea spectra. Blue data are referred to the primary vertical axis (energy spectral density), whereas green data to the secondary vertical axis (mean wave direction).

Rogers et al. (2003) reported successful results tuning the exponential coefficient p to 2 in the whitecap model (equation), leading to an increase of energy at low frequencies and decreasing high-frequency energy. This is due to the fact that the exponential coefficient acts on the wave steepness and, therefore, larger steepness associated with high-frequency waves will lead larger dissipation, thus decreasing energy at that frequency range. In the present report it was not attempted to tune this third coefficient and, following the lead of Rogers et al. (2003), it was left by default at 2. A strong focus has been placed, however, on tuning the two remaining parameters.

Impact on integral parameters Different impact on integral parameters is driven by each coefficient. Significant wave heights are largely influenced by the dissipation coefficient C'_{ds}, which in turn has lower effect on wave periods. This is due to the fact that whitecapping dissipation has linear dependence on this coefficient and, therefore, if reduced, lower dissipation is guaranteed for the whole frequency range, leading to a larger overall amount of spectral energy and, hence, larger wave heights. The delta value, on the other hand, modulates the dependency on the wave number (i.e., the length of the waves) and its contribution is more subtle.

When the delta coefficient is raised to 1, maximum dependence on wave number is assured, thus yielding more dissipation at high-frequencies (short wave lengths) and lower at low-frequencies (long wave lengths). Due to the latter statement, better agreement is provided when delta is raised, thus coping with the negative adverse effect introduced by the dependence on a mean wave steepness. In addition, when implementing this modification, whitecapping dissipation places more weight on the high-frequency range and, as a result, the second-order spectral moment reduces because of the lower energy content at high frequencies. This outcome results in a substantial enhancement in the mean wave period T_{m02}, thus improving the well-known tendency to underpredict this parameter in the Catalan coast.

Statistical analysis In Chapter 5 it was stated that even though statistical parameters are representative when long time series are available (at least two or threes months simulation periods), they give a quantitative evaluation of the degree of accuracy of simulation results and will serve to support the spectral analysis results.

Table 6.1 and Table 6.2 display the abovementioned statistical parameters for each combination of whitecapping coefficients and integral parameters. It is clearly visible (bolded values) that (1.0-0.5) provides better agreement, in accordance with the previous spectral and integral analysis.

Significant wave heights show higher correlation in general, although there is no clear trend with respect to positive or negative bias. This, however, is completely true for wave periods. Negative bias in both mean and peak wave periods is observed in both storm events, regardless of the combination proposed. A result of value is displayed by the very low correlation coefficient exhibited by the peak period during the first storm (characterized by bi-modal spectrum). Similar bias is found in peak periods during both storms; however, in the first event larger scatter and root mean square errors are displayed. Another outcome that agrees with visual analysis is the fact that larger errors are encountered in mean wave directions during the first storm, in which different wave climates are found propagating in different directions at the same time.

Table 6.1 Summary of the statistical errors for the simulations during the first storm event.

	RMSE		bias		SI		R		MAE	
	WM	BS	WM	BS	WM	BS	WM	BS	WM	BS
(0.0-0.5)										
h_{m0}	0.545 m	0.596 m	-0.059 m	0.175 m	0.345	0.378	0.793	0.800		
T_p	2.503 s	2.400 s	-1.296 s	-1.102 s	0.374	0.358	0.465	0.464		
T_{m02}	1.129 s	0.963 s	-0.991 s	-0.829 s	0.261	0.223	0.761	0.808		
θ_m	100.677°	94.027°	22.181°	14.787°	0.500	0.467	0.664	0.692	43.151°	38.868°
(0.0-2.5)										
h_{m0}	0.876 m	0.766 m	-0.588 m	-0.422 m	0.555	0.485	0.680	0.689		
T_p	3.636 s	3.442 s	-2.643 s	-2.457 s	0.543	0.514	0.012	0.169		
T_{m02}	1.669 s	1.502 s	-1.506 s	-1.331 s	0.387	0.348	0.512	0.567		
θ_m	128.889°	129.135°	62.060°	59.323°	0.641	0.642	0.473	0.467	62.444°	62.171°
(0.5-0.5)										
h_{m0}	0.535 m	0.590 m	**-0.055** m	0.179 m	0.339	0.374	0.801	0.808		
T_p	**2.451** s	2.279 s	-1.202 s	-0.983 s	**0.366**	0.340	**0.475**	0.517		
T_{m02}	1.010 s	0.823 s	-0.865 s	-0.674 s	0.234	0.191	**0.777**	0.826		
θ_m	99.464°	94.502°	22.747°	16.484°	0.494	0.470	0.671	0.689	43.090°	37.959°
(0.5-2.5)										
h_{m0}	0.769 m	0.657 m	-0.497 m	-0.323 m	0.487	0.416	0.750	0.760		
T_p	3.023 s	2.883 s	-1.925 s	-1.712 s	0.452	0.431	0.370	0.386		
T_{m02}	1.336 s	1.147 s	-1.161 s	-0.957 s	0.309	0.266	0.638	0.693		
θ_m	99.083°	105.339°	33.828°	32.181°	**0.492**	0.524	**0.689**	0.634	53.747°	55.090°
(1.0-0.5)										
h_{m0}	**0.531** m	**0.580** m	-0.071 m	**0.162** m	**0.337**	**0.368**	**0.805**	**0.810**		
T_p	2.465 s	**2.271** s	**-1.201** s	**-0.962** s	0.368	**0.339**	0.470	**0.520**		
T_{m02}	**0.954** s	**0.760** s	**-0.790** s	**-0.588** s	**0.221**	**0.176**	0.775	**0.828**		
θ_m	100.756°	92.150°	26.151°	13.232°	0.501	**0.458**	0.666	**0.709**	43.565°	38.323°
(1.0-2.5)										
h_{m0}	0.776 m	0.660 m	-0.523 m	-0.351 m	0.492	0.418	0.774	0.773		
T_p	2.876 s	2.826 s	-1.752 s	-1.605 s	0.430	0.422	0.426	0.396		
T_{m02}	1.182 s	1.003 s	-0.987 s	-0.763 s	0.274	0.232	0.677	0.715		
θ_m	103.390°	100.458°	33.020°	33.313°	0.514	0.499	0.648	0.656	50.979°	49.111°

Table 6.2 Summary of the statistical errors for the simulations during the second storm event.

	RMSE		bias		SI		R		MAE	
	WM	BS	WM	BS	WM	BS	WM	BS	WM	BS
(0.0-0.5)										
h_{m0}	0.441 m	0.386 m	-0.270 m	-0.200 m	**0.242**	0.211	0.899	0.878		
T_p	2.015 s	1.978 s	-1.535 s	-1.460 s	0.270	0.265	0.749	0.736		
T_{m02}	1.670 s	**0.963** s	-0.991 s	-1.494 s	0.318	0.302	0.716	0.755		
θ_m	85.088°	73.514°	24.439°	12.658°	0.450	0.389	0.653	0.721	19.804°	16.122°
(0.0-2.5)										
h_{m0}	0.865 m	0.819 m	-0.824 m	-0.774 m	0.474	0.449	0.902	0.891		
T_p	3.036 s	2.754 s	-2.550 s	-2.342 s	0.407	0.369	0.561	0.677		
T_{m02}	2.379 s	2.281 s	-1.506 s	-2.140 s	0.454	0.435	0.152	0.189		
θ_m	101.57°	79.502°	36.122°	20.268°	0.538	0.421	0.543	0.682	35.487°	25.829°
(0.5-0.5)										
h_{m0}	0.423 m	0.364 m	**-0.249** m	**-0.178** m	0.232	0.199	0.898	0.881		
T_p	1.732 s	1.732 s	-1.280 s	-1.272 s	0.232	0.232	0.806	0.807		
T_{m02}	1.426 s	1.331 s	-0.865 s	-1.243 s	0.272	0.254	0.771	0.790		
θ_m	74.801°	63.744°	15.536°	3.195°	**0.396**	**0.337**	**0.730**	**0.788**	18.463°	16.658°
(0.5-2.5)										
h_{m0}	0.762 m	0.713 m	-0.717 m	-0.662 m	0.417	0.391	0.902	0.891		
T_p	2.611 s	2.445 s	-2.151 s	-2.017 s	0.350	0.327	0.665	0.712		
T_{m02}	1.856 s	1.760 s	-1.161 s	-1.628 s	0.354	0.336	0.524	0.503		
θ_m	82.825°	81.720°	21.682°	19.951°	0.438	0.433	0.675	0.665	27.682°	21.853°
(1.0-0.5)										
h_{m0}	**0.418** m	**0.359** m	-0.251 m	-0.180 m	0.229	**0.196**	0.898	0.883		
T_p	**1.713** s	**1.721** s	**-1.261** s	**-1.259** s	**0.229**	**0.230**	**0.808**	**0.808**		
T_{m02}	**1.300** s	1.196 s	**-0.790** s	**-1.098** s	**0.248**	**0.228**	**0.783**	**0.791**		
θ_m	75.337°	64.260°	15.414°	2.756°	0.399	0.340	0.725	0.784	17.951°	17.146°
(1.0-2.5)										
h_{m0}	0.756 m	0.709 m	-0.716 m	-0.662 m	0.415	0.389	**0.908**	**0.898**		
T_p	2.520 s	2.421 s	-2.017 s	-1.911 s	0.337	0.324	0.645	0.656		
T_{m02}	1.586 s	1.494 s	-0.987 s	-1.351 s	0.302	0.285	0.615	0.568		
θ_m	83.246°	83.268°	22.122°	19.658°	0.441	0.441	0.671	0.653	24.561°	21.219°

It is also of interest to compare the results computed at different scales (i.e., different computational grids). Better agreement is found in virtually every parameter belonging to the high-resolution domain (BS), in relation with the coarse domain (WM). It is perhaps

more interesting to note that some parameters provide better results when using data coming from the coarse grid (e.g., the scatter index SI for wave heights, h_{m0}, during the first storm). Scatter indexes are expected to be lower with high-resolution data due to the enhanced accuracy (see Fig. 6.25). Bertotti and Cavaleri (2009) obtained systematically higher scatter in their small scale model and suggested that although ironically, this fact represents the capability of the high-resolution simulations (small scale) to go into higher details of the fields. However, the capability of reproducing realistic details does not imply these details are correct. Given a certain level of scatter between the actual data and a relatively smooth (lower resolution) field, the introduction of higher resolution details, physically consistent but not necessarily coincident with the real ones, leads unavoidably to a larger scatter (commonly referred as "double penalty").

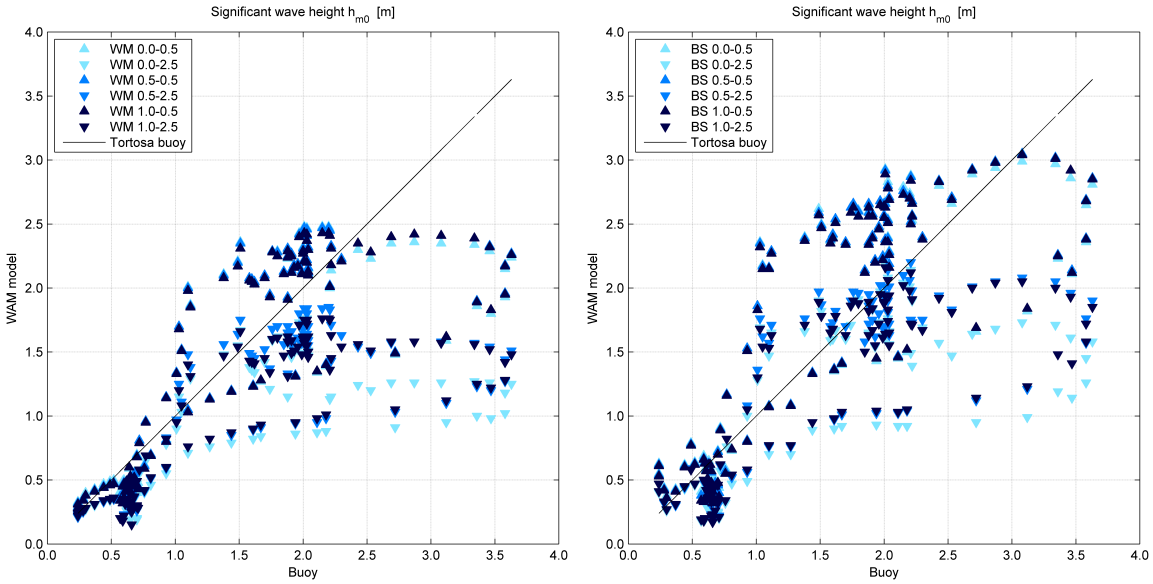

(a) Large-scale simulation (WM)

(b) Small-scale simulation (BS)

Fig. 6.25 Scatter plots for h_{m0} showing the larger scatter of the high-resolution simulation (BS). Results for the first storm event at Tortosa buoy.

Bertotti and Cavaleri (2009) concluded that high-resolution models outperform global models, even though the quality of the performance drops substantially in semi-enclosed seas. However, this is still not enough to reduce the biases to the level of the present performance in the open oceans. Note that a nested subdomain behaves according to the information it starts from (the coarse domain) and the subsequent boundary conditions along the forecast range. If a time and/or space error is present in the coarse run (storm may follow a slightly different path or move faster or slower than anticipated), this will be reflected,

possibly amplified, in the high-resolution, nested subdomain. Therefore, nested models, although capable of exceptional performances, cannot overcome all deficiencies. They simply focus on the details of a given area and, relying on their upper domain, do it correctly when correct information is provided (Bertotti and Cavaleri, 2009).

Temporal and spatial resolution of wind fields Furthermore, although not thoroughly explored in this research, it has been seen that the lack of temporal resolution in the wind fields can lead to not only underestimation but even omission of the peaks and troughs of the temporal variations of significant wave height and average wave period. As an example, the large underestimation of the wind-sea peak (0.14-0.15 Hz) associated to the peak of the second storm (January 14, at 21:00 h): observed data suggest the existence of a coastal wind jet, the time scale of which was shorter than 6 h, thus pinpointing the too coarse temporal resolution of the wind fields implemented (6 h). Therefore, an increase of the temporal resolution is strongly recommended to properly capture the instantaneous effects of coastal wind jets at the buoy of Tortosa. On the other hand, it can be seen that the spatial resolution of the wind field is not as influential as the temporal at Tortosa. This can be concluded due to the fact that wind speed and directions are fairly similar in both fine (BS) and coarse (WM) grids. (Fig. 6.15). However, in the same figure, important disagreement is found for the buoy of Blanes (and it is suspected that it would similarly occur at Llobregat). Alomar (2012) reported the benefits of increasing wind variability in wave forecasting by increasing both the temporal and spatial resolution of the forcing wind fields. High resolution input winds prevent information losses in short-duration storm, especially in basins where the orography plays a substantial role.

Near-term solution Ultimately, it can be concluded that best adjustment in storm conditions at the Catalan coast, when it comes to tuning the whitecapping dissipation term (Komen et al., 1984), occurs when the delta value is raised to 1 and the dissipation coefficient C'_{ds} is not correspondingly increased. Therefore, using the notation implemented in this chapter, the combination (1.0-0.5) provides better agreement with observed data, at both integral and spectral levels. The corresponding dissipation coefficient C_{ds} (without scaling with overall wave steepness for Pierson-Moskowitz spectrum, $\hat{s}^4_{PM}$) would be equal to 4.5×10^{-6}. It should be noted that this is a relatively low value (cf. SWAN team, 2011) and leads to believe that an overall calibration should be pursued. This modification, nevertheless, may be adopted as temporary solution for the current wave model in terms of calibrating the spectral dissipation routine; however, it should not be interpreted as an endorsement since there is a growing conviction among wave modelers that a very tunable,

empirical approach such as Tolman and Chalikov (1996) is probably the best near-term solution.

Call for further exploration The inconsistent behavior displayed by the current dissipation model (Komen et al., 1984), due to the dependence on an overall wave steepness, has been brought to light in this research. Such a dependence leads to important disagreement between computed and and hindcast data when more than one sea state are present (typical bi-modal spectrum at the Ebro delta). There is, therefore, a clear and adverse effect between low and high frequencies; mostly underestimation of low-frequency energy and overestimation of high-frequency energy. The latter might also be enhanced by the shape of the diagnostic tail. It has been concluded that the above combination slightly corrects the model's estimates, but, after all, the odds suggest that the new dissipation source term by Tolman and Chalikov (1996) can offer more realistic results due to the separation between low- and high-frequency dissipation. However, note that this source term has been tuned along with different source terms and, therefore, it is likely that remaining source terms will have to be re-tuned (in the current model). Thus, no direct forecasting of output results can be made at this point without getting thoroughly acquainted with all remaining terms. Detailed information with regard to the new formulation is presented in Section 3.2.3.

Furthermore, if extensive and high-resolution data resources could support the present research, it would be of large interest to put the model to a serious test, draw more solid conclusions and quantify the degree of improvement and confirm whether an increase in the temporal resolution of wind fields yields a qualitative leap.

Looking forward, the work by Banner and Melville (1976) has shown the clear link in an active young sea between generation and whitecapping dissipation. It is a real possibility that at some stage they will have to be considered as a single process. However, this is not for the near future. For the time being, a more physical description of whitecapping is highly in demand. There are indications that the careful analysis of the available experimental data is opening doors in this direction. In any case, the move must clearly be from empirism towards the physics (WISE Group et al., 2007).

References

Abdalla, S., Janssen, P., and Bidlot, J.-R. (2002). Use of satellite data and enhanced physics to improve wave predictions. World Scientific.

Akpınar, A., van Vledder, G. P., Kömürcü, M. İ., and Özger, M. (2012). Evaluation of the numerical wave model (SWAN) for wave simulation in the Black Sea. *Continental Shelf Research*, 50–51:80–99.

Alomar, M. (2012). *Improving wave forecasting in variable wind conditions. The effect of ressolution and growth rate for the Catalan coast.* PhD thesis, Universitat Politècnica de Catalunya.

Alves, J. H. G. M. and Banner, M. L. (2003). Performance of a Saturation-Based Dissipation-Rate Source Term in Modeling the Fetch-Limited Evolution of Wind Waves. *Journal of Physical Oceanography*, 33:1274–1298.

Ardhuin, F., Herbers, T. H. C., van Vledder, G. P., Watts, K. P., Jensen, R., and Graber, H. C. (2007). Swell and Slanting-Fetch Effects on Wind Wave Growth. *Journal of Physical Oceanography*, 37:908–931.

Babanin, A. V. and Makin, V. K. (2008). Effects of wind trend and gustiness on the sea drag: Lake george study. *Journal of Geophysical Research: Oceans*, 113(C2):n/a–n/a.

Banner, M. L., Babanin, A. V., and Young, I. R. (2000). Breaking Probability for Dominant Waves on the Sea Surface. *Journal of Physical Oceanography*, 30:3145–3160.

Banner, M. L., Jones, I. S. F., and Trinder, J. C. (1989). Wavenumber spectra of short gravity waves. *Journal of Fluid Mechanics*, 198:321–344.

Banner, M. L. and Melville, W. K. (1976). On the separation of air flow over water waves. *Journal of Fluid Mechanics*, 77:825–842.

Battjes, J. and Janssen, J. (1978a). Energy loss and set-up due to breaking of random waves. *Coastal Engineering, ASCE*, pages 569–587.

Battjes, J. A. and Janssen, J. P. F. M. (1978b). Energy loss and set-up due to breaking random waves. In *Proceedings of 16th Conference on Coastal Engineering*, pages 569–587, Hamburg.

Bertotti, L. and Cavaleri, L. (2004). Accuracy of the modelled wind and wave fields in enclosed seas. *Tellus A*, 56(2):167–175.

Bertotti, L. and Cavaleri, L. (2009). Large and small scale wave forecast in the Mediterranean Sea. *Natural Hazards and Earth System Sciences*, 9:779–788.

Bidlot, J., Abdalla, S., and Janssen, P. (2005). A revised formulation for ocean wave dissipation in CY25R1. Technical Report Memorandum R60.9/JB/0516, Research Department, ECMWF, Reading, U. K.

Bolaños, R. (2004). *Tormentas de oleaje en el Mediterráneo: Física y Predicción*. PhD thesis, Universitat Politècnica de Catalunya.

Bolaños, R., Jorda, G., Cateura, J., Lopez, J., Puigdefabregas, J., Gomez, J., and Espino, M. (2009). The XIOM: 20 years of a regional coastal observatory in the Spanish Catalan coast. *Journal of Marine Systems*, 77:237–260.

Bolaños, R., Osuna, P., Wolf, J., Monbaliu, J., and Sánchez-Arcilla, A. (2011). Development of the polcoms–wam current–wave model. *Ocean Modelling*, 36:102–115.

Bolaños, R., Sánchez-Arcilla, A., and Cateura, J. (2007). Numerical study of the marine breeze around Mallorca Island. *Journal of Marine Systems*, 65:336–353.

Bosboom, J. and Stive, M. J. F. (2013). *Coastal Dynamics I*. Cambridge University Press.

Bouws, E. and Komen, G. J. (1983). On the balance between growth and dissipation in an extreme depth-limited wind-sea in the southern north sea. *Journal of Physical Oceanography*, 13:1653–1658.

Cavaleri, L. and Rizzoli, P. M. (1981). Wind wave prediction in shallow water: Theory and applications. *Journal of Geophysical Research: Oceans*, 86(C11):10961–10973.

Cavaleri, L. and Sclavo, M. (2006). The calibration of wind and wave model data in the Mediterranean Sea. *Coastal Engineering*, 53:613–627.

Day, J. W., Martin, J. F., Cardoch, L., and Templet, P. H. (1997). System functioning as a basis for sustainable management of deltaic ecosystems. *Coastal Management*, 25:115–153.

de León, S. P. and Orfila, A. (2013). Numerical study of the marine breeze around Mallorca Island. *Applied Ocean Research*, 40:24–36.

del Amo, P. A. A. (2000). *Aspectos de la variabilidad de mesoescala de la circulación marina en la plataforma continental catalana*. PhD thesis, Universitat Politècnica de Catalunya.

Donelan, M. A. and Pierson, W. J. (1987). Radar scattering and equilirbium ranges in wind-generated waves with application to scatterometry. *Journal of Geophysical Research*, C92:4971–5029.

Donelan, M. A. and Yuan, Y. (1994). *Wave dissipation by surface processes*, chapter II.4, pages 143–155. Cambridge University Press.

Duncan, J. H. (1981). An experimental investigation of breaking waves produced by a towed hydrofoil. *Proceedings of the Royal Society of London. A. Mathematical and Physical Sciences*, 377(1770):331–348.

Eldeberky, Y. and Battjes, J. A. (1996). Spectral modelling of wave breaking. *Journal of Geophysical Research*, 101:1253–1264.

Flamant, C., Pelon, J., Eymard, L., and Tournadre, J. (2003). SSM/I integrated water vapor content measurements in coastal regions: A comparison with shipborne and airborne remote sensing measurements, radiosonde measurements, and NWP model retrievals. *Journal of Geophysical Research: Oceans*, 108(C3):FET 4–1–FET 4–20.

Gómez, J., Sánchez-Arcilla, Puigdefabregas, J., Sospedra, J., and de León, S. P. (2001). Clima marítimo en la costa catalana. implicaciones para predicción de oleaje. In *VI Jornadas Españolas de Ingeniería de Costas y Puertos*, Palma de Mallorca.

Günther, H. and Behrens, A. (2011). *The WAM Model Version 4.5.3*. Institute of Coastal Research, Helmholtz-Zentrum Geesthacht (HZG).

Guillaume, A. (1990). Statistical Tests for the Comparison of Surface Gravity Wave Spectra with Application to Model Validation. *Journal of Atmoshperic and Oceanic Technology*, 7:551–567.

Günther, H. (2006). *WAM Cycle 4.5*. Institute of Coastal Research, Forschungszentrum (GKSS).

Günther, H., Hasselmann, S., and Janssen, P. A. E. M. (1992). The WAM Model cycle 4. Report No. 4. Technical report, Hamburg.

Hasselmann, K. (1962). On the non-linear energy transfer in a gravity-wave spectrum Part 1. General theory. *Journal of Fluid Mechanics*, 12:481–500.

Hasselmann, K. (1974). On the spectral dissipation of ocean waves due to white capping. *Boundary-Layer Meteorology*, 6(1-2):107–127.

Hasselmann, K., Barnett, T. P., Bouws, E., Carlson, H., Cartwright, D. E., Enke, K., Ewing, J. A., Gienapp, H., Hasselmann, D. E., Kruseman, P., Meerburg, A., Müller, P., Olbers, D. J., Richter, K., Sell, W., and Walden, H. (1973). Measurements of wind-wave growth and swell decay during the Joint North Sea Wave Project (JONSWAP). *Deutsche Hydrogrphische Zeitschrift*, 12.

Hasselmann, S. and Hasselmann, K. (1981). A symmetrical method of computing the nonlinear transfer in a gravity-wave spectrum. *Hamburger Geophys. Einzelschr.*, 52:138.

Hasselmann, S., Hasselmann, K., Allender, J. H., and Barnett, T. P. (1985). Computations and Parameterizations of the Nonlinear Energy Transfer in a Gravity-Wave Spectrum. Part II: Parameterizations of the Nonlinear Energy Transfer for Application in Wave Models. *Journal of Physical Oceanography*, 15:1378–1391.

Hersbach, H. (1997). *The adjoint of the WAM model*. KNMI.

Hersbach, H. and Janssen, P. A. E. M. (1999). Improvement of the short-fetch behavior in the wave ocean model (WAM). *Journal of Atmospheric and Oceanic Technology*, 16:884–892.

Holthuijsen, L. H. (2007). *Waves in Oceanic and Coastal Waters*. Cambridge University Press.

Holthuijsen, L. H. and Herbers, T. H. C. (1986). Statistics of Breaking Waves Observed as Whitecaps in the Open Sea. *Journal of Physical Oceanography*, 16:290–297.

Hwang, P. A., García-Nava, H., and Ocampo-Torres, F. J. (2011). Observations of Wind Wave Development in Mixed Seas and Unsteady Wind Forcing. *Journal of Physical Oceanography*, 41:1020–1034.

Janssen, P. A. E. M. (1991). Quasi-linear theory of wind wave generation applied to wave forecasting. *Journal of Physical Oceanography*, 21:1631–1642.

Komen, G. J., Cavaleri, L., Donelan, M., Hasselmann, K., Hasselmann, S., and Janssen, P. A. E. M. (1994). *Dynamics and Modelling of Ocean Waves*. Cambridge University Press, 2006 edition.

Komen, G. J., Hasselmann, S., and Hasselmann, K. (1984). On the Existence of a Fully Developed Wind-Sea Spectrum. *Journal of Physical Oceanography*, 14:1271–1283.

Kuik, A. J., van Vledder, G. P., and Holthuijsen, L. H. (1988). A Method for the Routine Analysis of Pitch-and-Roll Buoy Wave Data. *Journal of Physical Oceanography*, 18:1020–1034.

Lin, W., Sanford, L. P., and Suttles, S. E. (2002). Wave measurement and modeling in Chesapeake Bay. *Continental Shelf Research*, 22(18-19):2673–2686.

Longuet-Higgins, M. S. (1969). On wave breaking and the equilibrium spectrum of wind-generated waves. *Proceedings of the Royal Society of London. A. Mathematical and Physical Sciences*, 310(1501):151–159.

Longuet-Higgins, M. S., Cartwright, D. E., and Smith, N. D. (1963). Observations of the directional spectrum of sea waves using the motions of a floating buoy, in ocean wave spectra. *Prentice-Hall*, pages 111–136.

Makin, V. K. and Kudryavtsev, V. N. (1999). Coupled sea surface-atmosphere model: 1. wind over waves coupling. *Journal of Geophysical Research: Oceans*, 104(C4):7613–7623.

Miche, R. (1944). Mouvements ondulatoires des mers en profondeur constante ou décroissante. *Annales des ponts et chaussées*, 114:369–406.

Miles, J. W. (1957). On the generation of surface waves by shear flows. *Journal of Fluid Mechanics*, 3:185–204.

Osuna, P., Souza, A. J., and Wolf, J. (2007). Effects of the dep-water wave breaking dissipation on the wind-wave modelling in the Irish Sea. *Journal of Marine Systems*, 67:59–72.

Pallares, E., Sánchez-Arcilla, A., and Espino, M. (2014). Wave energy balance in wave models (SWAN) for semi-enclosed domains-Application to Catalan coast. *Continental Self Research*.

Phillips, O. M. (1957). On the generation of waves by turbulent wind. *Journal of Fluid Mechanics*, 2:417–445.

Phillips, O. M. (1985). Spectral and statistical properties of the equilibrium range in wind-generated gravity waves. *Journal of Fluid Mechanics*, 156:505–531.

Pierson, W. J. and Moskowitz, L. (1964). A proposed spectral form for fully developed wind seas based on the similarity theory of S. A. Kitaigorodskii. *Journal of Geophysical Research*, 69(24):5181–5190.

Portilla, J. (2009). *Buoy data assimilation in nearshore wave modelling*. PhD thesis, Katholieke Universiteit Leuven.

Puig, P., Canals, M., Company, J. B., Martín, J., Amblas, D., Lastras, G., Palanques, A., and Calafat, A. M. (2012). Ploughing the deep sea floor. *Letter Research*, 489:286–290.

Reistad, M., Breivik, O., and Bokhorst, R. (2008). Wave Modelling with WAM. Fifth Regional Workshop on Storm Surge and Wave Forecasting.

Rogers, W. E., Hwang, P. A., and Wang, D. W. (2003). Investigation of Wave Growth and Decay in the SWAN Model: Three Regional-Scale Applications. *Journal of Physical Oceanography*, 33:366–389.

Sánchez-Arcilla, A., González-Marco, D., and Bolaños, R. (2008). A review of wave climate and prediction along the spanish mediterranean coast. *Natural Hazards and Earth System Science*, 8(6):1217–1228.

Sánchez-Arcilla, A., Jimenez, J. A., and Valdemoro, H. I. (1998). The Ebro delta: morphodynamics and vulnerability. *Journal of Coastal Research*, 14(3):754–772.

Snyder, R. L., Dobson, F. W., Elliott, J. A., and Long, R. B. (1981). Array measurements of atmospheric pressure fluctuations above surface gravity waves. *Journal of Fluid Mechanics*, 102:1–59.

SWAMP Group (1985). Ocean wave modeling. In *Plenum Press*, page 266, New York.

SWAN team (2011). *Scientific and Technical Documentation SWAN Cycle III version 41.01*. Faculty of Civil Engineering and Geosciences, Delft University of Technology.

Tolman, H. L. (1992). Effects of Numerics on the Physics in a Third-Generation Wind-Wave Model. *Journal of Physical Oceanography*, 22:1095–1111.

Tolman, H. L. (2014). User manual and system documentation of WAVEWATCHIII version 4.18. Technical report.

Tolman, H. L. and Chalikov, D. (1996). Source Terms in a Third-Generation Wind Wave Model. *Journal of Physical Oceanography*, 26:2497–2518.

WAFO-group (2000). *WAFO - A Matlab Toolbox for Analysis of Random Waves and Loads - A Tutorial*. Math. Stat., Center for Math. Sci., Lund Univ., Lund, Sweden.

WAMDIG (1988). The WAM model - A third generation ocean wave prediction model. *Journal of Physical Oceanography*, 18:1775–1810.

WISE Group, Cavaleri, L., Alves, J. H. G. M., Ardhuin, F., Babanin, A., Banner, M., Belibassakis, K., Benoit, M., Donelan, M., Groeneweg, J., Herbers, T. H. C., Hwang, P., Janssen, P. A. E. M., Janssen, T., Lavrenov, I. V., Magne, R., Monbaliu, J., Onorato, M., Polnikov, V., Resio, D., Rogers, W. E., Sheremet, A., McKee Smith, J., Tolman, H. L., van Vledder, G. P., and Wolf, J.and Young, I. (2007). Wave modelling–the state of the art. *Progress in Oceanography*, 75:603–674.

Young, I. and Banner, M. (1992). Numerical experiments on the evolution of fetch limited waves. In Banner, M. L. and Grimshaw, R. H. J., editors, *Breaking Waves*, International Union of Theoretical and Applied Mechanics, pages 267–275. Springer Berlin Heidelberg.

Young, I. R. and Babanin, A. V. (2006). Spectral distribution of energy dissipation of wind-generated waves due to dominant wave breaking. *Journal of Physical Oceanography*, 36:376–394.

Yuan, Y., Tung, C., and Huang, N. (1986). Statistical characteristics of breaking waves. In Phillips, O. and Hasselmann, K., editors, *Wave Dynamics and Radio Probing of the Ocean Surface*, pages 265–272. Springer US.

Appendix A

The WAM model

Explanation below has been imported from Günther and Behrens (2011). For further information please consult Komen et al. (1994).

A.1 The model system

The model system consists of three major program parts:

1. Pre-processing program
2. Processing program
3. Post-processing programs

A.1.1 Pre-processing program

`PREPROC` generates time independent information for the wave model. Starting from a regional or global topographic data set, the model grid is created in the form required for the model. The frequency and angular arrays are generated. A number of model constants are pre-computed and stored together with the model grid, frequency, and angular information in the output file. If nested grids are generated, the information for the output, input and interpolation of boundary spectra are pre-computed. A topographic data file has to be provided by the user. If a fine grid run is requested, the `PREPROC` output file from the coarse grid is necessary too.

A.1.2 Processing program

CHIEF is the shell program of the stand-alone version of the wave model calling the subroutine version of the wave model. All time dependent variables and user-defined parameters are fixed, the wind fields are transformed into the model formats, and the transport equation is integrated over a chosen period. The initial spectra are generated in case of a cold start.

The program uses the output file of PREPROC as set-up files. A wind input file and optional ice file and/or current file and/or boundary value files have to be provided by the user.

A number of model options and parameters can be selected by the. The following model options are implemented:

- Cartesian or spherical propagation
- Deep or shallow water
- Without or with depth or with depth and current refraction
- Depth induced breaking
- Nested grids
- Time interpolation of winds or no time interpolation
- Model output at regular intervals or by list
- Printer and/or file output of individually selected parameters.
- Output variables
- Output sites for spectra
- Cold or hot start

The model results (if selected) are saved in two files one for integrated parameters and one for spectra at specified sites.

A.1.3 Post-processing programs

Four post-processing programs are provided:

- `PRINT_GRID_FILE`: Prints the maps of integrated parameters.
- `PRINT_TIME`: Prints time series of integrated parameters at selected sites.
- `PRINT_SPECTRA_FILE`: Prints time series of spectra at selected output sites.
- `PRINT_RADIATION_FILE`: Prints the maps of radiation stress parameters.

The programs are set up for the model result files. Controlled by the user input the results are printed. Plot software is not included in the standard set of programs.

A.2 Communication between the subsystems

The program system uses 6 different types of files:

- User input files, which are needed by each program to control the execution.
- Protocol output files, which are generated by each program.
- Input data files, which have to be provided by the user.
- A Set-up file, which is generated by `PREPROC` and used by `CHIEF`.
- Result files, which are generated by `CHIEF` and used by the post-processing programs.
- Restart files, which are generated and used by `CHIEF`.

Figs. A.1, A.2 and A.3 show an overview about the input and output files used by the different main programs.

The file names for the user input and protocol output files are defined in the modules and cannot be changed from outside the program. The files have to be in the directory where the program is executed. The user input files have a fixed format or are namelists. Examples are provided with the code. See Annex A for details.

Input data files are:

- Topographic data for PREPROC.
- Wind data for CHIEF.
- Wind data for CHIEF.
- Current data (optional) for CHIEF (optional).
- Depth data (optional) for CHIEF (optional).
- Ice data for CHIEF (optional).

These files are dynamically assigned by OPEN. The file names must be defined in the user input files. The full path names have to be provided if the data are not in the directory where the program is executed.

Set-up file is generated by PREPROC. It contains the model constants and the general grid information. This file is dynamically assigned by OPEN. The file names are pre-defined in the user modules, but can be changed in the user input files. The full path names have to be provided if the data are not in the directory where the program is executed. The set-up file is unformatted.

Result files are the model output files generated by CHIEF. Different files store the integrated data, the spectra and the radiation stress output. If the nesting option is on, the model generates boundary value files for a follow-up fine grid or reads in boundary spectra from existing files. All these files are dynamically assigned by OPEN. The file names are built from in the user modules pre-defined file identifier, which can be changed in the user input files, extended by the date of the last output stored in the file. The full path names have to be provided if the data are not stored in the directory where the program is executed. Details of the file name convention are given in Subroutine OPEN_FILE, which is located in the WAM_GENERAL_MODULE. All result files are unformatted. Restart files follow the same rules as result files.

Fortran read and write units inside the programs are integer variables following the convention IUxx, where xx is the unit number, e.g. xx = 01, xx = 11. The default units and standard filenames are defined in the user modules and can be changed in the user input files.

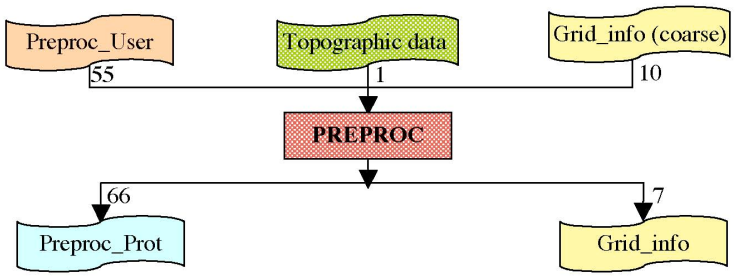

Fig. A.1 Input and output files for PREPROC.

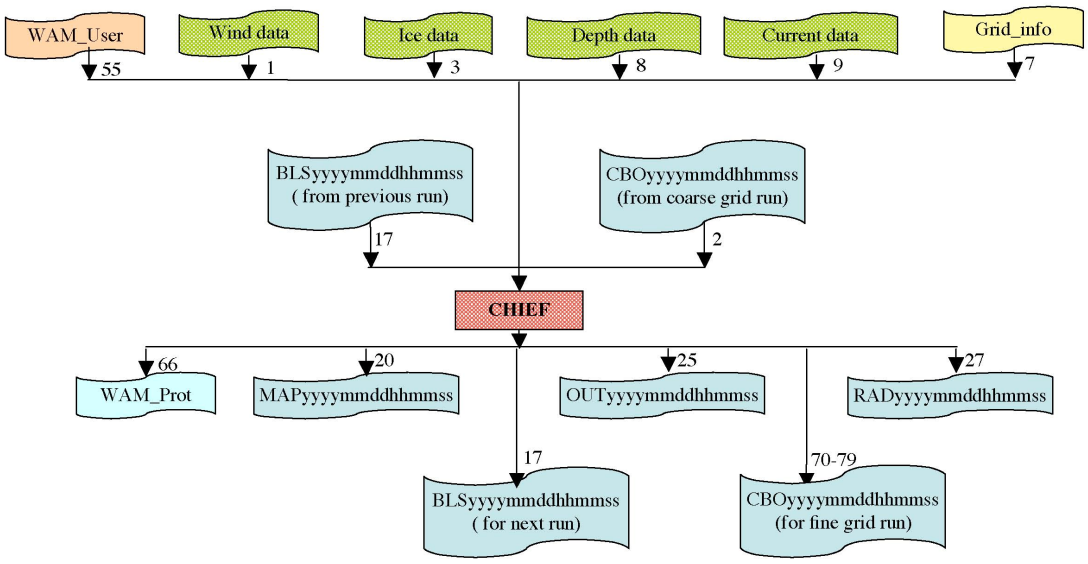

Fig. A.2 Input and output files for CHIEF.

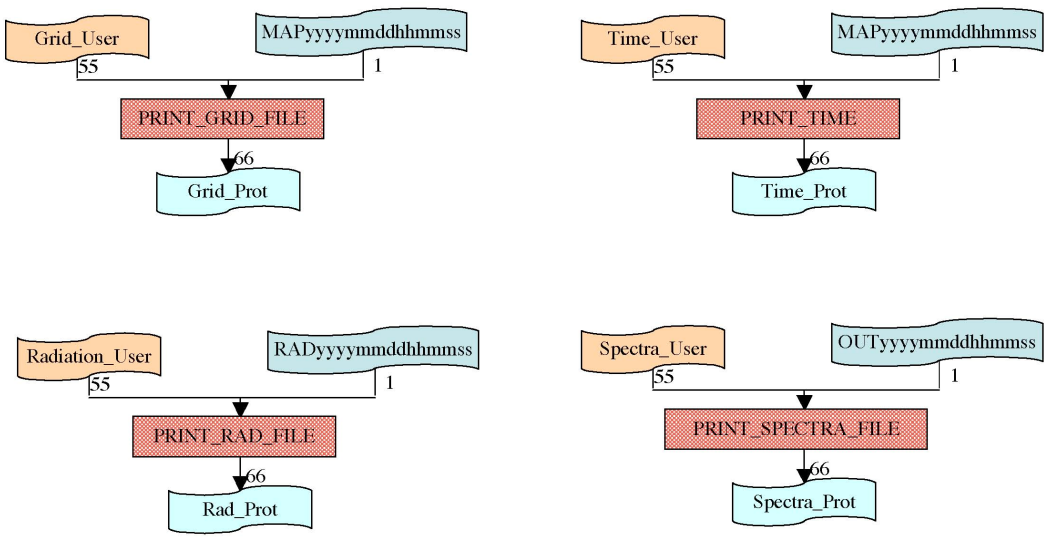

Fig. A.3 Input and output files for the post-processing programs.

A.3 Numerical implementation

In this appendix the numerical aspects of the solution of the action balance equation as implemented in the WAM model are introduced (Komen et al., 1994).

The actual WAM model is formulated in terms of the frequency-dispersion spectrum $E(f,\theta)$ of the variance of the surface elevation. The continuous wave spectrum is approximated in the numerical model by means of step functions which are constant in a frequency-direction bin. The size of the frequency-direction bin depends on frequency. There is a clear distinction between the prognostic and diagnostic part of the spectrum. The prognostic part of the spectrum has KL directional bands and ML frequency bands. These frequency bands are on a logarithmic scale, with $\Delta f/f = 0.1$, spanning a frequency range $f_{\max}/f_{\min} = (1.1)^{\mathrm{ML}-1}$. This logarithmic scale was chosen in order to have uniform relative resolution, and also because the nonlinear transfer scales with frequency (Komen et al., 1994). The starting frequency may be selected arbitrarily. In the present study, the starting frequency f_0 is 0.030 Hz, the number of frequencies ML is 33 and the number of directions KL is 24 (15° resolution).

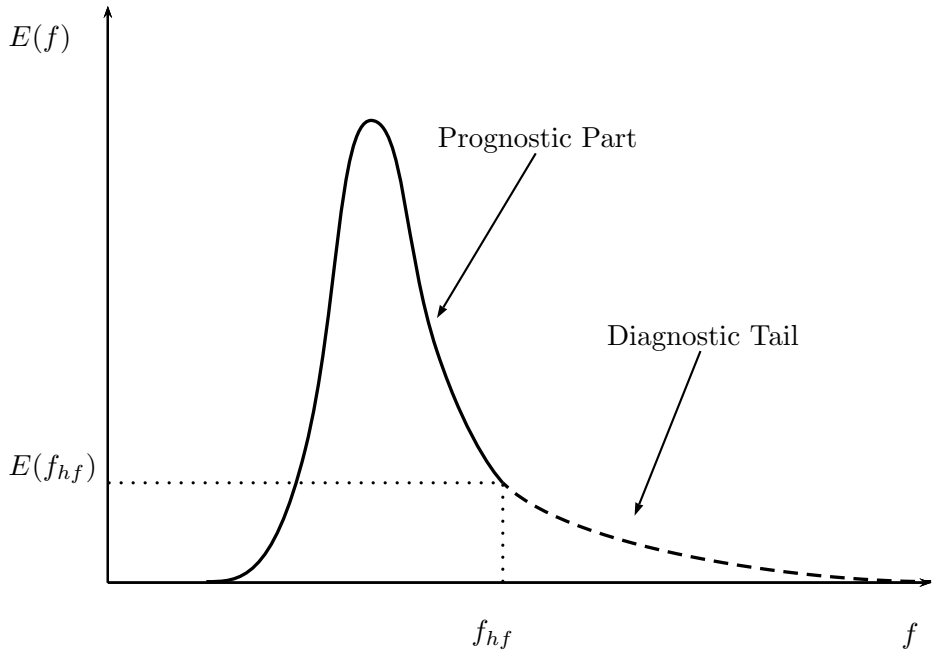

Fig. A.4 Prognostic part and diagnostic high-frequency tail of wave spectrum E.

Beyond the high-frequency limit f_{hf} of the prognostic region of the spectrum, an f^{-5} tail is added, with the same directional distribution as the last band of the prognostic region

(see Fig. A.4). The diagnostic part of the spectrum is therefore given as (cf. Eq(3.1)):

$$E(f,\theta) = E(f_{hf},\theta)\left(\frac{f}{f_{hf}}\right)^{-5} \qquad \text{for } f > f_{hf} \tag{A.1}$$

The high-frequency limit is set as:

$$f_{hf} = \min\{f_{\max}, \max(2.5\langle f\rangle, 4f_{PM})\} \tag{A.2}$$

Thus, the high-frequency extent of the prognostic tail is scaled for young waves by the mean frequency $\langle f\rangle$ and for more developed wind-seas by the Pierson-Moskowitz frequency f_{PM}. A dynamic high-frequency cut-off, f_{hf}, rather than a fixed cut-off at $f_{\max}$ is assumed to be necessary to avoid disparities in the response time scales within the spectrum.

A diagnostic tail is added for $f > f_{hf}$ to compute the nonlinear transfer in the prognostic region and also to compute the integral quantities which occur in the dissipation source function.

The prognostic part of the spectrum is therefore obtained by numerically solving the energy balance equation (2.18). Below are presented the different numerical schemes and time steps used to integrate the source functions and the advective terms of the transport equation.

A.3.1 Implicit-scheme (integration of the source functions)

An implicit scheme was introduced for the source function integration to enable the use of an integration time step that was larger than the dynamic adjustment time of the highest frequencies still treated prognostically in the model.

The energy balance of the spectrum is evaluated in detail up to a high cutoff frequency (A.1). The high-frequency adjustment time scales are considerably shorter than the evolution time scales of the energy-containing frequency bands near the peak of the spectrum. Thus, in the high-frequency region it is sufficient to determine the quasi-equilibrium level to which the spectrum adjusts in response to the more slowly changing low-frequency waves rather than the time history of the short time-scale adjustment process itself.

This requirement is achieved by implementing a time-centered implicit integration scheme whose time step is matched to the evolution of the lower frequency waves: for low-frequency waves, the integration method yields essentially the same results as a simple forward in-

tegration technique, while for high frequencies the method yields the (slowly changing) quasi-equilibrium spectrum.

Therefore, the implicit second-order, centered difference equations (leaving out the advection terms) are given by:

$$E_{n+1} = E_n + \frac{\Delta t}{2}(S_{n+1} + S_n) \tag{A.3}$$

where Δt is the time step and the index n refers to the time level.

If S_{n+1} depends linearly on E_{n+1}, Eq.(A.3) could be directly solved for the spectrum E_{n+1} at the new time step. However, none of the source terms are linear. Therefore, a Taylor expansion is introduced:

$$S_{n+1} = S_n + \frac{\partial S_n}{\partial E}\Delta E + \cdots \tag{A.4}$$

The functional derivative in (A.4) (numerically a discrete matrix M_n) can be divided into a diagonal matrix Λ_n and a nondiagonal residual N_m:

$$\frac{\partial S_n}{\partial E} = M_n = \Lambda_n + N_n \tag{A.5}$$

Substituting (A.4) and (A.5) into (A.3) it is obtained (the source term S depends on the friction velocity u_* at time level $n+1$):

$$\left[1 - \frac{1}{2}\Delta t \left\{\Lambda_n(u_*^{n+1}) + N_n(u_*^{n+1})\right\}\right]\Delta E = \frac{1}{2}\Delta t \left(S_n(u_*^n) + S_n(u_*^{n+1})\right) \tag{A.6}$$

with $\Delta E = E_{n+1} - E_n$. A number of trial computations were needed by Komen et al. (1994) to conclude that the off diagonal contributions were generally small if the time step was not too large. Disregarding these contributions, the matrix on the left side is inverted, yielding for the increment ΔE:

$$\Delta E = \frac{1}{2}\Delta t \left(S_n(u_*^n) + S_n(u_*^{n+1})\right)\left[1 - \frac{1}{2}\Delta t \Lambda_n(u_*^{n+1})\right]^{-1} \tag{A.7}$$

For a typical test case, good agreement was obtained between an explicit integration with a a time step of 3 min and the implicit scheme with only diagonal terms for time steps up to about 20 min (cf. time step implemented in Section 5.1).

Further information in relation with the advective terms and refraction is provided by Komen et al. (1994), where it is explained the choice of the first order upwinding scheme for the advection scheme in the energy balance equation (interpreted in terms of energy flux).

A.3.2 Boundary conditions and grid nesting

Wave model grids are commonly surrounded by land points. Therefore, the natural boundary conditions are no energy flux into the grid and free advection of energy out of the grid at the coast line.

WAM model was developed with the practical application in mind of running a global ocean wave model, covering large scales. However, near the coast, the scale of a wave system is determined by the coastal geometry and bottom topography, which have usually much smaller scales.

One way out of this problem would be to run a wave model with a variable grid, having a high resolution whenever needed (e.g., near the coast) and having a coarse resolution in the open ocean. So far this approach has not been followed. Preference was given to another solution, in which one has the option to run the model on nested grids. This gives the opportunity to use results of a coarse mesh model from a large region in a fine mesh regional model. Several successive levels of nesting may be necessary. The two-dimensional spectra computed by the coarse mesh model are saved at grid points which are on the boundary of the limited area, high-resolution grid. These spectra are then interpolated in space and time to match the high resolution at the grid boundaries. A special interpolation procedure is used. Instead of linearly interpolating the spectra from the adjacent points of the coarse grid directly, these spectra are rescaled in such a way that have the same mean frequency, mean wave direction and wave energy as found from a linear interpolation of these mean quantities to the fine mesh grid point. The wave spectrum at the fine mesh grid point is then found by linearly interpolating the rescaled spectra.